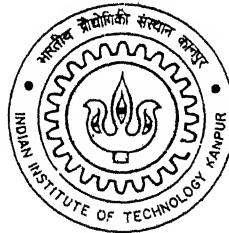


**A Study of Free Surface Effects
on Through Cracks under Static
and Dynamic Conditions using
Boundary Element Method**

by

ATUL KUMAR AGRAWAL



**DEPARTMENT OF MECHANICAL ENGINEERING
INDIAN INSTITUTE OF TECHNOLOGY, KANPUR
January, 2001**

सं. १३४२२०
सं. १३४२२०
सं. १३४२२०
सं. १३४२२०

TH
ME/2001/P
Ag 213



A134220



CERTIFICATE

It is certified that the work contained in the thesis entitled **A Study of Free Surface Effects on Through Cracks Under Static and Dynamic Conditions using Boundary Element Method**, by **ATUL KUMAR AGRAWAL**, has been carried out under supervision and that this work has not been submitted elsewhere for a degree.

Date: January 25, 2001

N. N. Kishore
25/1

Professor N. N. Kishore
Department of Mechanical Engineering
Indian Institute of Technology
Kanpur, 208016

SYNOPSIS

In this thesis, the effect of free surfaces on fracture characteristics for elastostatic and elastodynamic problems is investigated using three-dimensional boundary element method. Free surface effect is studied for a through center cracked finite body for three situations: quasi-static conditions, stationary crack under impact loading and running crack under impact loading.

A crack front intersecting the free surface in a 3-D body has been a subject of interest for last three decades. Through-thickness fatigue cracks in plate geometries almost always show crack front tunnelling, i.e., a curved crack front with the deepest point of the crack at the center. Benthien [1] analyzed a problem of a quarter-plane crack in a semi-infinite half-space subjected to symmetric quasi-static loading. For a crack front normal to the free surface, he derived that at the corner point, stresses have $r^{-.452}$ singularity for Poisson's ratio (ν) of 0.3. By a local finite element analysis, Bažant and Estenssoro [2] estimated critical intersection angle to be 101° (for $\nu = 0.3$) for a stationary crack under elastostatic loading. By a finite element formulation similar to that used by Bažant and Estenssoro, Gudmundson and Östlund [3] found that a weaker singularity also exists at the corner point for a dynamically growing crack and estimated the critical angle to be 101° , almost independent of the crack-tip velocity. They found that for angles between 90° and about 101° , singularity weakened further with increasing velocity and for angles larger than about 101° , singularity became stronger with increasing velocity.

The success enjoyed by these local numerical analyses is not found to the same extent in finite element treatments of more global or complete problems which contain crack/surface intersections. Different predictions were made concerning the variation in energy release rate (G) with some results showing an increase in G in the free surface region, some decrease and still others no change for quasi-static analysis. Burton *et al.* [4] generated critical crack profiles using FEM with each profile having less than 2% numerical variation in G with depth. The crack profiles generated by them were significantly less curved than those observed in practice [5]. They surmised that underlying assumptions in linear elastic fracture mechanics (LEFM) were to a degree incapable of explaining all of the various phenomena leading to free surface retardation. Using FEM for analysis, Lin and Smith [6] found that slightly non-orthogonal intersection caused a great loss of path-independence in the value of J integral up to 47% near the free surface. Thus in global situation, finite element analysis is not able to obtain an accurate stress state adjacent to the crack in the region close to the free surface, especially for cracks which are not normal to

surface.

In this thesis, BEM is used to study the effect of free surface on the state of stress at the crack vertex for a center cracked finite specimen under both static and dynamic conditions. Straight as well as curved crack fronts are analysed. Influence of Poisson's ratio and intersection angle of crack front with free surface on stress intensity factor along the crack front is studied.

Quasi-static analysis

Earlier studies have concentrated on calculation of stress singularity exponent on point of intersection of crack front with free surface and decay in value of energy release rate near free surface. This study capitalizes on the strength of BEM to calculate J_I^n integral more accurately near free surface as stresses and their gradients can be calculated more accurately using global boundary integral equations. Stress intensity factors can be calculated in BEM using traction values at the nodes along the crack front. A close correspondence between K_I computed from traction values and J_I^n integral is seen in this study. Thus, it is possible to relate the evaluated state of stress at the crack vertex, where crack front meets the free surface, with a value of SIF. At free surface, reduction in value of J_I^n up to a value of 50% of plane-strain value is estimated. Thickness of boundary layer where free surface effects are predominant is estimated. Critical intersection angle of crack front with free surface computed in this work for a finite center cracked specimen matches closely with the value predicted by the local FEM analysis of Bazant and Estenssoro for a half-space problem [2].

Stationary crack under impact loading

The three-dimensional time-domain displacement boundary integral formulation is implemented for analysis of a center cracked finite solid under symmetrically applied tensile step loading. A new partitioning scheme is proposed for spatial integration of elastodynamic kernels. Algorithm for calculating principal value integrals suggested by Guiggiani and Gigante [7] is extended to elastodynamic analysis. Also, combination of projection technique with semi-analytical integration, used for nearly singular integrals for static problems by Cruse and Aithal [8] and Mi and Aliabadi [9], is extended to elastodynamic problems.

In this thesis, variation of dynamic stress intensity factor (DSIF) along the crack front is studied. The state of stress is evaluated at the crack vertex, where crack front meets the free surface. The effect of free surface on DSIF is investigated. The effect of waves travelling in thickness direction is explained. It is possible to estimate accurately the

critical intersection angle of the crack front with the free surface at which square-root singularity is restored at the crack vertex under step loading.

Running crack under impact loading

The three-dimensional time-domain displacement boundary integral formulation is used for analysis of a moving center-crack in a finite solid under suddenly applied uniform normal pressure to crack faces. The algorithm used by Gallego and Dominguez [10] for running crack in 2-D analysis is extended to 3-D analysis in this thesis. The crack growth is modelled by using moving singular elements and a remeshing technique. For moving elements, space- and time-dependent interpolation functions are used.

Variation of dynamic stress intensity factor (DSIF) along the crack front is studied. The state of stress is evaluated at the crack vertex, where crack front meets the free surface. The effect of free surface on DSIF is investigated. It is again possible to estimate accurately the critical intersection angle of the crack front with the free surface at which square-root singularity is restored at the crack vertex under step loading for various speeds of crack propagation.

Main findings

- In earlier studies by Benthien [1] and Bazant and Estenssoro [2], local eigenvalue analysis was done for a quarter-plane crack in a semi-infinite half-space subjected to symmetric loading. This is the first study for a complete 3-D finite geometry problem that obtained the same critical intersection angle as obtained by Bazant and Estenssoro [2] for the half-space problem. This thesis establishes that LEF can explain 101° angle as critical angle of intersection for a Mode-I finite specimen.
- Main highlight of the thesis is bringing out the relevance of SIF directly calculated from crack front tractions and its correspondence with J_1^n integral values, especially near the free surface. This approach may facilitate study of free surface effect for more different problems. In FEM analysis, there is loss of path-independence in evaluation of J integral near the free surface. In this study, it is found that despite some mesh dependence, SIF value at the crack vertex, calculated from traction at the vertex, reflects the level of singularity at the vertex. Its value is sensitive to changes in vertex singularity brought about by changes in Poisson's ratio or angle of intersection of crack front with the free surface for the same level of mesh refinement.

List of papers communicated for publication

1. A study of free surface effects on through cracks using BEM - 'Engineering Fracture Mechanics' (accepted).
2. A study of free surface effects on through cracks under impact loading 'Engineering analysis with Boundary Elements' (accepted).
3. Free surface effect on moving crack under impact loading by BEM - 'Engineering analysis with Boundary Elements' (communicated).

Acknowledgements

I express my sincere gratitude to Prof. N. N. Kishore for his supervision, support and optimism during the course of this work. I am also thankful to Mrs. Kishore for her kind help at many an occasion and her affections for my daughters.

I am thankful to Prof. Vijay Gupta and Mrs. Gupta for their help at crucial moment and for contributing in making our stay in this campus livelier.

I thank Dr. V. B. Shenoy for many a helpful discussions and crucial help with LaTeX. I must add that interaction with him has been the most beneficial for me.

I am extremely grateful to the faculty of this Institute for some important courses learnt from them. I am thankful to Prof. V. Sunderrajan, Prof. A. K. Mallik, Prof. K. Ram, Prof. N. G. R. Iyengar, Prof. A. Mukherjee, Prof. V. Eshwaran and Prof. G. K. Lal for the courses I did with them.

I am thankful to Prof. B. Sahay, Prof. Prashant Kumar, Prof. S. G. Dhande and Prof. P. M. Dixit for their help during my PhD program.

I thank my friend Krishna for his help with some important papers on BEM and providing encouragement during the course of this work.

I thank my friends Ajay Amar, Sridhar and Mahesh for making me available some important papers.

I thank Sanat and Ranjana for their help and nice time spent with them. I also thank Venkat and Sharmilla for their help and good times.

I thank Rathore, Singhal, Ravi, Chandrasekhar, Samuel, Shashi, Sudhakar, Subro, Sukhbir, Muthup, Vimal for their help and lively time spent with them in this campus.

I am thankful to my lab staff Mr. Trivedi, Mr. Pandey, Mr. Avinash, Mr. Anurag, Mr. Divakar and Mr. Tewari for their help.

I am thankful to Mr. Nirmal Roberts, Dr. Tewari, Mr. Aftab Alam, Mr. Brajesh Pandey, Mr. PVK Reddy, Mr. Atul Kumar and Brahmaji for their help with computer systems.

I thank my sisters-in-law Neeru, Seema, Varsha and brothers-in-law Kishan, Sanjay, Deepak for their steady encouragement and help during the course of this work. I also thank my mother-in-law for her constant support and encouragement.

I thank my brothers Ashok, Arun, sisters-in-law Kamlesh, Vandana, sister Shail, brother-in-law Sudhir and my parents for their help and inspiration. I am thankful to my daughters Anubha and Aditi for their patience during this work and not allowing my spirits to dampen with their boundless charm.

Contents

Synopsis	v
List of Figures	xi
List of Tables	xxii
List of Symbols	xxv
1 Introduction	1
1.1 Overview of Linear Elastic Fracture Mechanics	
1.2 Overview of Dynamic Fracture Mechanics	
1.3 Advantages of BEM	1
1.4 Present work and layout of the thesis	1
2 TIME DOMAIN FORMULATION	1
2.1 Equations of three-dimensional elastodynamics	1
2.2 Boundary integral formulations in elastodynamics	1
2.2.1 Introduction	1
2.2.2 Dynamic Reciprocal Theorem	1
2.2.3 Fundamental solutions	1
2.3 Boundary Integral representation	1
2.4 Numerical treatment of boundary integral equations	2
2.4.1 Spatial discretization	2
2.4.2 Temporal and spatial interpolation of displacement and traction . .	2
2.4.3 Time-marching scheme	2
2.4.4 Analytical temporal integration	2
2.5 Spatial integration	3
2.5.1 Partitioning scheme	3

2.6	Evaluation of Principal-Value Integral	35
2.6.1	Quasi-singular integration	44
2.6.2	Detailed procedure for analytical integration	48
2.7	Quarter-point elements	53
3	Quasi-static Fracture Analysis	57
3.1	Introduction	57
3.2	The Boundary Element Method	59
3.3	BEM Crack Elements	61
3.4	J_1^n - integral	63
3.5	Numerical evaluation of boundary integrals	64
3.6	Results and Discussion	66
3.7	Conclusions	72
4	Dynamic Analysis: Stationary Crack	93
4.1	Introduction	93
4.2	Transient Boundary Integral Formulation	96
4.3	Numerical implementation	97
4.3.1	Temporal and spatial interpolation of displacement and traction . .	98
4.3.2	Analytical integration of temporal terms	99
4.3.3	Details of spatial integration	100
4.3.4	Crack Elements	103
4.4	Results and Discussion	104
4.5	Conclusions	109
5	Dynamic Analysis: Running Crack	127
5.1	Introduction	127
5.2	Analytical problem of self-similar, constant velocity, crack-propagation from a finite initial length	132
5.3	Transient Boundary Integral Formulation	133
5.4	Numerical implementation	134
5.4.1	Temporal and spatial interpolation of displacement and traction . .	135
5.4.2	Analytical integration of temporal terms	137
5.4.3	Spatial integration	137
5.4.4	Crack Elements	138

5.5	Formulation for a moving singular element	138
5.6	Finite-part integration	140
5.7	Details of moving mesh algorithm	141
5.8	Results and Discussion	143
5.9	Conclusions	147
6	Conclusions and Future Directions	173
6.1	Conclusions	173
6.2	Future Directions	174
	References	175

List of Figures

2.1	Quadrilateral element	24
2.2	Surface element enveloped by P- and S-waves emanating from \mathbf{y} at time t_m	31
2.3	Image in the parameter plane and polar coordinates	32
2.4	General vanishing neighbourhood around the source point	36
2.5	Image in the parameter plane of the boundary element and of the vanishing neighbourhood	40
2.6	The integration coordinate system.	45
2.7	Definition for the angular variable integration.	50
2.8	Nomenclature for angular transformation.	51
2.9	Quadratic quarter-point element	54
3.1	Crack front elements.	75
3.2	Contour and area surface for J_1^n	76
3.3	Distribution of internal points about the crack plane for J_1^n calculation.	77
3.4	Quarter-point element projected in the plane tangent to the nearest node.	78
3.5	Center-crack tension specimen.	79
3.6	Boundary Element Mesh.	80
3.7	SIF distribution along crack front for different meshes (Table 3.1).	81
3.8	Variation of J_C , J_A and J_1^n with radial distance of contour from crack front.	82
3.9	Variation of J_C , J_A and J_1^n with radial distance of contour from crack front.	83
3.10	Variation of J_C along crack front for different radial contours.	84
3.11	Variation of J_1^n along crack front.	85
3.12	Variation of K_I along crack front for different thicknesses of specimen for normal intersection.	86
3.13	Variation of K_I along crack front for different Poisson's ratios for normal intersection.	87

3.14	Variation of K_{II} along crack front for different Poisson's ratios for normal intersection.	88
3.15	Contours of plane strain constraint for the thick plate ($b/a = 2.166$).	89
3.16	Contours of plane strain constraint for the thin plate ($b/a = .091$).	90
3.17	Variation of K_I along crack front for different intersection angles of crack front with free surface.	91
3.18	Variation of K_I along crack front for different intersection angles, using only corner node SIF values.	92
4.1	Image in the parameter plane and polar coordinates	111
4.2	Center-crack tension specimen	112
4.3	Boundary Element Mesh	113
4.4	DSIF variation with time at crack vertex for different meshes (Table 4.1)	114
4.5	DSIF variation with time at mid-surface position on crack front for different meshes (Table 4.1)	115
4.6	DSIF variation along crack front for time instant $tc_1/h = 3.177$ for different meshes (Table 4.1)	116
4.7	Plots of $K_I(t)$ for different positions on the crack front for Mesh no. 4 (Table 4.1)	117
4.8	DSIF variation along the crack front at different instants of time, starting from the instant longitudinal wave strikes the crack face	118
4.9	Plot of x_1 -component of curl of displacement vector at an internal point with respect to time from the instant longitudinal wave strikes the crack face	119
4.10	Comparison of mid-surface $K_I(t)$ for different thicknesses of Mode-I specimen	120
4.11	Plots of $K_{II}(t)$ at different positions along crack front for Mode-II loading	121
4.12	Plots of $K_I(t)$ at crack vertex for different intersection angles of crack front with free surface	122
4.13	Plots of $K_I(t)$ at mid-surface for different intersection angles of crack front with free surface	123
4.14	Plots of $K_I(t)$ at different positions along crack front for intersection angle of 101°	124
4.15	Comparison of $K_I(t)$ at free-surface and mid-surface for intersection angles of 101° and 98°	125
5.1	⌘ Movement of the elements	151

5.2	Boundary Element Mesh	152
5.3	Quarter-point element projected in the plane tangent to the nearest node. .	153
5.4	Center-crack specimen	154
5.5	Plots of $K_I(t)$ at different positions on crack front for suddenly applied crack face pressure and comparison with analytical solution of problem of semi-infinite crack in an unbounded body	155
5.6	DSIF variation with time for different positions along the crack front for $v/c_R = 0.2$ (delay time $c_1\tau/h = 0.3177$)	156
5.7	DSIF variation with time for different positions along the crack front for $v/c_R = 0.4$ (delay time $c_1\tau/h = 0.3177$)	157
5.8	DSIF variation with time for different positions along the crack front for $v/c_R = 0.6$ (delay time $c_1\tau/h = 0.03177$)	158
5.9	DSIF variation with time for different positions along the crack front for $v/c_R = 0.8$ (delay time $c_1\tau/h = 0.03177$)	159
5.10	DSIF variation along the crack front for different instants of time for $v/c_R = 0.4$ (delay time $c_1\tau/h = 0.032$)	160
5.11	DSIF variation along the crack front for different instants of time for $v/c_R = 0.8$ (delay time $c_1\tau/h = 0.032$)	161
5.12	DSIF variation along the crack front for different instants of time for $v/c_R = 0.8$, using only DSIF values at corner nodes of the elements on crack front	162
5.13	DSIF variation along the crack front for different instants of time for $v/c_R = 0.8$, using only DSIF values at mid-side nodes of the elements on crack front	163
5.14	DSIF variation with time at crack vertex for different speeds of crack propagation (delay time $c_1\tau/h = 0.3177$)	164
5.15	DSIF variation with time at mid-surface for different speeds of crack propagation (delay time $c_1\tau/h = 0.3177$)	165
5.16	DSIF variation with time at crack vertex for different speeds of crack propagation (delay time $c_1\tau/h = 0.03177$)	166
5.17	DSIF variation with time at mid-surface for different speeds of crack propagation (delay time $c_1\tau/h = 0.03177$)	167
5.18	Direction of crack advance parallel to free surface to achieve self-similar profile	168
5.19	Plots of $K_I(t)$ at crack vertex for different intersection angles of crack front with free surface (delay time $c_1\tau/h = 0.3177$)	169

5.20	Plots of $K_I(t)$ at mid-surface position for different intersection angles of crack front with free surface (delay time $c_1\tau/h = 0.3177$)	170
5.21	Plots of $K_I(t)$ with time for different positions along crack front for intersection angle of 101° (delay time $c_1\tau/h = 0.3177$)	171

List of Tables

3.1	Mesh characteristics for Mode-I runs with straight crack front.	74
4.1	Mesh characteristics for Mode-I runs with straight crack front.	110
5.1	Values of the Freund [11, 12] slowness function $S_+(1/v)$ for various crack speeds v for Poisson ratio $\nu = 0.3$	149
5.2	Mesh characteristics for Mode-I runs with straight crack front.	150

LIST OF SYMBOLS

a	half-length of crack
b	half-thickness of center-crack specimen
c_1	Elastic dilatational wave speed
c_2	Elastic shear wave speed
c_R	Elastic Rayleigh wave speed
e_i	Unit vector in one of the Cartesian directions
E	Young's elastic modulus
G	Energy release rate; dynamic energy release rate
h	half-height of center-crack specimen
G_{ij}	Stoke's displacement fundamental solution or kernel
$H(t)$	Heaviside or unit step function
H_{ij}	Stoke's traction fundamental solution or kernel
J	J-integral
$J(\xi_1, \xi_2)$	Jacobian of transformation in three-dimensional problems
J	Jacobian of transformation; J-integral
J_1^n	J-integral defined for three-dimensional elastic configurations
$k(v)$	Universal function of crack tip speed for elastic crack growth in mode I
K_I	Elastic stress intensity factor for mode I (similar for mode II and III)
$l, l(t)$	Crack length; amount of crack growth
\dot{l}	Instantaneous crack tip speed
n_i	Components of unit vector; normal to surface or curve
$N_c(\xi_1, \xi_2)$	Quadratic shape functions ($c = 1, 2, \dots, 8$)
$o(f(x))$	Asymptotically dominated by f as $x \leftarrow$ a limit point
$O(f(x))$	Asymptotically proportional to f as $x \leftarrow$ a limit point
$r(P, Q)$	Distance between points P and Q
S	Surface in three-dimensional problems
S_{kij}	Third-order tensor multiplying the displacement vector
$S_{\pm}(\zeta)$	Factors of the Rayleigh wave function that are nonzero and analytic in overlapping half planes
t	Time coordinate
t_i	Components of traction vector
T	Time coordinate
T_{ij}	Kelvin's traction fundamental solution or kernel
u_i	Components of particle displacement vector ($i = 1, 2, 3$ or $i = x, y, z$)
\dot{u}_i	Components of particle velocity vector
\ddot{u}_i	Components of particle acceleration vector
U_{ij}	Kelvin's displacement fundamental solution or kernel

v	Crack front speed
V	Volume in three-dimensional problems
w	half-width of center-crack specimen
w_i	Weight function in ordinary Gaussian quadrature
x_i	Rectangular coordinates ($i = 1, 2, 3$)
x, y, z	Rectangular coordinates
Γ	Crack tip contour; Surface or boundary in two-dimensional problems
$\delta(t)$	Dirac delta function
δ_{ij}	Kronecker's delta
ϵ	A small real parameter
ϵ_{ij}	Components of the small strain tensor
ξ_i	Local Intrinsic coordinates ($i = 1, 2$)
η_i	Local Intrinsic coordinates ($i = 1, 2$)
λ	Lamé elastic constant
μ	Lamé elastic constant; elastic shear modulus
ν	Poisson's ratio
Ω	Domains
ρ	Material mass density; Polar radial coordinate
σ_{ij}	Components of the stress tensor
σ_∞	Magnitude of remotely applied normal traction
σ_o	Magnitude of applied normal traction
τ	Time coordinate
τ_o	Magnitude of applied shear traction
θ	Polar angular coordinate

Chapter 1

Introduction

In the theory of elasticity, two types of two-dimensional problems are recognised: one of plane stress and one of plane strain. A state of plane stress is approached in a very thin bar without discontinuities in tension or compression. A state of plane strain is approached in the central transverse section of an infinitely long cylinder subjected to uniform loading along a line parallel to its axis. In dynamic situations, a plane strain case is obtained if the wavelength is small compared with all dimensions of the body of material in which the waves travel. A plane stress case is obtained if the waves are propagated in a plate such that the wavelength is large compared with the thickness of the plate.

When a thin bar in tension has a discontinuity, such as a hole, groove or crack, the state of stress may be affected by the discontinuity. It is both of theoretical and practical interest to examine the effect of the thickness on the state of stress resulting from such discontinuities. Approximate theories of thin plates are unreliable in the case of plates of considerable thickness, or when the plates are weakened by cavities whose dimensions are of the same order of magnitude as the plate thickness. In such cases, the stress variations in the thickness direction must be accounted for and the problem adopts a three-dimensional character.

The stress distribution in a thick plate containing a smooth circular cavity has been discussed by Sternberg and Sadowsky [13]. Inner layers are seen to carry a somewhat greater stress than the outer layers of the bar. Their work showed that the thickness of the plate can exert appreciable influence on the stress concentrations of the circular hole. When the periphery of the cavity contains re-entrant corners or singular points, such as a sharp crack, the problem is considerably more difficult mainly because the conventional mathematical techniques are not suitable for handling 3-D problems with geometric singularities. Also, the stress distribution in a cracked plate of finite thickness is neither in a

state of plane stress or plane strain nor generalized plane stress.

Hartranft and Sih [14] considered a through-the-thickness crack intersecting normally to the free surfaces in a finite size plate. They defined a boundary thickness β near the free surface by an empirical equation $\beta = t/(4 + 16t/a)$ in which the square-root singularity is not valid. In this equation, t is the thickness of the plate and $2a$ is the crack length. But they did not analyse the state of stress in boundary layer region near the crack vertex. Crack vertex is the corner point where the crack front intersects the free surface for a through-thickness crack.

Yang and Freund [15], motivated by concerns regarding experimental measurements made in the vicinity of the crack tip, explored the 3-D crack problem using a boundary layer approach. They studied the state of stress in a thin plate which contained through cracks with a view toward assessing the influence of transverse shear on the crack tip stress and deformation fields. Their boundary layer solution showed a smooth transition from the near-tip generalized plane strain solution to plane-stress solution at distances from the crack tip ' r ' of $1/2$ to $3/4$ of plate thickness ' h ' depending on the value of Poisson's ratio. There is a zone around the crack edge where three-dimensional effects influence the state of stress. They stated that the plane stress assumption is typically valid only for $r > h/2$.

Rosakis and Ravi-Chandar [16] studied the extent of the region of three-dimensionality of the crack-tip field using reflected and transmitted caustics. They found that plane stress conditions prevail at distances from the crack-tip greater than half the specimen thickness, while no significant plane strain region was detected by them.

Yang and Freund [15] and Rosakis and Ravi-Chandar [16] were concerned about the extent of zone of influence of three-dimensional effects around the crack edge so as to identify the regions in which local experimental measurements based on two-dimensional theory can be performed with confidence. But they did not study the effect of free surface on state of stress at the crack vertex. When a crack front intersects a free surface, elastic analysis and experiment suggest that the inverse-square root singularity of LEFM is altered. Benthem [1] analyzed a problem of a quarter-plane crack in a semi-infinite half-space subjected to symmetric loading. He derived that at the corner point, stresses have $r^{-0.452}$ singularity for Poisson's ratio ν equal to 0.3. Although it does not seem a dramatic change, it implies that the stress intensity factor at this point is equal to zero (or does not exist) since it is defined as the strength of the square-root singularity at the crack tip. It also causes the energy release rate to be equal to zero, since this can have a bounded, non-zero value only in the case of an exact r^{-1} singularity of the strain energy. Bažant

and Estenssoro [2] confirmed Benthem's values for the singular eigenvalue at the crack vertex through a 3-D finite element analysis developed for conical regions. In addition, they considered intersections other than normal and found angles at which square-root singularity is restored. They used extrapolation procedures to estimate singularity indices corresponding to infinite degrees of freedom from results of eigenvalue analysis of a set of uniform grids. By a finite element formulation similar to that used by Bažant and Estenssoro [2], Gudmundson and Östlund [3] found that a weaker singularity also exists at the corner point for a dynamically growing crack and estimated the critical angle to be 101° for $\nu = 0.3$, almost independent of the crack-tip velocity. The success enjoyed by these local numerical analyses for half-space problems is not found to the same extent in finite element treatments of more global or complete problems (i.e., finite bodies) which contain crack/surface intersections. Different predictions were made concerning the variation in energy release rate (G) with some results showing an increase in G in the free surface region, some a decrease and still others no change. Burton *et al.* [4] used a special set of integral equations for an elastic half-space weakened by a crack of finite width and infinite depth subjected to transverse excitation. They confirmed the existence of a weaker singularity at global crack/surface intersections with both integral equation formulation and finite element analysis of a finite geometry with adjustable singularity index at the crack vertex. They found by FEM a decay of G as free surface is approached ($z/a \rightarrow 0$) with the drop between the maximum value and that of the closest Gauss point (at $z/a = 0.015$) to the free surface being 30% of plane-strain value G_p when Poisson's ratio is 0.4. Nakamura and Parks [17] estimated thickness of boundary layer region, where free surface effects are predominant, as 3% of plate thickness. They used domain integral method to calculate local energy release rate J and calculated a drop in value of J of the order of 30% of two-dimensional plane-stress value of J near the crack vertex. In FEM, calculation of J-integral at various positions along the crack front is constrained by the fact that accurate values of stresses are available only at Gauss points of the elements. Hence accurate determination of thickness of boundary layer at free surface becomes difficult as it requires having very thin elements near the free surface.

It can be observed in experiments that an initially straight-fronted crack in specimens such as a compact-tension specimen usually grows to a slightly curved shape under a fatigue load [5]. Using local eigenvalue analysis with FEM, Bažant and Estenssoro [2] found the critical intersection angle to be 101° , a value also observed experimentally [5] for $\nu = .3$. Three-dimensional LEFM implies that for $\nu \neq 0$ the straight profiles associated with the

varying energy release rates would not propagate as such but rather take up curved profiles with constant energy release rates. Burton *et al.* [4] generated critical crack profiles using FEM with each profile having less than 2% numerical variation in G with depth. The crack profiles generated by them were significantly less curved than those observed in practice [5]. Similarly, using FEM, Bakker [18] predicted a relative tunnelling depth of 2.5 – 3% based on constant stress intensity distributions for self-similar crack propagation. Experimentally observed tunnelling depths on fatigue cracks are generally larger, closer to 5%, which is close to circular front. Using FEM for analysis, Lin and Smith [6] found that slightly non-orthogonal intersection caused a great loss of path-independence in the value of J-integral up to 47% near the free surface. Thus, in finite geometry situation, finite element analysis is not able to obtain an accurate stress state adjacent to the crack front in the region close to the free surface, especially for cracks which are not normal to the surface.

Burton *et al.* [4] surmised that the underlying theoretical assumptions and developments in LEFM were to a degree incapable of explaining all of the various phenomena actually present in retardation of crack front near the free surface. Bakker [18] mentioned the need of invoking plasticity and crack closure effects to explain free surface retardation. On the other hand, for quasi-brittle behaviour with only small-scale yielding, Smith [19] found that cracks identical in shape to those in fatigued metal models could be grown under monotonic loads (R = ratio of minimum K_I to maximum $K_I = 1.0$) in photoelastic bodies suggesting that closure effects might not strongly affect crack shapes.

The calculation of SIF in two dimensions (for virtually arbitrary configurations) is commonplace today. In three-dimensions, the case is slightly different. Existing methodology is sufficient for the solution of Mode-I problems provided the intersection of crack fronts with free surfaces is avoided and provided the crack front does not exhibit abrupt changes in curvature. The problems of brittle fracture involving intersection of the crack fronts with the free surfaces still require extremely careful examination.

The boundary element method (BEM) is already established as an economical and accurate numerical technique for elastic stress analysis. It is particularly suitable for problems that are 3-D and involve high local stress gradients, such as those encountered near cracks. It is possible to obtain higher resolution of interior stresses and their derivatives with BEM. The high accuracy of BEM makes it possible to analyse accurately the effect of free surface on the state of stress at the point of intersection of crack front with the free surface in this work.

1.1 Overview of Linear Elastic Fracture Mechanics

A number of books and monographs are available to provide background on fracture mechanics from various perspectives. For example, the books by Broek [20], Kanninen and Popelar [21], Cherepanov [22], Hellan [23] and Kumar [24] develop the topic from the mechanics perspective. The books by Knott [25] and Lawn [26] introduce the subject from the mechanics perspective, whereas Barsom and Rolfe [27] discuss fracture within the context of materials selection and structural applications.

Fracture mechanics is concerned with the quantitative description of the mechanical state of a deformable body containing a crack or cracks with a view toward characterizing and measuring the resistance of materials to crack growth.

There being multiple flaws in real material, the growth of the most dangerous of which leads to fracture. Griffith [28] explained why the strength of real materials is from 2 to 3 orders of magnitude lower than the theoretical strength implied by the perfect crystal structure of bodies. Though Griffith's analysis referred to sub-molecular size of micro-cracks, his technique could be simply extended to any macroscopic level by suitable redefinition of specific constants like surface energy of the material. Irwin [29] and Orowan [30] extended Griffith's theory to micro-cracks in steel and proposed the concept of quasi-brittle fracture. They included the region of irreversible strains near a crack edge into the surface of fracture and introduced the concept of effective surface energy which includes plastic work. This made it possible to consider fractures within the framework of the model of an ideally brittle body.

Continuum field approach to fracture of solids was launched with the introduction of the elastic stress intensity factor, K , as a crack tip field characterizing parameter by Irwin [31]. This idea provided an alternate framework for discussing the strength of cracked solids of nominally elastic material. Irwin proposed that a crack will begin to grow in a cracked body with limited plastic deformation when K is increased to a value called the fracture toughness of the material.

The crack tip region is said to be autonomous at fracture initiation or during crack growth if

1. The extent of the region of nonlinearity from the crack edge is very small compared to all other length dimensions of the body and loading system.
2. The mechanical state within this end region at incipient growth or during growth is independent of loading and geometrical configuration.

For the particular case of an elastic-plastic material, the property of autonomy implies that the crack tip plastic zone is completely surrounded by an elastic SIF field and that the state of stress within the plastic zone is determined by the level of stress intensity of the surrounding field. This situation, which was termed small-scale yielding by Rice [32], is the situation in which SIF is a useful fracture characterizing parameter.

It may be noted that a stress distribution with an infinite singularity is clearly a mathematical idealization, in that no real material can actually support such a stress. The rationalization for admitting the singular stress distribution, the strength of which is measured by the SIF, is based on the concept of small-scale yielding. It is thus assumed that in the immediate vicinity of the crack tip, the potentially large stresses are relieved by some nonlinear process in a region whose dimensions are small compared to crack length and body dimensions. It is assumed further that the stress distribution in the elastic material adjacent to the small zone is adequately described by the dominant singular term in the elasticity solution. Under small-scale yielding conditions, the SIF may be considered to be a one-parameter measure of the amplitude of the stress which is being applied to the material in the crack tip region. The SIF approach circumvents consideration of how the material in the crack tip region actually responds to the applied stress.

Fracture mechanics is devoted to determining SIF or energy release rate for various conditions. For Mode-I loading, the components of stresses near the crack edge can be represented asymptotically as

$$\sigma_{ij} \sim \frac{K_I}{\sqrt{2\pi r}} f_{ij}(\theta) \quad (1.1)$$

Asymptotic solutions show

1. universal spatial dependence
2. All information about loading and configuration are embedded in the scalar multiplier called SIF.

1.2 Overview of Dynamic Fracture Mechanics

A few comprehensive books and monographs on dynamic fracture mechanics, notably, are Freund [12], Parton and Boriskovsky [33,34] and Broberg [35]. Dynamic fracture mechanics is the subfield of fracture mechanics concerned with fracture phenomena for which the role of material inertia becomes significant. Inertial effects can arise either from rapidly applied loading on a cracked solid or from rapid crack propagation. In the case of rapid loading,

the influence of the loads is transferred to the crack by means of stress waves through the material. To determine whether or not a crack will advance due to the stress wave loading it is necessary to determine the transient driving force on the crack.

Quasi-static fracture mechanics gives the answer to the question of whether or not the crack will grow catastrophically. The scope of dynamic fracture mechanics is much wider. Quasi-static fracture mechanics formulates only the criterion of unstable crack propagation whereas dynamic fracture mechanics requires the formulation of a series of criteria—those for crack initiation, crack propagation, crack arrest, bending of crack trajectory, and crack branching. Some basic problems of dynamic fracture mechanics can be listed as follows:

1. Establishment of the frequency dependence of stress intensity factor for a crack subjected to harmonic loading.
2. Establishment of temporal dependence of stress intensity factors for a crack under impact loading.
3. Establishment of the dependence of stress intensity factors on time and crack propagation velocity.
4. Establishment of the law of crack propagation for a known dependence of the stress intensity factors on the crack propagation velocity.

Theoretical treatments by Yoffe, Broberg and others show that the nature of the near field about the tip of a propagating crack changes with velocity (see Freund [12]). The stresses can be represented in the form analogous to formula (1.1) with the only difference—now the stress intensity factors depend on time whereas the angular stress distribution depends on the velocity, i.e.,

$$\sigma_{ij} \sim \frac{K(t)}{\sqrt{2\pi r}} f_{ij}(\theta, v) \quad (1.2)$$

The stress intensity factor in an impact loading substantially exceeds its static value in the transient period. Freund, in his series of papers [11, 36], established the universal analytic methods for evaluation of the transient stress intensity factor of a crack in a two-dimensional geometrical configuration under dynamic loading. One of his major conclusions was that the stress intensity factor of a half-plane running crack is given by the product of the universal function of crack-tip velocity and the stress-intensity factor for an equivalent stationary crack [36].

The most popular model of dynamic fracture mechanics deals with growth of a rectilinear crack in an elastic plane. It is assumed that the energy consumed during the formation

of the unit area of a new surface is a material characteristic. The elastodynamic stress field at the crack tip is calculated to formulate the criterion of crack propagation as an equation of energy balance.

Thus, the idealized model of dynamical fracture mechanics is based on two main principles:

1. Stress fields at the crack tip are described in terms of stress intensity factors.
2. The criteria of the crack start, arrest and propagation are derived from the energy balance equation.

Thus, to verify the accuracy of the model to a real process, it is necessary to check the validity of these two statements. With this aim, one can analyse the experimental data on stress intensity factors and then compare the necessary experimental conditions for crack initiation, propagation and arrest with the corresponding theoretical predictions.

In most experiments, correspondence between the SIF's and the crack propagation velocity turns out to be non-unique. At low loading rates and moderate loads, there is good agreement between the theoretical and experimental stress intensity factors, which is absent for high loading rates and intense loading.

Qualitative explanation of such a discrepancy can be seen if it is assumed (and it is confirmed experimentally) that fracture occurs not at the crack tip itself, but in a certain zone ahead of the crack tip because of a complex process of appearance of micro-cracks, their mergence, and interaction. The existence of such a zone was clearly demonstrated on a brittle acrylic plastic [37].

Ravi-Chandar and Knauss [38] had observed with high speed micrography that the fractured surface formed upon propagation of a crack with a high velocity has three different regions: mirror-smooth, matt, and hackle zones. Upon passing the hackle zone, the crack starts branching. The mirror-smooth zone is characterized by a smooth light-reflecting surface. In the matt zone the, surface becomes more coarse and in the last hackle zone it becomes rough. It is observed that with an increase in loading the size of the mirror-smooth zone decreases, whereas those of the matt and hackle zones increase. On the contrary, a decrease in the loading level increases the mirror-smooth zone and decreases the matt and hackle zones.

When a single crack propagates in the mirror-smooth zone, its behaviour only slightly deviates from the quasi-static growth. In the matt zone, a whole ensemble of cracks propagates simultaneously. In the hackle zone, the crack propagation is still of the same

physical nature but the zone of micro-cracking becomes substantially larger. Thus, it is possible to state that crack propagation under high stresses is controlled by the development of micro-cavities and micro-cracks, their accumulation, mergence, and interaction [38].

Under conditions of low stress intensity, the crack front exhibits ‘thumbnail’ curvature similar to the crack profiles associated with quasi-static fracture processes. At increasing stress intensity the crack front straightens out and is identifiable as a front of multiple micro-fractures [39]. In the ‘mirror’ zone, crack propagates in the plate with a curved front. In the ‘mist’ and ‘hackle’ zones, the ensemble crack front is no longer curved as in the ‘mirror’ zone.

Parton [37] experimentally observed that if crack velocity exceeds a certain value, then the arrival of waves reflected from the free boundaries to the crack tip does not affect its velocity, implying that the zone of process occurrence has a certain inertia, i.e., it shows some resistance to the ‘attempts’ to change its velocity. Based on the boundary element analysis in this study, it seems to the author that beyond a certain crack velocity, crack behaviour undergoes a distinct change or inertial terms start dominating the square-root singular terms. The possibility that the extent of the stress intensity factor during dynamic crack growth under transient conditions is more limited than a steady-state analysis would indicate was first suggested by the analysis of Ma and Freund [40]. Under severe transient conditions, the local crack tip field is not accurately represented by a stress intensity factor field. At higher crack speeds, the higher-order terms in the near-field asymptotic expansion can have a significant influence on the crack tip stress field [41] even for the case of constant crack speed, following fracture initiation.

During the early stages of crack growth, the other terms may dominate the square root singular term under certain conditions. During the early phase of crack growth, the transient nature of stress field prevents a complete stress intensity factor from becoming established outside the near-tip three-dimensional zone. This feature erodes the value of the stress intensity factor concept in characterizing the fracture resistance of the material. Though a unique plane stress intensity factor can be identified in both the data and the model at each instant of time, even though no fully developed stress intensity factor field is apparent. However, this stress intensity factor is not strictly relevant in the spirit of fracture toughness testing.

A long-standing issue of fundamental importance in dynamic fracture research is the connection between the dynamic fracture toughness and the crack tip velocity. The debate, for the most part, has centered around the question of uniqueness of a relationship between

K_I^d and v . Kobayashi and Dally [42], Rosakis *et al.* [43] and Zehnder and Rosakis [44], among others, provided data sets that seem to indicate that $K_I^d - v$ relation is reasonably viewed as a material property. On the other hand, the results of Kobayashi and Mall [45] and Ravi-Chandar and Knauss [39], based on photo-elasticity and the method of caustics in transmission, respectively, suggest that there is no such correspondence. The fundamental difficulty of achieving a well-developed stress intensity factor field may be playing a significant role in these differences in results.

For a crack under suddenly applied uniform crack face pressure, Ma and Freund [40] found that for a stationary crack, stress intensity factor field is found only for points closer to the crack tip than about 5–10 percent of the distance to the cylindrical shear wave front, implying that the extent of the K field is so small at the onset of growth. They found that measured and calculated stress intensity factor histories compare very well for relatively low crack face pressures, but there is significant disagreement beyond crack growth initiation for higher pressures. The time required, before the singular stress becomes a good estimate of the total stress, decreases as the delay time increases. Delay time is the time between the onset of crack growth and the time instant when pressure is suddenly applied on the crack face. The problem may also lie in the assumption of linear elastic material response. Both the analysis and the models that underlie the interpretations of these experiments are two-dimensional in nature. In either case, the three-dimensional effects that are overlooked may have too much of an influence to be neglected in considering the process [40].

Conditions of K_I^d dominance exist either extremely close to the crack-tip or are eventually established at long times after crack initiation. However, the higher order transient asymptotic representation is more successful in describing the actual field even at times close to the event of crack initiation or at distances relatively far away from the moving crack tip. The transient effect is manifested through the time derivative of the dynamic stress intensity factor even if the crack-tip speed is constant.

It is necessary to apply the higher order asymptotic expansion which includes the transient history of the crack growth to describe the near tip deformation fields. Also the crack growth is indeed controlled by a material related criterion. This criterion gives the unique relationship between the dynamic fracture toughness K_{IC}^d and the crack-tip speed v . The existence of such a criterion was seen validated in a simulation by Liu and Rosakis [46] by using the higher order transient expansion, while the lack of the uniqueness of a relationship between K_{IC}^d and v has been observed when the K_I^d -dominant assumption or the steady state higher order expansion is used [39, 45].

In the present study, the author has investigated if it is possible to capture this loss of square-root dominance by the boundary element analysis. SIF is calculated from crack-tip or crack front tractions in BEM. Value of traction at a node on crack front exhibits an integrated influence of level of singularity over the elements adjoining it. Any weakening of singularity, for example at crack vertex, or loss of dominance of square-root terms at high speeds of crack propagation gets reflected in the value of SIF calculated from nodal tractions.

In the past three decades, the application of the finite element method (FEM) to dynamic crack propagation has made important advances. Interesting reviews can be found in the papers by Aoki *et al.* [47] and by Atluri and Nishioka [48]. Two different approaches followed are based on one of the following two concepts: a stationary mesh, which includes a 'node release' mechanism, or a moving mesh which normally includes a singular element.

The BEM has appeared as an alternative for elastic fracture mechanics problems. This method seems to be a better choice than FEM for elastodynamic fracture mechanics because the discretization is restricted to the boundary surface and the concept of singular element is simplified. In particular when dealing with dynamic crack propagation, the remeshing is conceptually much simpler in BEM than in any domain technique. Classical methods like finite difference method or FEM are difficult to apply to the study of crack growth because of their intrinsic numerical dissipation of high frequency elastic waves.

1.3 Advantages of BEM

The BEM is a numerical technique based on integral equation formulations of the continuum mechanics problems. There are two types of integral equation formulations. One contains, as basic unknowns, quantities with a clear physical meaning and in terms of which boundary conditions are given. This type is called the direct formulation. In the second type, known as indirect formulation, the basic unknown quantities have no physical meaning. The physical variables are obtained from these sources. In this thesis, numerical approach used is based on direct formulation.

There are some general characteristics of the BEM which represent clear advantages for the analysis of static and dynamic continuum mechanics problems. First of all, the problem is formulated on the boundary. Therefore, only the boundary has to be discretized as opposed to domain techniques, such as the Finite Element Method (FEM) and the Finite Difference Method (FDM) which require the discretization of the domain. As a conse-

quence, the resulting system of equations is smaller in the BEM. Another consequence is that the mesh generation process, which only involves the surface, is simpler than in domain type methods. This advantage is important for situations where the geometry changes throughout the solution process, for example, crack propagation studies. But the final system of equations is non-symmetric and fully-populated. This fact may lead to longer computer times, as compared to finite element solutions, in some types of problems. A second characteristic of the BEM is that it produces highly accurate solutions on the boundary and in particular at any selected internal point. This feature makes the methods very appropriate for problems where very high accuracy is required. Among the disadvantages of the BEM, its difficulty in dealing with non-linear material properties is prominent. In such cases the integral equations include domain integrals and the advantages of a boundary formulation vanish if extensive zones of non-linear material exist.

There is an additional important difference between the BEM and the domain type numerical methods. When dealing with infinite or semi-infinite regions, the domain numerical methods require a discretization which should extend towards infinity. Obviously, the discretization has to be finished at a certain distance where an artificial boundary of some kind is located. These boundaries can be used without problems in statics. In dynamics, however, spurious reflections of waves which distort the solution of the problem take place at the artificial boundaries. On the contrary, the BEM is based on the integral equation formulation, which in the case of external regions, consist of integrals extending only over the internal boundaries. Therefore, those are the only boundaries to be discretized. The behaviour of the boundless domain is 'naturally' represented by those integrals over the internal boundaries.

The BEM has special suitability for problems of fracture dynamics. Its capability to model steep stress gradients is the main motivation for its use in this study to analyse free surface effect for through cracks for both static and dynamic conditions.

1.4 Present work and layout of the thesis

The objective of the present work is to investigate the effect of free surfaces on fracture characteristics for elastostatic and elastodynamic problems using three-dimensional boundary element method. Free surface effect is studied for a through center cracked finite body for three situations: quasi-static conditions, stationary crack under impact loading and running crack under impact loading. The thesis has six chapters and each of them is a self-contained unit.

In Chapter 2, the three-dimensional direct time-domain displacement formulation is described. Software developed on the basis of this formulation has been used to get the results of the next chapters.

In Chapter 3, the effect of free surfaces on fracture characteristics for elastostatic problems is discussed. Stress intensity factors are calculated along the crack front for a through center crack specimen using nodal traction values at the crack front. Correspondence of these stress intensity factors with values of J_1^n -integral is studied all along the crack front. Free surface retardation of crack front is studied for incipient self-similar crack growth and critical intersection angle of the crack front with the free surface is estimated.

In Chapter 4, the effect of free surfaces on fracture characteristics for a stationary crack under impact loading is discussed. The variation of dynamic stress intensity factors with time is studied along the crack front. The effect of waves travelling in thickness direction is probed. Also free surface retardation of crack front is studied for incipient self-similar crack growth and critical intersection angle of the crack front with the free surface is estimated under step loading.

In Chapter 5, the effect of free surfaces on fracture characteristics for a running crack under impact loading is discussed. Formulation of a moving singular element for three-dimensional modelling is described. Variation of dynamic stress intensity factors is studied for low and high crack speeds. Free surface effect on DSIF variation at crack vertex and other positions on the crack front is studied for straight and curved crack fronts. Also critical intersection angles are estimated.

Chapter 6 presents the main conclusions of this study and guidelines for future work.

Chapter 2

TIME DOMAIN FORMULATION

This chapter describes the direct time-domain displacement formulation used in this thesis. First of all, the general equations governing linear elastodynamics are briefly described. Thereafter, boundary integral formulation is given along with detailed numerical implementation procedures. Temporal and spatial integration of terms involving displacement and traction kernels are described in detail.

The detailed formulation is given for the sake of completeness. All peculiarities of the method used have been brought out in the description. Time domain formulation is a well-developed formulation and its details can be seen in several texts [49, 50]. In this thesis, a new partitioning scheme is proposed for spatial integration of elastodynamic kernels. Algorithm for calculating principal value integrals suggested by Guiggiani and Gigante [7] is extended to elastodynamic analysis. Also, combination of projection technique with semi-analytical integration, used for nearly singular integrals for static problems by Cruse and Aithal [8] and Mi and Aliabadi [9], is extended to elastodynamic problems.

2.1 Equations of three-dimensional elastodynamics

The basic equations of linear elastodynamics are:

1. the equations of motion

$$\sigma_{ij,j} + \rho b_i = \rho \ddot{u}_i \quad (2.1)$$

2. the kinematical relationships

$$\epsilon_{ij} = \frac{1}{2}(u_{i,j} + u_{j,i}) \quad (2.2)$$

3. the constitutive law

$$\sigma_{ij} = \lambda \epsilon_{kk} \delta_{ij} + 2\mu \epsilon_{ij} \quad (2.3)$$

Also the balance of angular momentum implies that the stress tensor is symmetric ($\sigma_{ij} = \sigma_{ji}$). In the above, $u_i(\mathbf{x}, t)$ are the components of displacement vector at point \mathbf{x} and time t , σ_{ij} and ϵ_{ij} are the components of stress and strain tensors respectively, and b_i is the body force per unit mass. Furthermore, λ and μ are the Lamé's constants and ρ is the mass density. Kronecker's delta δ_{ij} is equal to unity if $i = j$ and zero if $i \neq j$. The Cartesian coordinate system ($i, j = 1, 2, 3$) is used here. Light-faced letters stand for scalars while letters in boldface denote vectors and second-order tensors.

Above equations can be combined to give the Navier-Cauchy equations

$$(\lambda + \mu) u_{j,ji} + \mu u_{i,jj} + \rho b_i = \rho \ddot{u}_i \quad (2.4)$$

which are the governing equations for an elastic, isotropic and homogeneous solid of volume V and surface S . By defining the propagation velocities of the pressure (dilatational) and shear (rotational) waves in the solid as $c_1^2 = (\lambda + 2\mu)/\rho$ and $c_2^2 = \mu/\rho$, respectively, equation(2.4) can be written as

$$(c_1^2 - c_2^2) u_{j,ij} + c_2^2 u_{i,jj} + b_i = \ddot{u}_i \quad (2.5)$$

Equation of motion is accompanied by initial conditions

$$u_i(\mathbf{x}, 0) = u_{i0} \quad (2.6)$$

$$\dot{u}_i(\mathbf{x}, 0) = v_{i0} \quad (2.7)$$

in V and boundary conditions

$$u_i(\mathbf{x}, t) = U_i, \quad \mathbf{x} \in S_1 \quad (2.8)$$

$$t_i(\mathbf{x}, t) = \sigma_{ij} n_j = T_i, \quad \mathbf{x} \in S_2 \quad (2.9)$$

on S , where t_i are the tractions, $n_j(\mathbf{x})$ is the outward-pointing normal vector and U_i and T_i are prescribed values for displacements and tractions respectively.

It is assumed that u_i and its derivatives up to second order are continuous except at propagating wavefronts, where only u_i is continuous. On these fronts, both the kinematic jump condition

$$[\dot{u}_i] = -c n_k [u_{i,k}] \quad (2.10)$$

and the momentum condition

$$[t_i] = -\rho c [\dot{u}_i] \quad (2.11)$$

must be satisfied [51]. In the above two equations, brackets denote difference in the enclosed quantity between front and back surfaces of the discontinuous front travelling with velocity c .

2.2 Boundary integral formulations in elastodynamics

2.2.1 Introduction

The mathematical basis for all direct integral equation formulations in elastodynamics is the dynamic reciprocal theorem. It is not, however, the only method; the same result can be accomplished via Green's function method, variational principles, or weighted residuals. A system of constraint equations between the boundary quantities is generated by moving the field point about the surface. In order to solve engineering-type problems, discretization of the surface is necessary. Subsequent numerical processing of the boundary integral equations gives rise to the Boundary Element Method (BEM).

2.2.2 Dynamic Reciprocal Theorem

The reciprocal theorem in dynamics specifies a relationship between a pair of elastodynamic states. It is essentially the dynamic extension of the classical reciprocal theorem of Betti-Rayleigh in elastostatics, augmented by the inertia forces. This theorem was stated by Graffi [52] in its present form for bounded regions using Laplace transformations. Rigorous proofs for unbounded regions were given by Wheeler and Sternberg [53]. The reciprocal theorem first specifies a regular region V in the sense of Kellogg [54] with boundary S and material properties ρ , c_1 and c_2 . Consider two distinct elastodynamic states $A = [u_i, t_i, b_i]$ and $B = [\tilde{u}_i, \tilde{t}_i, \tilde{b}_i]$ defined in that region and with initial conditions

$$u_i(\mathbf{x}, 0) = u_{io}(\mathbf{x}) \quad (2.12)$$

$$\dot{u}_i(\mathbf{x}, 0) = v_{io}(\mathbf{x}) \quad (2.13)$$

$$\tilde{u}_i(\mathbf{x}, 0) = \tilde{u}_{io}(\mathbf{x}) \quad (2.14)$$

$$\dot{\tilde{u}}_i(\mathbf{x}, 0) = \tilde{v}_{io}(\mathbf{x}) \quad (2.15)$$

Then, for $t \geq 0$

$$\int_S t_i * \tilde{u}_i dS + \int_V \rho \{b_i * \tilde{u}_i + v_{io} \tilde{u}_i + u_{io} \tilde{u}_{io}\} dV = \int_V \rho \{\tilde{b}_i * u_i + \tilde{v}_{io} u_i + \tilde{u}_{io} u_{io}\} dV$$

$$+ \int_S \dot{t}_i * u_i dS \quad (2.16)$$

The operation $*$ above denotes time convolution, i.e.,

$$f * g = \int_0^t f(\mathbf{x}, t - \tau) g(\mathbf{x}, \tau) d\tau = \int_0^t f(\mathbf{x}, \tau) g(\mathbf{x}, t - \tau) d\tau \quad (2.17)$$

for $t \geq 0$ and for two functions f and g .

2.2.3 Fundamental solutions

The fundamental solution at point \mathbf{x} (receiver) for displacement component i due to a unit impulse vector at point \mathbf{y} (source) at time τ in direction j for a three-dimensional elastic solid of infinite extent is solution of equation of motion with a body force

$$b_j = \delta(\mathbf{x} - \mathbf{y}) \delta(T - \tau) \mathbf{e}_j \quad (2.18)$$

where δ denotes the Dirac delta function and \mathbf{e}_j is a constant unit vector in direction j .

The fundamental solution for displacement at point \mathbf{x} and time T is given by

$$\begin{aligned} G_{ij}(\mathbf{x}, T; \mathbf{y}, \tau) = & \frac{1}{4\pi\rho} \left[(3a_{ij} - b_{ij}) \int_{1/c_1}^{1/c_2} \lambda \delta(v - \lambda r) d\lambda \right. \\ & + a_{ij} \left\{ (1/c_1^2) \delta(v - r/c_1) - (1/c_2^2) \delta(v - r/c_2) \right\} \\ & \left. + (b_{ij}/c_2^2) \delta(v - r/c_2) \right] \end{aligned} \quad (2.19)$$

where $v = T - \tau$; $a_{ij} = h_i h_j / r^3$; $b_{ij} = \delta_{ij} / r$; $h_i = x_i - y_i$ and r is the distance between points \mathbf{x} and \mathbf{y} . The fundamental solution for tractions is given by

$$\begin{aligned} H_{ij}(\mathbf{x}, T; \mathbf{y}, \tau) = & \frac{1}{4\pi} \left[-6c_2^2 (5a_{ij} - b_{ij}) \int_{1/c_1}^{1/c_2} \lambda \delta(v - \lambda r) d\lambda + (12a_{ij} - 2b_{ij}) \left\{ \delta(v - r/c_2) \right. \right. \\ & \left. \left. - (c_2/c_1)^2 \delta(v - r/c_1) \right\} + 2r a_{ij}/c_2 \left\{ \dot{\delta}(v - r/c_2) - (c_2/c_1)^3 \dot{\delta}(v - r/c_1) \right\} \right. \\ & \left. - c_{ij} (1 - 2c_2^2/c_1^2) \left\{ \delta(v - r/c_1) + (r/c_1) \dot{\delta}(v - r/c_1) \right\} \right. \\ & \left. - d_{ij} \left\{ \delta(v - r/c_2) + (r/c_2) \dot{\delta}(v - r/c_2) \right\} \right] \end{aligned} \quad (2.20)$$

where $v = T - \tau$; $h_i = x_i - y_i$; $a_{ij} = h_i h_j h_m n_m / r^5$; $c_{ij} = h_j n_i / r^3$; $d_{ij} = (h_i n_j + \delta_{ij} h_m n_m) / r^3$; $b_{ij} = c_{ij} + d_{ij}$. Also n_i are the components of outward pointing normal vector and $h_m n_m = h_1 n_1 + h_2 n_2 + h_3 n_3$.

The above fundamental solutions obey the causality condition

$$G_{ij}(\mathbf{x}, T, \mathbf{y}, \tau) = 0 \quad \text{if } c_1(T - \tau) < r \quad (2.21)$$

and have the following time translation property:

$$G_{ij}(\mathbf{x}, T + T_o, \mathbf{y}, \tau + T_o) = G_{ij}(\mathbf{x}, T, \mathbf{y}, \tau) \quad (2.22)$$

Love [55] concluded that Stoke's solution yields correct results only when the input quantities are continuous at the propagating wave front. In this case, both kinematic jump condition and momentum conditions are satisfied as well. This implies that if the input excitation is a step loading, it must be modelled as a ramp loading during the first time step. Also very small time steps should not be used because they result in non-vanishing dilatations and rotations at the wave front.

2.3 Boundary Integral representation

By utilising the dynamic reciprocal theorem with the untilded state being the real one and the tilded state being the fundamental singular solution, Love's [55] integral identity may be written in the form

$$\begin{aligned} C_{ij}(\mathbf{y})u_i(\mathbf{y}, T) &= \int_S [G_{ij} * t_i(\mathbf{x}, T) - H_{ij} * u_i(\mathbf{x}, T)] dS(\mathbf{x}) + \rho \int_V G_{ij} * b_i(\mathbf{x}, T) dV(\mathbf{x}) \\ &+ \rho \int_V [G_{ij} v_{io}(\mathbf{x}) + \dot{G}_{ij} u_{io}(\mathbf{x})] dV(\mathbf{x}) \end{aligned} \quad (2.23)$$

In the above, \mathbf{x} and \mathbf{y} are receiver and source points respectively, and u_{io} and v_{io} are the initial displacement and velocity, respectively. The free-term tensor components C_{ij} can be expressed as

$$C_{ij} = \delta_{ij} - \gamma_{ij} \quad (2.24)$$

where δ_{ij} is the Kronecker's delta and γ_{ij} is a discontinuity or jump term.

C -matrix depends on the local characteristic surface of the boundary point with respect to the domain. It depends on the solid angle of the boundary point. Mantic [56] has given a general closed analytical formula of the C -matrix for the case of any finite number of tangent planes to the boundary of the body at a non-smooth boundary point. For a smooth surface, value of C_{ij} is $.5\delta_{ij}$. An indirect method is also often used to calculate C -matrix as illustrated by Cruse [57]. C -matrix remains the same for both elastostatic and elastodynamic problems because it depends on the local geometry and Poisson's ratio of the material.

The above integral representations are exact statements of the problem that was originally cast in the form of partial differential equations. No approximation has been made,

and solutions of the integral representations satisfy the original differential equations as well.

In this work, elastodynamic problems, having zero initial conditions and zero body forces, have been considered. For zero initial conditions and zero body forces, the boundary integral formulation for transient elastodynamics reduces to

$$C_{ij}(\mathbf{y}) u_i(\mathbf{y}, T) = \int_S [G_{ij}(\mathbf{x}, \mathbf{y}, T) * t_i(\mathbf{x}, T) - H_{ij}(\mathbf{x}, \mathbf{y}, T) * u_i(\mathbf{x}, T)] dS(\mathbf{x}) \quad (2.25)$$

where

$$G_{ij} * t_i = \int_0^T G_{ij}(\mathbf{x}, T; \mathbf{y}, \tau) t_i(\mathbf{x}, \tau) d\tau \quad (2.26)$$

$$H_{ij} * u_i = \int_0^T H_{ij}(\mathbf{x}, T; \mathbf{y}, \tau) u_i(\mathbf{x}, \tau) d\tau \quad (2.27)$$

2.4 Numerical treatment of boundary integral equations

For zero initial conditions and zero body forces, the integral statement (2.25) expresses the unknown variable in terms of boundary variables. The solution of such an integral equation is not possible, in general, except if it is done numerically. The geometry of the problem and the field variables (displacements and tractions) must be discretized to solve non-trivial problems.

The time-domain BEM in three-dimensions consists of two basic steps as explained in [49, 58, 59]:

1. A discretization of the real time axis into a sequence of equally spaced time intervals with the assumption of linear variation of displacement and constant variation of tractions over each time interval. When piecewise linear variation is used for both displacements and tractions, the time-stepping scheme becomes unstable [60, 61]
2. A discretization of boundary into 8-noded elements.

On the basis of these discretizations a time stepping solution of equation (2.25) can be established for the boundary displacements and tractions over each element and for each time step.

2.4.1 Spatial discretization

The boundary is divided into a number of elements. The geometry, in the present work, has been described by continuous quadratic, eight-noded elements. Triangular elements are treated as collapsed quadrilateral elements. The cartesian coordinates of a point on the surface of a boundary element are given in terms of the element nodal coordinate $X_{i\alpha}$ as

$$x_i = M_\alpha(\eta_k) X_{i\alpha} \quad (2.28)$$

where $i = 1, 2, 3$; $k = 1, 2$; and $\alpha = 1, 2, \dots, 8$.

In the above, M_α are the shape functions defined in the intrinsic or local coordinate system η_k . The shape functions for the quadrilateral element are:

$$M_\alpha = \begin{cases} .25(1 + \xi_0)(1 + \eta_0)(\xi_0 + \eta_0 - 1) & \text{if } \alpha = 1, 3, 5, 7 \\ .5(1 + \xi^2)(1 - \eta_0) & \text{if } \alpha = 2, 6 \\ .5(1 + \xi_0)(1 - \eta^2) & \text{if } \alpha = 4, 8 \end{cases} \quad (2.29)$$

where $\xi_0 = \xi \cdot \xi_\alpha$ and $\eta_0 = \eta \cdot \eta_\alpha$ with ξ and η being the two independent coordinates and $(\xi_\alpha, \eta_\alpha)$ the coordinates of node α .

The transformation from the cartesian coordinate system to an element intrinsic coordinate system is through the Jacobian matrix given by

$$J_{ij} = \frac{\partial M_\alpha}{\partial \eta_j} X_{i\alpha} \quad (2.30)$$

2.4.2 Temporal and spatial interpolation of displacement and traction

The time span of interest is divided into N equal time steps of size ΔT so that

$$T_n = n \Delta T, \quad n = 1, 2, \dots, N. \quad (2.31)$$

The boundary variables are interpolated in terms of their values at nodes by

$$u_i(\mathbf{x}, \tau) = \sum_{n=1}^N [M_I^n u_i^{n-1}(\mathbf{x}) + M_F^n u_i^n(\mathbf{x})] \quad (2.32)$$

$$t_i(\mathbf{x}, \tau) = \sum_{n=1}^N [\mu_I^n t_i^{n-1}(\mathbf{x}) + \mu_F^n t_i^n(\mathbf{x})] \quad (2.33)$$

and

$$u_i^n(\mathbf{x}) = \sum_{c=1}^8 N^c[\xi(\mathbf{x})] u_i^{nc}, \quad i = 1, 2, 3 \quad (2.34)$$

$$u_i^{n-1}(\mathbf{x}) = \sum_{c=1}^8 N^c[\xi(\mathbf{x})] u_i^{(n-1)c}, \quad i = 1, 2, 3 \quad (2.35)$$

where u_i^{nc} and $u_i^{(n-1)c}$ represent nodal values of displacement at time nodes n and $(n-1)$ respectively. Similar interpolation is done for traction variables also. Here, N is the total number of time steps. M_I and M_F are the temporal interpolation functions, related to local time nodes I (initial) and F (final), and are of the following form for piecewise linear variation:

$$M_I^n = \frac{T_n - \tau}{\Delta T} \phi_n(\tau) \quad (2.36)$$

$$M_F^n = \frac{\tau - T_{n-1}}{\Delta T} \phi_n(\tau) \quad (2.37)$$

where

$$\phi_n(\tau) = \begin{cases} 1 & \text{if } (n-1)\Delta T \leq \tau \leq n\Delta T \\ 0 & \text{otherwise} \end{cases}$$

or

$$\phi_n(\tau) = H(\tau - (n-1)\Delta T) - H(\tau - n\Delta T) \quad (2.38)$$

H being the Heaviside function.

The displacements are interpolated by piecewise linear functions. Traction are represented by piecewise constant functions which allow for sudden jump of their values from step to step. It has been shown, in the case of BEM based on displacement integral equation, that this is the best interpolation scheme to linear order. [50,61] For tractions, temporal interpolation functions are of the form

$$\mu_I^n = 0.5 \phi_n(\tau) \quad (2.39)$$

$$\mu_F^n = 0.5 \phi_n(\tau) \quad (2.40)$$

For spatial interpolation of boundary variables, an approach [62] which combines the advantages of continuous and discontinuous elements in a single formulation is used in this paper. In this formulation, expressions of the shape and interpolation functions are unified in a form suitable for fully continuous, fully discontinuous or transition elements (i.e., discontinuous only along one or more edges). Three types of boundary nodes are identified depending on the function they fulfil:

1. Geometrical nodes: those used for interpolating the boundary geometry.
2. Interpolation nodes: the points on the boundary which define the interpolation of the variables. The system nodal values correspond to these nodes.
3. Collocation nodes: where the boundary integral equation is enforced.

These three kinds of nodes coincide at the same point in the commonest formulation of the boundary elements. One property of the boundary element formulations is that the discontinuities of the variable across the element edges do not invalidate the convergence of the technique [63]. Collocation and interpolation nodes for continuous elements coincide with the geometrical nodes. Collocation nodes and interpolation nodes for discontinuous elements and discontinuous side of transition elements are situated inside the element. For quarter-point element, geometrical and interpolation nodes coincide, but collocation corresponding to nodes on crack front is done at nodes situated inside the elements on either side of the crack front. To reduce the number of equations and enhance accuracy equations corresponding to collocation nodes before and after a given interpolation node are added up [64].

Interpolation functions

To determine these interpolation functions, it is necessary to define the position of the node points within the element, which can be done by defining a certain number of parameters based on the local coordinate system of the element. These parameters for the quadrilateral elements are as follows: Six parameters are needed to define the element nodal positions a_1, a_2, a_3, a_4, a_5 and a_6 , with $a_i = 1 - b_i$, ($i = 1, 2, 3, 4$), $a_5 = a_2 + a_4$, and $a_6 = a_1 + a_3$ (Fig 2.1). The values $b_1 = b_2 = b_3 = b_4 = 1/3$ are assumed for quadratic interpolation. The interpolation functions for eight-noded elements are as follows:

$$M(2) = (a_2 - \xi)(a_4 + \xi)(a_3 - \eta) / (a_2 a_4 a_6) \quad (2.41)$$

$$M(4) = (a_3 - \eta)(a_1 + \eta)(a_4 + \xi) / (a_1 a_3 a_5) \quad (2.42)$$

$$M(6) = (a_2 - \xi)(a_4 + \xi)(a_1 + \eta) / (a_2 a_4 a_6) \quad (2.43)$$

$$M(8) = (a_3 - \eta)(a_1 + \eta)(a_2 - \xi) / (a_1 a_3 a_5) \quad (2.44)$$

$$M(1) = (a_2 - \xi)(a_3 - \eta) / a_5 / a_6 - M(2)a_2 / a_5 - M(8)a_3 / a_6 \quad (2.45)$$

$$M(3) = (a_3 - \eta)(a_4 + \xi) / a_5 / a_6 - a_3 / a_6 M(4) - a_4 / a_5 M(2) \quad (2.46)$$

$$M(5) = (a_1 + \eta)(a_4 + \xi) / a_5 / a_6 - a_1 / a_6 M(4) - a_4 / a_5 M(6) \quad (2.47)$$

$$M(7) = (a_2 - \xi)(a_1 + \eta) / a_5 / a_6 - a_1 / a_6 M(8) - a_2 / a_5 M(6) \quad (2.48)$$

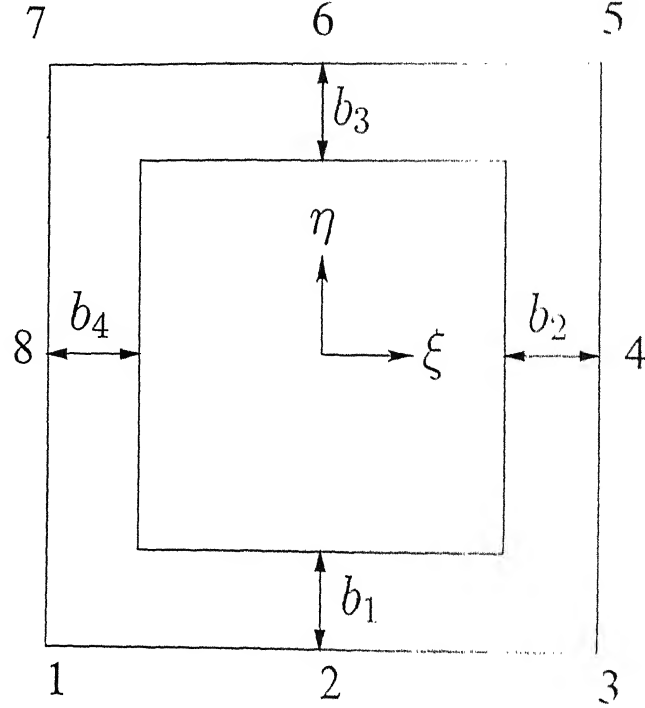


Figure 2.1: Quadrilateral element

2.4.3 Time-marching scheme

The displacement boundary integral equation can be written as

$$C_{ij}u_i(\mathbf{y}, T_N) - \int_{T_{N-1}}^{T_N} \int_S [G_{ij}t_i - H_{ij}u_i] dS d\tau = \int_0^{T_{N-1}} \int_S [G_{ij}t_i - H_{ij}u_i] dS d\tau \quad (2.49)$$

where the integral on the right hand side is the contribution due to past dynamic history. This equation is also an exact statement since no approximation has yet been introduced. However, in order to solve the above equation, one has to approximate the time variation of the field quantities, in addition to the usual approximation of spatial variation. The time integration in the above equation is done analytically, and the spatial integration is done numerically. A system of algebraic equations is obtained at time step N through nodal collocation, i.e., by allowing \mathbf{y} to coincide sequentially with all the nodal points of the boundary.

The boundary integral equation for the first time step is

$$C_{ij}u_i(\mathbf{y}, T_1) - \int_{T_0}^{T_1} \int_S [G_{ij}t_i - H_{ij}u_i] dS d\tau = 0 \quad (2.50)$$

After integrations, the resulting system of equations has the form

$$[G_F^1] \{t^1\} - [H_F^1] \{u^1\} + [G_I^1] \{t^0\} - [H_I^1] \{u^0\} = \{0\} \quad (2.51)$$

where $[G]$ and $[H]$ are coefficient matrices resulting from the surface integrations, $\{t\}$ and $\{u\}$ are the tractions and displacements at all nodal points, and superscripts denote the time steps. For $[G]$ and $[H]$ the superscript denotes the time step at which they are calculated, and the subscript denotes the local time node (I or F) during that time interval.

After the usual assembly process, the resulting system of equations has the form

$$[A_F^1] \{X^1\} - [B_F^1] \{Y^1\} + [A_I^1] \{X^0\} - [B_I^1] \{Y^0\} = \{0\} \quad (2.52)$$

where $[A]$ and $[B]$ are the matrices related to the unknown and known field quantities respectively. $\{X\}$ and $\{Y\}$ are vectors of unknown and known field quantities respectively.

Since all the unknowns at time $T = 0$ are assumed to be zero, equation reduces to

$$[A_F^1] \{X^1\} = [B_F^1] \{Y^1\} + [B_I^1] \{Y^0\} \quad (2.53)$$

Now, the boundary integral equation for the second time step is considered.

$$C_{ij}u_i(\mathbf{y}, T_2) - \int_{T_1}^{T_2} \int_S [G_{ij}t_i - H_{ij}u_i] dS d\tau = \int_0^{T_1} \int_S [G_{ij}t_i - H_{ij}u_i] dS d\tau \quad (2.54)$$

If the time difference $(T_2 - T_1)$ is the same as $(T_1 - T_0)$, the resulting coefficient matrices of the left hand sides of equations (2.50) and (2.54) become identical. This is due to the time translation property of fundamental solutions, G_{ij} and H_{ij} , which contain time functions with arguments $(T - \tau)$ and therefore, the convoluted integral corresponding to the interval $T_1 \leq \tau \leq T_2$ with $T = T_2$ is identical to that of the interval $T_0 \leq \tau \leq T_1$ with $T = T_1$.

The right hand side of equation (2.54) is evaluated at time $T = T_2$ with the time integration over the interval T_0 to T_1 and thus, provides the effect of the dynamic history of the first time interval on the current time node, i.e., T_2 .

Now, the resulting system of equations for the time node T_2 is of the form

$$\begin{aligned} [A_F^1] \{X^2\} - [B_F^1] \{Y^2\} + [G_I^1] \{t^1\} - [H_I^1] \{u^1\} &= -[G_F^2] \{t^1\} + [H_F^2] \{u^1\} \\ &\quad - [G_I^2] \{t^0\} + [H_I^2] \{u^0\} \end{aligned} \quad (2.55)$$

Equation can be rearranged such that

$$[A_F^1] \{X^2\} = [B_F^1] \{Y^2\} - [G_I^1 + G_F^2] \{t^1\} + [H_I^1 + H_F^2] \{u^1\} + [H_I^2] \{u^0\} - [G_I^2] \{t^0\} \quad (2.56)$$

In the above equation, all the quantities on the right hand side are known. Therefore, the unknown vector $\{X\}$ at time T_2 is obtained by solving the above system of equations.

Similarly, for the N^{th} time step, the boundary integral equation is written in a discretized form as given below:

$$[A_F^1] \{X^N\} - [B_F^1] \{Y^N\} = - \sum_{n=2}^N [[G_F^n + G_I^{n-1}] \{t^{N-n+1}\} - [H_F^n + H_I^{n-1}] \{u^{N-n+1}\}] + [H_I^n] \{u^0\} - [G_I^n] \{t^0\} \quad (2.57)$$

or

$$[A_F^1] \{X^N\} = [B_F^1] \{Y^N\} + \{R^N\} \quad (2.58)$$

where vector $\{R^N\}$ is the effect of the past dynamic history on the current time node. The above equations can be solved to find the unknown vector $\{X^N\}$ at time T_N .

2.4.4 Analytical temporal integration

For linear time interpolation, field variables are expressed as

$$f(\mathbf{x}, \tau) = \sum_{n=1}^N [M_I^n f^{n-1}(\mathbf{x}) + M_F^n f^n(\mathbf{x})] \quad (2.59)$$

where $f^n(\mathbf{x})$ represents the spatial variation of the field variable $f(\mathbf{x}, \tau)$ at time $T_n (= n\Delta T)$, and M_I^n and M_F^n are the temporal shape functions defined earlier.

The transient kernels, involved in boundary integral equations for elastodynamic problems, have one or more of the following time functions embedded in them:

$$\begin{aligned} \text{Time function (1)} : & \delta(T - \tau - r/c) \\ \text{Time function (2)} : & \int_{1/c_1}^{1/c_2} \lambda \delta(T - \tau - r/c) d\lambda \\ \text{Time function (3)} : & \dot{\delta}(T - \tau - r/c) \\ \text{Time function (4)} : & \ddot{\delta}(T - \tau - r/c) \\ \text{Time function (5)} : & \ddot{\dot{\delta}}(T - \tau - r/c) \end{aligned}$$

where ' c ' is either the pressure wave velocity c_1 or the shear wave velocity c_2 , and δ is the Dirac delta function.

Using equation (2.59), the time integrals related to any of the above listed functions can be expressed as

$$\begin{aligned} \int_0^T g(T - \tau - r/c) f(\mathbf{x}, \tau) d\tau &= \sum_{n=1}^N \int_{(n-1)\Delta T}^{n\Delta T} g(T - \tau - r/c) f(\mathbf{x}, \tau) d\tau \\ &= \sum_{n=1}^N \left[f^{n-1}(\mathbf{x}) \int_{(n-1)\Delta T}^{n\Delta T} M_I^n(\tau) g(T - \tau - r/c) d\tau \right. \\ &\quad \left. + \int_{(n-1)\Delta T}^{n\Delta T} M_F^n(\tau) f^n(\mathbf{x}) g(T - \tau - r/c) d\tau \right] \end{aligned}$$

$$+ f^n(\mathbf{x}) \int_{(n-1)\Delta T}^{n\Delta T} M_F^n(\tau) g(T - \tau - r/c) d\tau \Big] \quad (2.60)$$

An important characteristic of the transient dynamic kernels is the time translation property. Because of this property, at each time step, only the effect of the dynamic history of the first time step on the current time node needs to be evaluated, i.e., at each time step, the analytical time integration has to be done only for $n = 1$. Thus, equation (2.60) reduces to

$$\begin{aligned} \int_0^{\Delta T} g(T - \tau - r/c) f(\mathbf{x}, \tau) d\tau &= f^0(\mathbf{x}) \int_0^{\Delta T} \left(1 - \frac{\tau}{\Delta T}\right) \phi_1(\tau) g(T - \tau - r/c) f(\mathbf{x}, \tau) d\tau \\ &+ f^1(\mathbf{x}) \int_0^{\Delta T} \left(\frac{\tau}{\Delta T}\right) \phi_1(\tau) g(T - \tau - r/c) f(\mathbf{x}, \tau) d\tau \end{aligned} \quad (2.61)$$

The time integrals on the right hand side of above equation can be rearranged into the following two types of integrals:

- Type A: $\int_0^{\Delta T} \phi_1(\tau) g(T - \tau - r/c) d\tau$
- Type B: $\int_0^{\Delta T} \tau \phi_1(\tau) g(T - \tau - r/c) d\tau$

The convoluted time integrals of type ‘A’ and type ‘B’ with the time functions (1) and (2) are evaluated analytically as follows:

Time function 1

Type A

$$\int_0^{\Delta T} \phi_1(\tau) \delta(T - \tau - r/c) d\tau = \phi_1(T - r/c) = H(T - r/c) - H(T - \Delta T - r/c) \quad (2.62)$$

Type B

$$\int_0^{\Delta T} \tau \phi_1(\tau) \delta(T - \tau - r/c) d\tau = (T - r/c) \phi_1(T - r/c) \quad (2.63)$$

Time function 2

Type A

$$\int_0^{\Delta T} \int_{1/c_1}^{1/c_2} \lambda \delta(T - \tau - \lambda r) \phi_1(\tau) d\lambda d\tau = \int_{1/c_1}^{1/c_2} \lambda \phi(T - \lambda r) d\lambda$$

$$\begin{aligned}
&= \left[\frac{\lambda^2}{2} \phi_1 (T - \lambda r) \right]_{1/c_1}^{1/c_2} \\
&= \left[\frac{\lambda^2}{2} H (T - \lambda r) \right]_{1/c_1}^{1/c_2} \\
&= \left[\frac{\lambda^2}{2} H (T - \Delta T - \lambda r) \right]_{1/c_1}^{1/c_2} \quad (2.64)
\end{aligned}$$

where

$$\left[\frac{1}{2} \lambda^2 H (T - \lambda r) \right]_{1/c_1}^{1/c_2} = \begin{cases} 0 & \text{if } T < r/c_1 \\ \frac{T^2}{2r^2} - \frac{1}{2c_1^2} & \text{if } r/c_1 < T < r/c_2 \\ \frac{1}{2c_2^2} - \frac{1}{2c_1^2} & \text{if } T > r/c_2 \end{cases} \quad (2.65)$$

The second term on the right hand side of equation (2.64) can be obtained in a similar manner by replacing T by $T - \Delta T$ in equation (2.65).

Type B

$$\begin{aligned}
\int_0^{\Delta T} \int_{1/c_1}^{1/c_2} \lambda \delta (T - \tau - \lambda r) \tau \phi_1 (\tau) d\lambda d\tau &= \int_{1/c_1}^{1/c_2} \lambda (T - \lambda r) \phi_1 (T - \lambda r) d\lambda \\
&= \int_{1/c_1}^{1/c_2} T \lambda \phi_1 (T - \lambda r) d\lambda - \int_{1/c_1}^{1/c_2} r \lambda^2 \phi_1 (T - \lambda r) d\lambda \\
&= T \left[\frac{\lambda^2}{2} \phi_1 (T - \lambda r) \right]_{1/c_1}^{1/c_2} - r \left[\frac{\lambda^3}{3} \phi_1 (T - \lambda r) \right]_{1/c_1}^{1/c_2} \quad (2.66)
\end{aligned}$$

The terms on the right hand side of equation (2.66) are evaluated in a similar manner as that of equation (2.64).

Time function (3)

$$\int_{(n-1)\Delta T}^{n\Delta T} \ddot{\delta} (T - \tau - r/c) f (\mathbf{x}, \tau) d\tau = \frac{f^n (\mathbf{x}) - f^{n-1} (\mathbf{x})}{\Delta T} \phi_n (T - r/c) \quad (2.67)$$

Time function (4)

The temporal integration involving the time function (4), i.e., $\ddot{\delta} (T - \tau - r/c)$, is approximated by using a backward finite difference scheme as follows:

$$\int_{(n-1)\Delta T}^{n\Delta T} \ddot{\delta} (T - \tau - r/c) f (\mathbf{x}, \tau) d\tau = \frac{f^n (\mathbf{x}) - 2f^{n-1} (\mathbf{x}) + f^{n-2} (\mathbf{x})}{(\Delta T)^2} \phi_n (T - r/c) \quad (2.68)$$

Time function (5)

Similarly,

$$\int_{(n-1)\Delta T}^{n\Delta T} \ddot{\delta}(T - \tau - r/c) f(x, \tau) d\tau = \frac{f^n(x) - 3f^{n-1}(x) + 3f^{n-2}(x) - f^{n-3}(x)}{(\Delta T)^3} \phi_n(T - r) \quad (2.69)$$

If temporal integration results are closely examined, a particular radial variation is seen. All temporal terms can be expressed in the form $a + br + \frac{d}{r^2}$ after analytical integration with time as shown below: For the first time interval,

$$M_I^1(\tau) = \left(1 - \frac{\tau}{\Delta T}\right) \phi_1(\tau) \quad (2.70)$$

$$M_F^1(\tau) = \frac{\tau}{\Delta T} \phi_1(\tau) \quad (2.71)$$

Hence, for example,

$$\int_0^{\Delta T} \delta(T - \tau - r/c) M_I^1(\tau) d\tau = \begin{cases} \left(1 - \frac{T}{\Delta T}\right) + \frac{1}{c\Delta T}r & \text{if } c(T - \Delta T) < r < cT \\ 0 & \text{otherwise} \end{cases} \quad (2.72)$$

And

$$\int_0^{\Delta T} \delta(T - \tau - r/c) M_F^1(\tau) d\tau = \begin{cases} \frac{T}{\Delta T} - \left(\frac{1}{c\Delta T}\right)r & \text{if } c(T - \Delta T) < r < cT \\ 0 & \text{otherwise} \end{cases} \quad (2.73)$$

Similarly,

$$\int_0^{\Delta T} \int_{1/c_1}^{1/c_2} M_I^1(\tau) \delta(t - \lambda r) \lambda d\lambda = A - \frac{B}{\Delta T} \quad (2.74)$$

where

$$\begin{aligned} A &= \frac{1}{2}\lambda^2 H(T - \lambda r) - \frac{1}{2}\lambda^2 H(T - \Delta T - \lambda r) \\ &= D - E \end{aligned} \quad (2.75)$$

And

$$D = \begin{cases} 0 & \text{if } r > c_1 T \\ \frac{1}{2} \left(\frac{1}{c_2^2} - \frac{1}{c_1^2} \right) & \text{if } r < c_2 T \\ -\frac{1}{2} \frac{1}{c_2^2} + \frac{1}{2} \frac{T^2}{r^2} & \text{if } c_2 T < r < c_1 T. \end{cases} \quad (2.76)$$

$$E = \begin{cases} 0 & \text{if } r > c_1 (T - \Delta T) \\ \frac{1}{2} \left(\frac{1}{c_2^2} - \frac{1}{c_1^2} \right) & \text{if } r < c_2 (T - \Delta T) \\ -\frac{1}{2} \frac{1}{c_2^2} + \frac{1}{2} \frac{(T - \Delta T)^2}{r^2} & \text{if } c_2 (T - \Delta T) < r < c_1 (T - \Delta T) \end{cases} \quad (2.77)$$

Similarly, (2.78)

$$B = F - G \quad (2.79)$$

where (2.80)

$$F = \begin{cases} 0 & \text{if } r > c_1 T \\ \frac{T}{2} \left(\frac{1}{c_2^2} - \frac{1}{c_1^2} \right) - \frac{1}{3} \left(\frac{1}{c_2^3} - \frac{1}{c_1^3} \right) r & \text{if } r < c_2 T \\ \frac{1}{2} \frac{T}{c_1^2} + \frac{R}{3} \frac{1}{c_1^3} + \frac{T^3}{6r^2} & \text{if } c_2 T < r < c_1 T \end{cases} \quad (2.81)$$

And (2.82)

$$G = \begin{cases} 0 & \text{if } r > c_1 (T - \Delta T) \\ \frac{T}{2} \left(\frac{1}{c_2^2} - \frac{1}{c_1^2} \right) - \frac{1}{3} \left(\frac{1}{c_2^3} - \frac{1}{c_1^3} \right) r & \text{if } r < c_2 (T - \Delta T) \\ \frac{1}{2} \frac{T}{c_1^2} + \frac{R}{3} \frac{1}{c_1^3} + \frac{(T - \Delta T)^2}{6r^2} (T + 2\Delta T) & \text{if } c_2 (T - \Delta T) < r < c_1 (T - \Delta T) \end{cases} \quad (2.83)$$

Similarly,

$$\int_0^{\Delta T} \int_{1/c_1}^{1/c_2} M_{P'}^1(\tau) \lambda \delta(t - \lambda r) d\lambda = \frac{B}{\Delta T}, \quad (2.84)$$

where B is defined in equation(2.79).

Thus, all temporal terms can be expressed in the form $a + br + \frac{d}{r^2}$ after analytical integration with time. Also it is noticed that for the distance reached by both shear and compression waves travelling from a source node up to a time ΔT , coefficient of $\frac{1}{r^2}$ is zero.

2.5 Spatial integration

In this section, details are given about a new partitioning scheme that is proposed in this thesis for spatial integration of elastodynamic kernels. A typical surface element is shown in figure 2.2. At first the element is quiescent since no signals from the source point \mathbf{y} have yet arrived. Spatial integration of the displacement and traction kernels takes place during the time interval t_m denoting the arrival of the pressure signal. The area over which the integration takes place is the band between radii $c_1 t_m$ and $c_2(t_m - 1)$. After passage of the shear wave, the element is quiet again and there is nothing to integrate in view of the causality condition. The area covered by a wave in a time step, starting from a particular source node, does not contribute to the integrals in the later time steps.

The kernels in elastodynamic case have discontinuous derivatives at points such that $r/c_{1(2)} = k\Delta t$ (k integer). Therefore, the standard numerical methods, like Gaussian integration, give poor results if applied over the whole element, say, E_i . Instead one has to partition each element E_i into sub-elements $E_i^k : E_i = \cup E_i^k$ with $E_i^k = \{(k-1)\Delta t < r/c < k\Delta t\}$. Then, an integral over E_i is the sum of sub-integrals over E_i^k , each sub-integral being

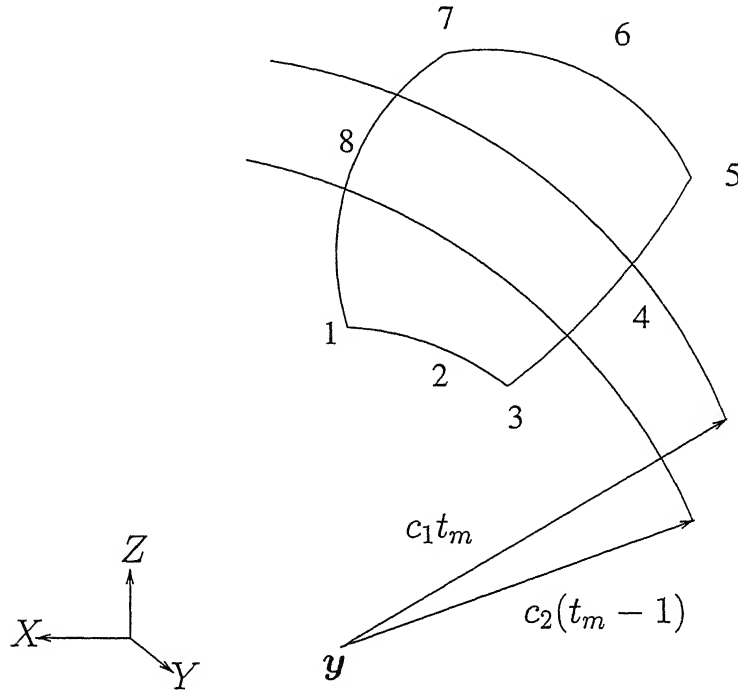


Figure 2.2: Surface element enveloped by P- and S-waves emanating from y at time t_m .

evaluated using standard numerical methods. The partitioning is reasonably tractable for 2-D problems. It is clearly a purely geometrical problem (find the intersection points of a given curve C with circles centered at a given point y and of equally spaced radii). On the contrary, its three-dimensional equivalent (find the intersection curves of a given surface S with spheres centered at a given point y and of equally spaced radii) is extremely complicated. However, Karabalis [59] had performed the spatial integrations by partitioning the receiver elements into very small rectangular sub-elements. With this, the possibility of only certain portions of the source element being ‘active’ also could be taken into consideration.

In this thesis, a new scheme is proposed for partitioning of surface elements for 3-D problems as follows:

2.5.1 Partitioning scheme

Consider a boundary element S_p . It is mapped onto a square region R (Fig. 4.1) in the parameter plane having local intrinsic coordinates $\xi = (\xi_1, \xi_2)$. Suppose source point is y and a typical receiver point is x . Hence, a typical integral over the surface S_p can be

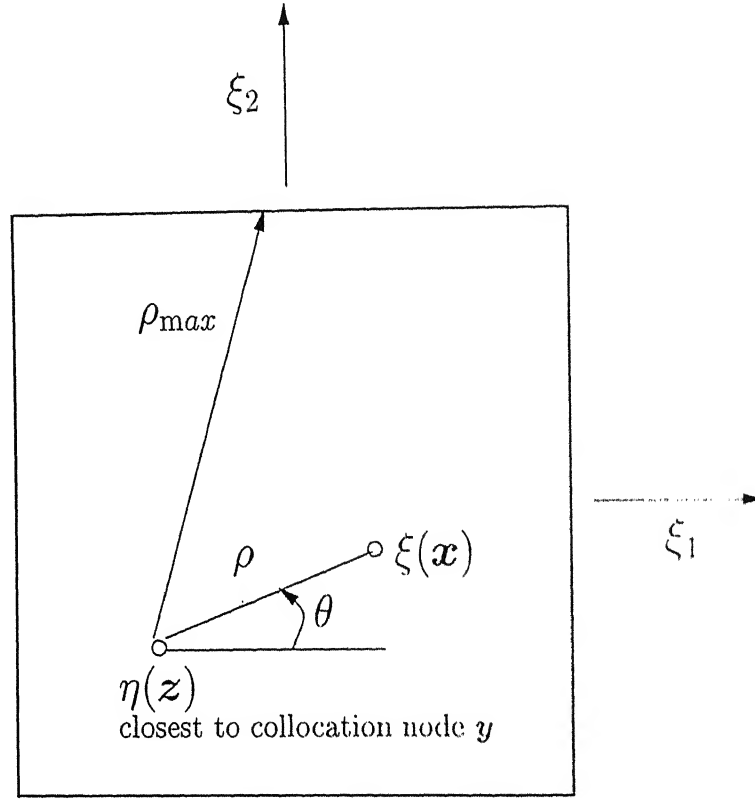


Figure 2.3: Image in the parameter plane and polar coordinates

written as

$$\begin{aligned}
 I &= \int_{S_p} \int_0^T \left[V_{ij}(\mathbf{x}(\xi), T; \mathbf{y}, \tau) N^c(\xi, \mathbf{x}) M(\tau) d\tau \right] dS(\mathbf{x}) \\
 &= \int_{S_p} \left[\int_0^T V_{ij}(\mathbf{x}(\xi), T; \mathbf{y}, \tau) M(\tau) d\tau \right] N^c(\xi, \mathbf{x}) dS(\mathbf{x}) \\
 &= \int_R \int_0^T [V_{ij}(\mathbf{x}(\xi), T; \mathbf{y}, \tau) M(\tau) d\tau] N^c(\xi) J(\xi) d\xi_1 d\xi_2 \quad (2.85)
 \end{aligned}$$

where V_{ij} is displacement or traction kernel, $M(\tau)$ is temporal interpolation function, and $N^c(\xi, \mathbf{x})$ are spatial interpolation functions of field variables.

Coordinates of a receiver point on a boundary element are given by a parametric representation in terms of shape function $M^c(\xi_1, \xi_2)$ and nodal coordinates x_i^c .

$$x_i = \sum_c M^c(\xi_1, \xi_2) x_i^c, \quad i = 1, 2, 3 \quad (2.86)$$

Let us indicate by $\eta = (\eta_1, \eta_2)$, the image of the point z on the element. Point z is closest

to the source point. The first, second and third order derivatives are obtained by

$$\frac{\partial x_i}{\partial \xi_k} = \frac{\partial M^c}{\partial \xi_k} x_i^c \quad (2.87)$$

$$\frac{\partial^2 x_i}{\partial \xi_k^2} = \frac{\partial^2 M^c}{\partial \xi_k^2} x_i^c \quad (2.88)$$

$$\frac{\partial^3 x_i}{\partial \xi_k^3} = \frac{\partial^3 M^c}{\partial \xi_k^3} x_i^c \quad (2.89)$$

By employing a Taylor expansion about the closest point, it is easy to establish formula of the form

$$\begin{aligned} x_i = & z_i + \left[\frac{\partial x_i}{\partial \xi_1} \Big|_{\xi=\eta} (\xi_1 - \eta_1) + \frac{\partial x_i}{\partial \xi_2} \Big|_{\xi=\eta} (\xi_2 - \eta_2) \right] \\ & + \left[\frac{\partial^2 x_i}{\partial \xi_1^2} \Big|_{\xi=\eta} \frac{(\xi_1 - \eta_1)^2}{2} + \frac{\partial^2 x_i}{\partial \xi_1 \partial \xi_2} \Big|_{\xi=\eta} (\xi_1 - \eta_1)(\xi_2 - \eta_2) + \frac{\partial^2 x_i}{\partial \xi_2^2} \Big|_{\xi=\eta} \frac{(\xi_2 - \eta_2)^2}{2} \right] \\ & + \left[\frac{1}{2} (\xi_1 - \eta_1)^2 (\xi_2 - \eta_2) \frac{\partial^3 x_i}{\partial \xi_1^2 \partial \xi_2} \Big|_{\xi=\eta} + \frac{1}{2} (\xi_1 - \eta_1)(\xi_2 - \eta_2)^2 \frac{\partial^3 x_i}{\partial \xi_1 \partial \xi_2^2} \Big|_{\xi=\eta} \right] \end{aligned} \quad (2.90)$$

Since geometry is interpolated with help of quadratic functions, above formula is exact. The terms $\frac{\partial^3 x_i}{\partial \xi_1^3}$ and $\frac{\partial^3 x_i}{\partial \xi_2^3}$ do not appear in the above expression as these are equal to zero due to quadratic interpolation of geometry.

Following a common practice in the BEM, polar coordinates (ρ, θ) centered at η are defined in the parameter plane as

$$\xi_1 = \eta_1 + \rho \cos \theta \quad (2.91)$$

$$\xi_2 = \eta_2 + \rho \sin \theta \quad (2.92)$$

so that $d\xi_1 d\xi_2 = \rho d\rho d\theta$. Hence,

$$\begin{aligned} x_i - y_i = & e_i + \rho \left[\frac{\partial x_i}{\partial \xi_1} \cos \theta + \frac{\partial x_i}{\partial \xi_2} \sin \theta \right] \\ & + \rho^2 \left[\frac{\partial^2 x_i}{\partial \xi_1^2} \frac{\cos^2 \theta}{2} + \frac{\partial^2 x_i}{\partial \xi_1 \partial \xi_2} \cos \theta \sin \theta + \frac{\partial^2 x_i}{\partial \xi_2^2} \frac{\sin^2 \theta}{2} \right] \\ & + \rho^3 \left[\frac{1}{2} \cos^2 \theta \sin \theta \frac{\partial^3 x_i}{\partial \xi_1^2 \partial \xi_2} + \frac{1}{2} \cos \theta \sin^2 \theta \frac{\partial^3 x_i}{\partial \xi_1 \partial \xi_2^2} \right] \\ = & e_i + \rho A_i(\theta) + \rho^2 B_i(\theta) + \rho^3 C_i(\theta) \end{aligned} \quad (2.93)$$

where $e_i = z_i - y_i$. Hence,

$$\begin{aligned} r^2 &= \Sigma(x_i - y_i)^2 \\ &= \Sigma e_i^2 + 2\rho \Sigma(A_i(\theta)e_i) + \rho^2(\Sigma A_i^2(\theta) + 2\Sigma(e_i B_i(\theta))) + 2\rho^3(\Sigma A_i(\theta)B_i(\theta) + \Sigma(e_i C_i(\theta))) \\ &\quad + \rho^4(2\Sigma(A_i(\theta)C_i(\theta)) + \Sigma B_i^2(\theta)) + 2\rho^5\Sigma(B_i(\theta)C_i(\theta)) + \rho^6\Sigma C_i^2(\theta) \end{aligned} \quad (2.94)$$

For integration, the integration square ($-1 \leq \xi_i \leq 1$) is subdivided into triangles with common vertex at $\eta = (\eta_1, \eta_2)$. The integral (2.85) of a typical kernel over each triangle is performed as

$$I = \int_{\theta_1}^{\theta_2} \int_0^{\rho_{\max}} F_{ij}(\rho, \theta) d\rho d\theta \quad (2.95)$$

where

$$F_{ij}(\rho, \theta) = W_{ij}(\mathbf{y}, \mathbf{x}(\xi(\rho, \theta))) N^c(\xi(\rho, \theta)) \rho J(\xi(\rho, \theta)) \quad (2.96)$$

where $W_{ij} = \int_0^T V_{ij}(\mathbf{x}, T; \mathbf{y}, \tau) M(\tau) d\tau$. The limits θ_1 and θ_2 are angles subtended by the arms of the triangle on the vertex $\eta = (\eta_1, \eta_2)$. Here ρ_{\max} is the value of ρ on a particular ray making angle θ , where it meets the opposite side of the triangle.

First of all, Gauss integration is performed over θ direction. Corresponding to the value of θ computed as per Gauss points, ρ_{\max} is calculated for the particular ray. The values of ρ on a particular ray corresponding to the distance of $c_1 n \Delta t$ or $c_2 n \Delta t$ are computed by a combination of bisection and Newton-Raphson methods applied on equation (2.94). For each ray, the value of ρ are found corresponding to positions of heads and tails of the wavefronts of compression and shear waves, starting from the source node, for the element and time interval under consideration. The ray is divided into three different zones for separate Gaussian integration. The three different zones are:

1. both compression and shear wave cover part of the ray.
2. only compression wave covers part of the ray.
3. only shear wave travels that portion of the ray in that particular time interval.

In a time interval, only those areas contribute to the integral which were not affected by the particular waves in previous time intervals. Thus, jump in the kernel at points such that $r = c_{1(2)} n \Delta t$ is handled accurately.

Non-singular and singular integrals

Analytical integration of the matrix coefficients in equations is not, in general, possible and therefore, numerical quadrature must be used. Thus, fundamental solution-shape function products are approximated by application of the Gauss-Legendre quadrature formula. [65]

$$\int_{-1}^1 f(\eta) d\eta = \sum_{k=1}^K f(\eta^k) w^k \quad (2.97)$$

in which η^k and w^k are Gaussian points and weights, respectively. Application of the above one-dimensional formula along two orthogonal directions allows integration over quadrilaterals.

One can distinguish two basic cases of integrand behaviour, non-singular and singular. In the former case, the distance r between source-point \mathbf{y} and receiver (or integration) point \mathbf{x} on the surface of the element is never zero. In the latter case, \mathbf{y} coincides with one of the receiver points and r becomes zero.

2.6 Evaluation of Principal-Value Integral

Principal value singularity occurs for traction kernel H_{ij} when source element becomes also a receiver. All temporal terms can be expressed in the form $a + br + \frac{d}{r^2}$ after analytical integration in time, as explained in section 2.4.4 on temporal integration. Also a, b, d are constant in the respective zones as explained in section 2.5.1 allowing use of techniques developed for integrating elastostatic kernels by splitting the radial integration over three separate zones.

It is well known that integral involving the traction kernel is strongly singular only in the first time step. It is noticed that for the distance reached by both shear and compression waves travelling from a source node up to a time T , coefficient of $\frac{1}{r^2}$ is zero. Thus, the temporal terms are not contributing to the singularity in r . In the later time steps, the integral is regular as the region, close to the source node and traversed by both the waves up to the previous time-step, does not contribute to the integral. The Cauchy principal value integral is treated in the same way, as done by Guiggiani and Gigante [7] for the elastostatic case. The non-linear transformation suggested by Doblaré and Gracia [66] is also incorporated.

Elastodynamic displacement boundary integral equation for a three-dimensional do-

main Ω , bounded by the regular surface [54], can be expressed as

$$\lim_{\epsilon \rightarrow 0^+} \int_{(S-e_\epsilon)+S_\epsilon} [G_{ij}(\mathbf{x}, T; \mathbf{y}, \tau) * t_i(\mathbf{x}, T) - H_{ij}(\mathbf{x}, T; \mathbf{y}, \tau) * u_i(\mathbf{x}, T)] dS(\mathbf{x}) = 0 \quad (2.98)$$

If $r = |\mathbf{x} - \mathbf{y}|$ represents the distance between the source point \mathbf{y} and receiver point \mathbf{x} , the kernel G_{ij} shows a weak singularity when $\mathbf{x} \rightarrow \mathbf{y}$, while the kernel H_{ij} shows a strong singularity of the order of $O(1/r^2)$ in three-dimensional problems.

Since in equation (2.98) both the source point \mathbf{y} and the integration point \mathbf{x} lie on the surface S , a limiting process is necessary. Since equation (2.98) stems from Green's second identity, it may only be formulated on a domain not including the singular point \mathbf{y} . The situation is shown in Fig. 2.4, where a (vanishing) neighbourhood v_ϵ of \mathbf{y} has been

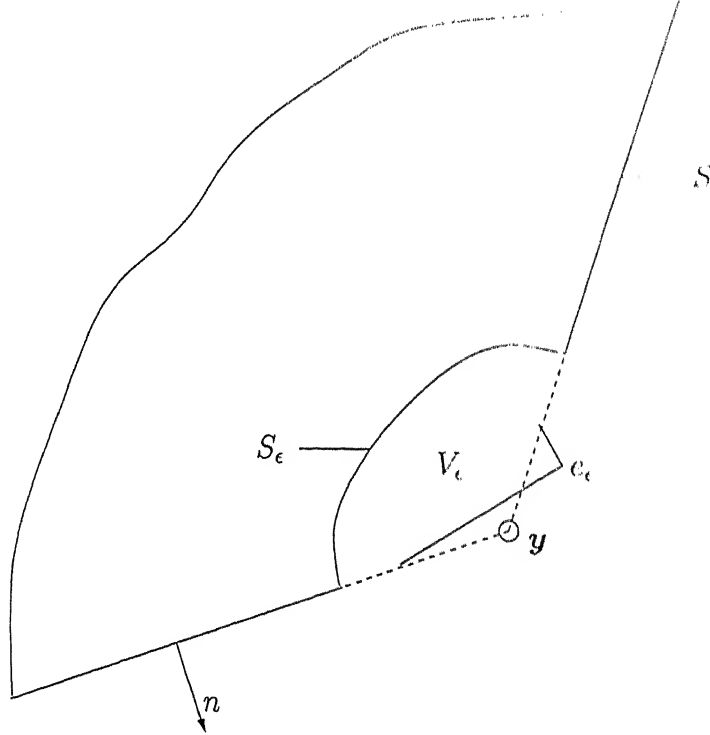


Figure 2.4: General vanishing neighbourhood around the source point

removed from the original domain Ω . The integration is thus performed on the boundary $S_\epsilon = (S - e_\epsilon) + s_\epsilon$ of the new domain $\Omega_\epsilon = \Omega - v_\epsilon$. The integration must be done before taking the limit. Since equation already states that the value of overall limit is zero, all divergent parts get cancelled [7, 67].

It is also not necessary to restrict the shape of v_ϵ . It may have any shape, provided \mathbf{y} is an exterior point for Ω_ϵ , and S_ϵ is a regular surface in the sense of Kellogg [54].

However, once the shape of the vanishing neighbourhood v_ϵ has been selected, both e_ϵ and s_ϵ are uniquely determined, and their shapes must be preserved while $\epsilon \rightarrow 0^+$, i.e. the maximum chord of v_ϵ approaches zero. More importantly, the shape of e_ϵ must be consistent with the shape of s_ϵ throughout the process.

The most convenient shape for s_ϵ , that is a sphere centered at \mathbf{y} and of radius ϵ , is selected. The selected shape of s_ϵ also enforces the shape of e_ϵ , which becomes a symmetric neighbourhood on S around the singular point \mathbf{y} . Although the value of limit taken as whole in equation is completely independent of the selected shape of v_ϵ , the value of each term in equation(2.98), taken separately does actually depend on the shape of either e_ϵ or s_ϵ .

Since s_ϵ is a sphere, the limits of all integrals on s_ϵ in equation(2.98) can be evaluated explicitly. Letting $\epsilon \rightarrow 0$, the following boundary integral equation arises

$$C_{ij}(\mathbf{y}) u_i(\mathbf{y}, T) = \int_{S-e_\epsilon} [G_{ij}(\mathbf{x}, T; \mathbf{y}, \tau) * t_i(\mathbf{x}, T) - H_{ij}(\mathbf{x}, T; \mathbf{y}, \tau) * u_i(\mathbf{x}, T)] dS(\mathbf{x}) \quad (2.99)$$

where the so-called free-term coefficients C_{ij} are given by the limit of the traction integral on the surface s_ϵ of v_ϵ , while displacement kernel gives a zero value over s_ϵ . Due to the chosen shape of v_ϵ (a sphere for three-dimensional modelling) which enforces the symmetry with respect to \mathbf{y} of the vanishing neighbourhood e_ϵ on S , the surface integral on left-hand side of equation(2.99) can be defined in the sense of a Cauchy principal value.

The set of all adjacent elements connected to the singular collocation point \mathbf{y} is defined as S_p . Those elements belonging to S_p are indicated by S_p^m ($S_p = \cup_m S_p^m$). The boundary element S_p^m is mapped onto a region R^m of standard shape in the parametric plane(i.e., a square).

Now, the geometry of an element is described in terms of shape functions and nodal coordinates:

$$x_k(\xi) = \sum_c M^c(\xi) X_k^c, \quad k = 1, 2, 3 \quad (2.100)$$

Displacement and traction are described by shape functions $N^c(\xi_1, \xi_2)$ of local intrinsic coordinates $\xi = (\xi_1, \xi_2)$, so that

$$u_i(\mathbf{x}, \tau) = \sum_{n=1}^N [M_I^n u_i^{n-1}(\mathbf{x}) + M_F^n u_i^n(\mathbf{x})] \quad (2.101)$$

and

$$u_i^n(\mathbf{x}) = \sum_c N^c[\xi(\mathbf{x})] u_i^{nc}, \quad i = 1, 2, 3 \quad (2.102)$$

$$u_i^{n-1}(\mathbf{x}) = \sum_c N^c[\xi(\mathbf{x})] u_i^{(n-1)c}, \quad i = 1, 2, 3 \quad (2.103)$$

where u_i^{nc} and $u_i^{(n-1)c}$ represent nodal values of displacement at time node n and $(n-1)$ respectively.

Similar interpolation is done for traction variables also. After discretization of geometry and interpolation of boundary variables, discretized version of equation(2.99) is obtained.

$$\begin{aligned} & u_j^{pa,n}(T) [N^a(\xi(\mathbf{y})) C_{ij}(\mathbf{y}) + \int_{S_p} \int_0^T H_{ij}(\mathbf{x}, T; \mathbf{y}, \tau) N^a(\xi(\mathbf{x})) M_F^n(\tau) d\tau dS(\mathbf{x})] \\ & + u_j^{pa,n-1}(T) \int_{S_p} \int_0^T H_{ij}(\mathbf{x}, T; \mathbf{y}, \tau) N^a(\xi(\mathbf{x})) M_F^n(\tau) d\tau dS(\mathbf{x}) \\ & - \sum_b \sum_{c \text{ } (b,c) \neq (p,a)} u_j^{bc,n-1} \int_{R_b} \int_0^T [H_{ij}(\mathbf{x}, T; \mathbf{y}(\xi), \tau) N^c(\xi) M_F^n(\tau) d\tau] J^b(\xi) d\xi \\ & - \sum_b \sum_{c \text{ } (b,c) \neq (p,a)} u_j^{bc,n} \int_{R_b} \int_0^T [H_{ij}(\mathbf{x}, T; \mathbf{y}(\xi), \tau) N^c(\xi) M_F^n(\tau) d\tau] J^b(\xi) d\xi \\ & + \sum_b \sum_c t_j^{bc,n-1} \int_{R_b} \int_0^T [G_{ij}(\mathbf{x}, T; \mathbf{y}(\xi), \tau) N^c(\xi) M_F^n(\tau) d\tau] J^b(\xi) d\xi \\ & + \sum_b \sum_c t_j^{bc,n} \int_{R_b} \int_0^T [G_{ij}(\mathbf{x}, T; \mathbf{y}(\xi), \tau) N^c(\xi) M_F^n(\tau) d\tau] J^b(\xi) d\xi \end{aligned} \quad (2.104)$$

It is important to remember that, notwithstanding the introduction of the one-to-one mapping between the boundary points and the intrinsic coordinates ξ , the symmetry of the vanishing neighbourhood hidden in any CPV definition must be maintained.

In equation (2.104), S_p indicates the set of all adjacent elements connected to the singular (collocation) point \mathbf{y} , and N^a collects all shape functions that do not vanish as $\mathbf{x} \rightarrow \mathbf{y}$ (usually $N^a(\xi(\mathbf{y})) = 1$). S_b indicates the set of all elements on S excluding S_p . R_b is the image of the boundary element S_b in the parameter space ξ (i.e., $[-1, 1] \times [-1, 1]$ square). In the next section, attention is focussed on CPV integral on S_p .

Strongly singular integral on surface element

Here attention is restricted to S_p . Those elements belonging to S_p are indicated by S_p^m ($S_p = \cup_m S_p^m$). The strongly singular integral over the surface S_p is

$$\int_{S_p} \int_0^T [H_{ij}(\mathbf{x}(\xi), T; \mathbf{y}, \tau) N^a(\xi(\mathbf{x})) M(\tau) d\tau] dS(\mathbf{x})$$

$$\begin{aligned}
&= \lim_{\epsilon \rightarrow 0} \int_{S_p - e_\epsilon} \left[\int_0^T H_{ij}(\mathbf{x}, T; \mathbf{y}, \tau) M(\tau) d\tau \right] N^a(\xi(\mathbf{x})) dS(\mathbf{x}) \\
&= \lim_{\epsilon \rightarrow 0} \sum_m \int_{S_p^m - e_\epsilon^m} \left[\int_0^T H_{ij}(\mathbf{x}, T; \mathbf{y}, \tau) M(\tau) d\tau \right] N^a(\xi(\mathbf{x})) dS(\mathbf{x}) \\
&= \lim_{\epsilon \rightarrow 0} \sum_m \int_{R^m - \sigma_\epsilon^m} \int_0^T [H_{ij}(\mathbf{x}(\xi), T; \mathbf{y}, \tau) M(\tau) d\tau] N^a(\xi) J^m(\xi) d\xi \quad (2.105)
\end{aligned}$$

where e_ϵ^m represents the part of e_ϵ lying on S_p^m . The plane region R^m (of standard shape) is the image of the surface element S_p^m in the transformed plane (ξ_1, ξ_2) and accordingly, σ_ϵ^m is the image of e_ϵ^m (Figure (2.5)). It can be noticed, in general, that σ_ϵ^m does not have a circular shape (although its polar radius still tends to zero with ϵ). In equation (2.105), all elements S_p^m around the pole \mathbf{y} must be taken together, as any single contribution is unbounded in the limit. Now, elastodynamic kernels contain time varying functions. All temporal terms can be expressed in the form $a + br + \frac{d}{r^2}$ after analytical integration with time as already explained. Also a, b, d are constant in the respective zones as explained in section 2.5.1, allowing use of techniques developed for integrating elastostatic kernels by splitting the radial integration over three separate zones.

It is well known that integral involving the traction kernel is strongly singular only in the first time step. It is noticed that for the distance reached by both shear and compression waves travelling from a source node up to a time ΔT , coefficient of $\frac{1}{r^2}$ is zero. In the later time steps, the integral is regular as the region, close to the source node and traversed by both the waves up to the previous time-step, does not contribute to the integral.

Thus, Cauchy principal value integral for elastodynamic case can be treated in the same way, as done by Guiggiani et al [7] for the elastostatic case. Next section shows the transformation of the original CPV integral into an element-by-element sum of regular integrals, each one expressed in terms of intrinsic coordinates.

Principal-value calculation

A representative term of strong singularity present in the traction kernel can be represented as $\frac{1}{r^2}$. This section shows how the singularity is subtracted out and integrand is regularised.

A polar coordinate system (ρ, θ) centered at η , image of the singular point \mathbf{y} , is introduced in each R^m .

Define

$$\xi_1 = \eta_1 + \rho \cos \theta \quad (2.106)$$

$$\xi_2 = \eta_2 + \rho \sin \theta \quad (2.107)$$

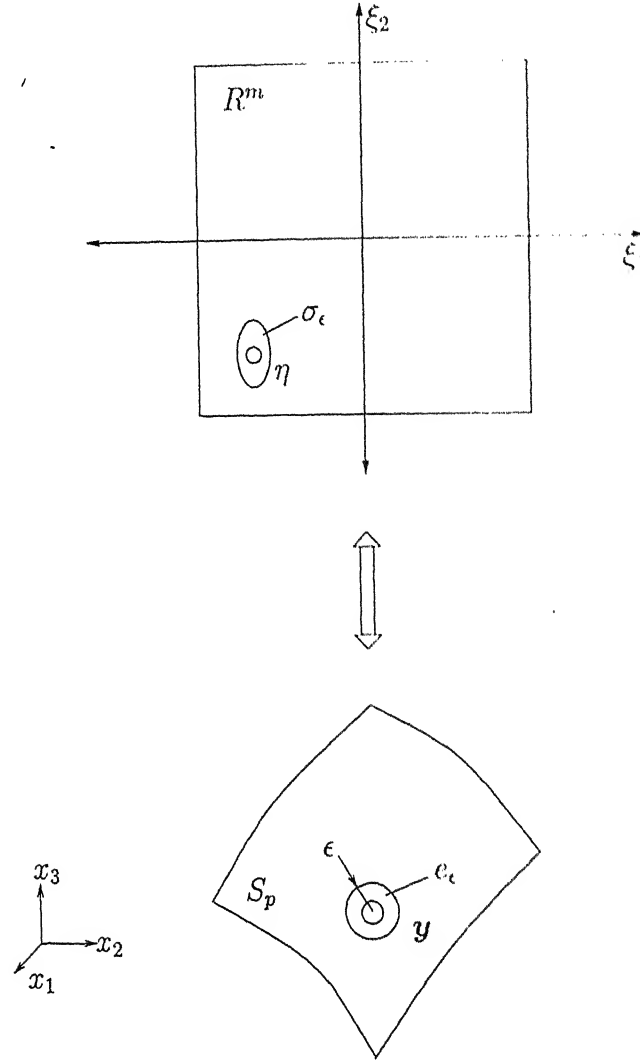


Figure 2.5: Image in the parameter plane of the boundary element and of the vanishing neighbourhood

thus, having

$$d\xi_1 d\xi_2 = \rho d\rho d\theta \quad (2.108)$$

The integration on element S_p^m is now considered separately, provided the limit process has not been performed yet (its value would be unbounded).

$$\int_{R^m - \sigma_\epsilon^m} H_{ij}(\mathbf{y}, \mathbf{x}(\xi)) N^a(\xi) J^m(\xi) d\xi = \int_{\theta_1^m}^{\theta_2^m} \int_{\alpha^m(\epsilon, \theta)}^{\rho^m(\theta)} F_{ij}^m(\rho, \theta) d\rho d\theta \quad (2.109)$$

where

$$F_{ij}^m(\rho, \theta) = H_{ij}(\mathbf{y}, \mathbf{x}(\xi(\rho, \theta))) N^a(\xi(\rho, \theta)) \rho J^m(\xi) \quad (2.110)$$

By employing a Taylor expansion in the neighbourhood of the singular point [68], it can be shown

$$\begin{aligned} x_i - y_i &= \frac{\partial x_i}{\partial \xi_1} (\xi_1 - \eta_1) + \frac{\partial x_i}{\partial \xi_2} (\xi_2 - \eta_2) + O(\rho^2) \\ &= \rho \left(\frac{\partial x_i}{\partial \xi_1} \cos \theta + \frac{\partial x_i}{\partial \xi_2} \sin \theta \right) + O(\rho^2) \\ &= \rho A_i(\theta) \end{aligned} \quad (2.111)$$

where

$$A_i(\theta) = \left(\frac{\partial x_i}{\partial \xi_1} \cos \theta + \frac{\partial x_i}{\partial \xi_2} \sin \theta \right), \quad i = 1, 2, 3 \quad (2.112)$$

and

$$A(\theta) = \left\{ \sum_{i=1}^3 [A_i(\theta)]^2 \right\}^{1/2} \quad (2.113)$$

Also,

$$r^2(\rho, \theta) = \rho^2 A^2(\theta) + O(\rho^3) \quad (2.114)$$

$$\frac{1}{r^2} = \frac{1}{\rho^2 A^2(\theta)} + O\left(\frac{1}{\rho}\right) \quad (2.115)$$

$$r_{,i} = \frac{x_i - y_i}{r} = \frac{A_i(\theta)}{A(\theta)} + O(\rho) \quad (2.116)$$

$$J_k = n_k J = J_k(\eta) + O(\rho) \quad (2.117)$$

$$r_{,k} J_k = O(\rho) \quad (2.118)$$

$$N^a = N^a(\eta) + O(\rho) \quad (2.119)$$

Now, it is possible to give explicitly the asymptotic expression of the singular integrand function F_{ij} (2.110) as

$$F_{ij}(\rho, \theta) = \frac{1}{\rho} f_{ij}(\theta) + O(\rho) \quad (2.120)$$

Now, all terms in the traction kernel will be considered to find corresponding $f_{ij}(\theta)$ expression required for regularising the integral.

For expression $a_{ij} = \frac{1}{r^2} (r_{,i} r_{,j} r_{,n})$,

$$\begin{aligned} \rho a_{ij} N^a J &= \rho \left(\frac{1}{\rho^2 A^2} + O\left(\frac{1}{\rho}\right) \right) \left(\frac{A_i(\theta)}{A(\theta)} + O(\rho) \right) \left(\frac{A_j(\theta)}{A(\theta)} + O(\rho) \right) O(\rho) (N^a(\eta) + O(\rho)) \\ &= O(\rho) \end{aligned} \quad (2.121)$$

hence, it is already regular.

For expression $c_{ij} = \frac{1}{r^2} r_{,j} n_i$,

$$\begin{aligned} \rho c_{ij} N^a J &= \rho \left(\frac{1}{\rho^2 A^2} + O\left(\frac{1}{\rho}\right) \right) \left(\frac{A_j(\theta)}{A(\theta)} + O(\rho) \right) (N^a(\eta) + O(\rho)) (J_i(\eta) + O(\rho)) \\ &= \frac{1}{\rho} \frac{A_j(\theta)}{A^3(\theta)} N^a(\eta) J_i(\eta) + O(1) \end{aligned} \quad (2.122)$$

Thus, all relevant terms required for Cauchy Principal value integration have been considered to find out corresponding terms required for subtracting out the singularity.

Vanishing neighbourhood in the local plane

The explicit asymptotic expression is now derived for the contour of σ_ϵ^m in the local parameter plane in terms of ρ and θ . The contour of the neighbourhood e_ϵ of radius ϵ on S is given by the equation

$$\epsilon^2 = (x_k - y_k)(x_k - y_k); \quad \mathbf{x}, \mathbf{y} \in S \quad (2.123)$$

that is, in the ξ -plane

$$\epsilon^2 = \rho^2 A^2(\theta) + O(\rho^3) \quad (2.124)$$

Therefore, the contour of σ_ϵ^m , image of e_ϵ^m , is given by the equation

$$\begin{aligned} \rho &= \alpha(\epsilon, \theta) \\ &= \frac{\epsilon}{A(\theta)} + O(\epsilon^2) \\ &= \epsilon \beta(\theta) + O(\epsilon^2) \end{aligned} \quad (2.125)$$

where $\beta(\theta) = 1/A(\theta)$ and it carries all the information required to perform properly the limit process in ξ -plane.

Final formula for CPV integrals

The original CPV surface integral is

$$\begin{aligned} I_s &= \int_{S_p} H_{ij}(\mathbf{y}, \mathbf{x}) N^a(\xi(\mathbf{x})) dS(\mathbf{x}) \\ &= \lim_{\epsilon \rightarrow 0} \left\{ \sum_m \int_{S_p^m - e_\epsilon^m} H_{ij}(\mathbf{y}, \mathbf{x}) N^a(\xi(\mathbf{x})) dS(\mathbf{x}) \right\} \end{aligned} \quad (2.126)$$

After the introduction of the parametric representation on each element, the singular integral becomes

$$I_s = \lim_{\epsilon \rightarrow 0} \left\{ \sum_m \int_{R^m - \sigma_\epsilon^m} H_{ij}(\mathbf{y}, \mathbf{x}(\xi)) N^a(\xi) J^m(\xi) d\xi \right\} \quad (2.127)$$

and in local polar coordinates,

$$I_s = \lim_{\epsilon \rightarrow 0} \left\{ \sum_m \int_{\theta_1^m}^{\theta_2^m} \int_{\alpha^m(\epsilon, \theta)}^{\rho^m(\theta)} F_{ij}^m(\rho, \theta) d\rho d\theta \right\} \quad (2.128)$$

Adding and subtracting on each element around \mathbf{y} , the corresponding asymptotic expression $f_{ij}^m(\theta)/\rho$ of the integrand function, the original CPV results in an alternative form more suitable for actual computation.

$$\begin{aligned} I_s &= \sum_m \int_{\theta_1^m}^{\theta_2^m} \int_0^{\rho^m(\theta)} [F_{ij}^m(\rho, \theta) - f_{ij}^m(\theta)/\rho] d\rho d\theta + \lim_{\epsilon \rightarrow 0} \left\{ \sum_m \int_{\theta_1^m}^{\theta_2^m} f_{ij}^m(\theta) \ln \left(\frac{\rho^m(\theta)}{\alpha^m(\epsilon, \theta)} \right) d\theta \right\} \\ &= \sum_m \int_{\theta_1^m}^{\theta_2^m} \int_0^{\rho^m(\theta)} [F_{ij}^m(\rho, \theta) - f_{ij}^m(\theta)/\rho] d\rho d\theta + \int_{\theta_1^m}^{\theta_2^m} f_{ij}^m(\theta) \ln \left(\frac{\rho^m(\theta)}{\beta^m(\theta)} \right) d\theta \end{aligned} \quad (2.129)$$

No limit is no longer present. Because,

$$\lim_{\epsilon \rightarrow 0} \ln \epsilon \left\{ \sum_m \int_{\theta_1^m}^{\theta_2^m} f_{ij}^m(\theta) d\theta \right\} = 0 \quad (2.130)$$

Therefore, the original CPV integral on S_p can be expressed as a sum of double and one-dimensional regular integrals, each one in terms of local coordinates. Each term in the final sum refers to one element at the time, thus allowing the computation to be performed in an element-by-element fashion. The actual computation is performed by using Gauss-Legendre quadrature formulae and dividing the element into triangular subelements. In the above formula, $\rho^m(\theta)$ is the value of ρ , corresponding to the point at the end of zone 1 (section 2.5.1) along the ray pertaining to the Gaussian value of θ in the element under consideration. For the remaining two zones (section 2.5.1) on each ray, ordinary Gaussian integration is possible as integral is regular.

Non-linear transformation

Above regularization technique consists in subtracting the intrinsic singularity to the singular kernel obtaining a regular integral that can be computed via standard quadratures and adding afterwards the integral of that intrinsic singularity performed analytically. But computation of the first integral on the right hand side of the equation (2.129) is poor as the integrand is the difference between two infinities of the same order and coefficient. So a nonlinear transformation is used in this work having null Jacobian at collocation point to improve the accuracy of integration. Radial variable ρ of the polar coordinates is transformed by the non-linear transformation used by Doblaré and Gracia [66].

S	integration element
S'	projection of S on the $\zeta_1 - \zeta_2$ plane
P	source point
Q ($\zeta_1(\xi_1, \xi_2), \zeta_2(\xi_1, \xi_2), \zeta_3(\xi_1, \xi_2)$)	point on the element
Q'($\zeta_1, \zeta_2, 0$)	projection of Q on the $\zeta_1 - \zeta_2$ plane
Q ₀ ($x_1(\xi_1^0, \xi_2^0), x_2(\xi_1^0, \xi_2^0), x_3(\xi_1^0, \xi_2^0)$)	the closest point to P on S.

This direction-dependent transformation is chosen as it results in distribution of Gauss points that is almost a perfect circle about the point of collocation. The transformation $\mu \in (-1, 1) \rightarrow \rho \in (0, \rho^m(\theta))$ is

$$\rho(\mu, \theta) = \frac{B}{r_{,\rho}(-1, \theta)}(\mu + 1)^3 + \left(\frac{\rho^m(\theta)}{16} - \frac{B}{2r_{,\rho}(-1, \theta)} \right) (\mu + 1)^4 \quad (2.131)$$

with $\min_{\theta} \rho^m(\theta) \geq B \geq 0$ in order to be monotonic. Here, $\min_{\theta} \rho^m(\theta)/4$ has been used for B . Here, $r_{,\rho}(-1, \theta)$ is the same as $A(\theta)$ computed in equation (2.113). This transformation is seen to improve the accuracy of CPV integrals.

2.6.1 Quasi-singular integration

In order to achieve a high level of accuracy in the boundary element formulation, all integrals involved must be accurately evaluated. Near-singular integrals need to be calculated accurately. Cruse and Aithal [8] proposed an algorithm similar to the singularity subtraction technique. This algorithm was used and improved upon by Mi and Aliabadi [69] for elastostatic crack problems. In this thesis, the same algorithm has been extended to elastodynamic case. In this method, only the boundary variables are expanded and integration is carried out partially in real space and partially in intrinsic space. Accurate integration results are obtained.

The integration coordinate system

The algorithm is based on the Taylor series expansion of boundary variables. The expansion is taken at Q_0 which is the closest point on the element to source point P . The integration system is set up on the tangent plane of the element at Q_0 . This tangent plane $\zeta_1 - \zeta_2$ and the integration coordinate system are shown in figure 2.6. The notation used is as follows:

The normal vector \mathbf{n} of the tangent plane at the closest point $Q_0(\xi_1^0, \xi_2^0)$ is given by

$$\mathbf{n} = \mathbf{A} \times \mathbf{B} / |\mathbf{A} \times \mathbf{B}| \quad (2.132)$$

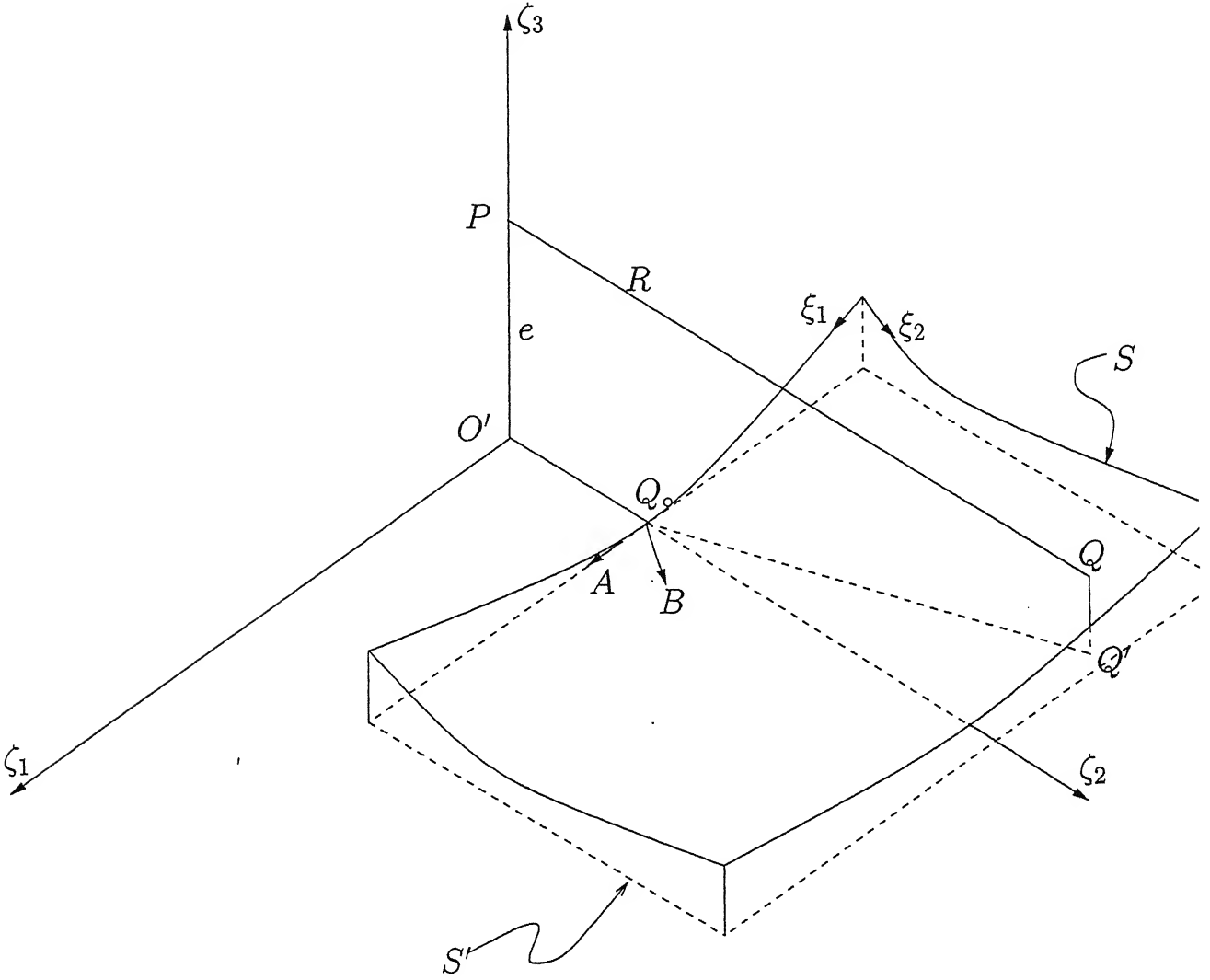


Figure 2.6: The integration coordinate system.

where

$$\begin{aligned}
 A &= \left\{ \frac{\partial x_1}{\partial \xi_1}, \frac{\partial x_2}{\partial \xi_1}, \frac{\partial x_3}{\partial \xi_1} \right\} \Big|_{(\xi_1^0, \xi_2^0)} \\
 &= \{x_1^\alpha, x_2^\alpha, x_3^\alpha\} M_{,1}^\alpha (\xi_1^0, \xi_2^0)
 \end{aligned} \tag{2.133}$$

$$\begin{aligned}
 B &= \left\{ \frac{\partial x_1}{\partial \xi_2}, \frac{\partial x_2}{\partial \xi_2}, \frac{\partial x_3}{\partial \xi_2} \right\} \Big|_{(\xi_1^0, \xi_2^0)} \\
 &= \{x_1^\alpha, x_2^\alpha, x_3^\alpha\} M_{,2}^\alpha (\xi_1^0, \xi_2^0)
 \end{aligned} \tag{2.134}$$

and

$$x_i = x_i^\alpha M^\alpha (\xi_1, \xi_2); \quad -1 \leq \xi \leq 1; \quad i = 1, 3; \quad \alpha = 1, 8. \tag{2.135}$$

The terms $M_{,j}^\alpha$ ($j = 1, 2$) denote the derivatives of shape functions M_α with respect to ξ_j and x_i^α are the values of the geometric coordinates x_i at the nodal point.

The tangent plane is constructed using the normal \mathbf{n} and the point Q_0 . The integration coordinate system takes the integration plane as the coordinate plane on which ζ_1, ζ_2 lie. The vector $\mathbf{e}_3 = \mathbf{n}$ is taken as the ζ_3 direction in the integration system and $\mathbf{e}_1 = \mathbf{A}/|\mathbf{A}|$ as the ζ_1 direction. Therefore, the ζ_2 direction is obtained from vector product $\mathbf{e}_2 = \mathbf{e}_3 \times \mathbf{e}_1/|\mathbf{e}_3 \times \mathbf{e}_1|$. The origin of the integration coordinate system, O' is chosen as the projection of the source point on ζ_1 - ζ_2 plane. It is obtained by solving the linear equations:

$$(\mathbf{P} - \mathbf{O}') \cdot \mathbf{A} = 0 \quad (2.136)$$

$$(\mathbf{P} - \mathbf{O}') \cdot \mathbf{B} = 0 \quad (2.137)$$

$$(\mathbf{Q}_0 - \mathbf{O}') \cdot (\mathbf{A} \times \mathbf{B}) = 0 \quad (2.138)$$

for unknown coordinates of point O' . The coordinate transformation of a space point \mathbf{X} in the original system to the integration system \mathbf{X}' is given as

$$\begin{aligned} \mathbf{X}' &= (\zeta_1, \zeta_2, \zeta_3) \\ &= (\mathbf{e}_1 \cdot (\mathbf{X} - \mathbf{O}'), \mathbf{e}_2 \cdot (\mathbf{X} - \mathbf{O}'), \mathbf{e}_3 \cdot (\mathbf{X} - \mathbf{O}')) \end{aligned} \quad (2.139)$$

The Taylor expansion of the displacement field

The displacements u_i at a time-step N are expressed in terms of the shape functions N^α as

$$u_i(\xi_1, \xi_2) = u_i^\alpha N^\alpha(\xi_1, \xi_2) \quad (2.140)$$

The Taylor expansion of u_i about $Q_0(\xi_1^0, \xi_2^0)$ can be written as

$$\begin{aligned} u_i &= u_i(Q_0) + \frac{\partial u_i}{\partial \zeta_1} \Delta \zeta_1 + \frac{\partial u_i}{\partial \zeta_2} \Delta \zeta_2 + \frac{1}{2} \frac{\partial^2 u_i}{\partial \zeta_1^2} (\Delta \zeta_1)^2 + \frac{\partial^2 u_i}{\partial \zeta_1 \partial \zeta_2} (\Delta \zeta_1)(\Delta \zeta_2) + \frac{1}{2} \frac{\partial^2 u_i}{\partial \zeta_2^2} (\Delta \zeta_2)^2 + O(\delta^3) \\ &= D(u_i) + O(\delta^3) \end{aligned} \quad (2.141)$$

where

$$\begin{aligned} \delta &= \sqrt{(\Delta \zeta_1)^2 + (\Delta \zeta_2)^2} \\ &= \sqrt{(\zeta_1 - \zeta_1(Q_0))^2 + (\zeta_2 - \zeta_2(Q_0))^2} \end{aligned} \quad (2.142)$$

The first order derivatives used above can be expressed as

$$\begin{pmatrix} \frac{\partial u_i}{\partial \zeta_1} \\ \frac{\partial u_i}{\partial \zeta_2} \end{pmatrix} = \begin{pmatrix} \frac{\partial \zeta_1}{\partial \xi_1} & \frac{\partial \zeta_2}{\partial \xi_1} \\ \frac{\partial \zeta_1}{\partial \xi_2} & \frac{\partial \zeta_2}{\partial \xi_2} \end{pmatrix} \begin{pmatrix} \frac{\partial u_i}{\partial \xi_1} \\ \frac{\partial u_i}{\partial \xi_2} \end{pmatrix} \quad (2.143)$$

and the terms $\frac{\partial u_i}{\partial \zeta_1}, \frac{\partial u_i}{\partial \zeta_2}$ are obtained as

$$\begin{pmatrix} \frac{\partial u_i}{\partial \zeta_1} \\ \frac{\partial u_i}{\partial \zeta_2} \end{pmatrix} = \begin{pmatrix} \frac{\partial \zeta_1}{\partial \xi_1} & \frac{\partial \zeta_2}{\partial \xi_1} \\ \frac{\partial \zeta_1}{\partial \xi_2} & \frac{\partial \zeta_2}{\partial \xi_2} \end{pmatrix}^{-1} \begin{pmatrix} \frac{\partial u_i}{\partial \xi_1} \\ \frac{\partial u_i}{\partial \xi_2} \end{pmatrix} \quad (2.144)$$

The terms on the right hand side of above equation can be evaluated explicitly through the use of shape functions for geometry $\zeta_i = \zeta_i^\alpha M^\alpha(\xi_1, \xi_2)$ and the displacement $u_i = u_i^\alpha N^\alpha(\xi_1, \xi_2)$. Also, $\frac{\partial \zeta_i}{\partial \xi_1} = \zeta_i^\alpha M_{,j}^\alpha(\xi_1^0, \xi_2^0)$ and ζ_i^α for each element can be evaluated with help of equation (2.139). The second order derivatives can be obtained from

$$\begin{pmatrix} \left(\frac{\partial \zeta_1}{\partial \xi_1}\right)^2 & 2\frac{\partial \zeta_1}{\partial \xi_1} \frac{\partial \zeta_2}{\partial \xi_1} & \left(\frac{\partial \zeta_2}{\partial \xi_1}\right)^2 \\ \frac{\partial \zeta_1}{\partial \xi_2} \frac{\partial \zeta_1}{\partial \xi_1} & \frac{\partial \zeta_2}{\partial \xi_2} \frac{\partial \zeta_1}{\partial \xi_1} + \frac{\partial \zeta_1}{\partial \xi_2} \frac{\partial \zeta_2}{\partial \xi_1} & \frac{\partial \zeta_2}{\partial \xi_2} \frac{\partial \zeta_2}{\partial \xi_1} \\ \left(\frac{\partial \zeta_1}{\partial \xi_2}\right)^2 & 2\frac{\partial \zeta_1}{\partial \xi_2} \frac{\partial \zeta_2}{\partial \xi_2} & \left(\frac{\partial \zeta_2}{\partial \xi_2}\right)^2 \end{pmatrix} \begin{pmatrix} \frac{\partial^2 u_i}{\partial \zeta_1^2} \\ \frac{\partial^2 u_i}{\partial \zeta_1 \partial \zeta_2} \\ \frac{\partial^2 u_i}{\partial \zeta_2^2} \end{pmatrix} = \begin{pmatrix} \frac{\partial^2 u_i}{\partial \xi_1^2} - \frac{\partial u_i}{\partial \zeta_1} \frac{\partial^2 \zeta_1}{\partial \xi_1^2} - \frac{\partial u_i}{\partial \zeta_2} \frac{\partial^2 \zeta_2}{\partial \xi_1^2} \\ \frac{\partial^2 u_i}{\partial \xi_1 \partial \xi_2} - \frac{\partial u_i}{\partial \zeta_1} \frac{\partial^2 \zeta_1}{\partial \xi_1 \partial \xi_2} - \frac{\partial u_i}{\partial \zeta_2} \frac{\partial^2 \zeta_2}{\partial \xi_1 \partial \xi_2} \\ \frac{\partial^2 u_i}{\partial \xi_2^2} - \frac{\partial u_i}{\partial \zeta_1} \frac{\partial^2 \zeta_1}{\partial \xi_2^2} - \frac{\partial u_i}{\partial \zeta_2} \frac{\partial^2 \zeta_2}{\partial \xi_2^2} \end{pmatrix} \quad (2.145)$$

where $\frac{\partial \zeta_j}{\partial \xi_k}$ and $\frac{\partial^2 \zeta_j}{\partial \xi_k \partial \xi_l}$ can be evaluated from $\zeta_j = \zeta_j^\alpha M^\alpha(\xi_1, \xi_2)$. Therefore, $\frac{\partial^2 u_i}{\partial \zeta_1^2}, \frac{\partial^2 u_i}{\partial \zeta_1 \partial \zeta_2}, \frac{\partial^2 u_i}{\partial \zeta_2^2}$ are computed by using equation (2.145).

Semi-analytical integration

Refer to figure 2.6, the distance between points Q and Q' is denoted by Δ and the distance Q' to Q_0 by δ . There is a relationship $\Delta \propto \delta^2$ between these variables, since Q_0 is the tangent point of a tangent plane of smooth surface S . The near-singular integral for any singular or hypersingular kernel T_{kij} can be written as

$$\begin{aligned} I &= \int_S T_{kij}(P, Q) u_k(Q) dS(Q) \\ &= \int_{S'} T_{kij}(P, Q) u_k(Q) J(Q') dS'(Q') \\ &= \int_{S'} [T_{kij}(P, Q) u_k(Q) J(Q') - T_{kij}(P, Q') D(u_k)] dS'(Q') + \int_{S'} T_{kij}(P, Q') D(u_k) dS'(Q') \\ &= I_n + I_a \end{aligned} \quad (2.146)$$

The first integral is evaluated numerically, while the second integral is evaluated semi-analytically. The first integral can be written as

$$I_n = \int_{S'} T_{kij}(P, Q') \{D(u_k) O(\delta^2) + O(\delta^3)\} dS'(Q') \quad (2.147)$$

since

$$T_{kij}(P, Q) = T_{kij}(P, Q') \{1 + O(\delta^2)\} \quad (2.148)$$

$$J(Q') = 1 + O(\delta^2) \quad (2.149)$$

$$u_k = D(u_k) + O(\delta^3) \quad (2.150)$$

If the integration element is flat, S will coincide with the projection S' , and $T_{kij}(P, Q) = T_{kij}(P, Q')$ and $J(Q') = 1$. However, this is not the case when the integration element is curved.

Numerical integration for I_n is performed in the same manner as explained in section 2.5.1 by subdividing the intrinsic element with closest point as the vertex. And Gauss-Legendre quadrature is done along radial and theta directions.

The second integral I_a is evaluated on the (ζ_1, ζ_2) plane after transformation to the polar coordinate system. The procedure is similar to that of Cruse and Aithal [8], that is, ρ -integration of the polar coordinate is performed analytically, while θ -integration is done numerically.

2.6.2 Detailed procedure for analytical integration

Any point Q' on (ζ_1, ζ_2) plane can be represented as $(\rho \cos \theta, \rho \sin \theta)$. Its corresponding coordinates in original or global x_α coordinate system can be found by solving the equations resulting from $(\mathbf{e}_1 \cdot (\mathbf{x} - \mathbf{O}'), \mathbf{e}_2 \cdot (\mathbf{x} - \mathbf{O}'), \mathbf{e}_3 \cdot (\mathbf{x} - \mathbf{O}')) = (\rho \cos \theta, \rho \sin \theta, 0)$. Original coordinates are found as a function of ρ and θ as follows:

$$D = \text{Determinant of } \begin{pmatrix} e_{11} & e_{12} & e_{13} \\ e_{21} & e_{22} & e_{23} \\ e_{31} & e_{32} & e_{33} \end{pmatrix} \quad (2.151)$$

$$\begin{aligned} x_1(Q') - x_1(P) &= \frac{1}{D} [\rho \cos \theta (e_{22}e_{33} - e_{32}e_{23}) - \rho \sin \theta (e_{12}e_{33} - e_{32}e_{13})] + x_1(O') - x_1(P) \\ &= b_{01}(\theta) + \rho b_{11}(\theta) \end{aligned} \quad (2.152)$$

In the above, for example, e_{11}, e_{12}, e_{13} are components of vector \mathbf{e}_1 . Also, $x_\alpha(O')$ and $x_\alpha(P)$ represent x_α coordinates of origin of new coordinate system on the tangent plane and source point in the original frame of reference, respectively. Similarly, expressions can be found for coordinates x_2 and x_3 .

Distance from source point to receiver point on projected element on tangent plane is $r = \sqrt{e^2 + \rho^2}$, where e is distance between source point and O' .

Since, $r_{,i} = \frac{x_i(Q') - x_i(P)}{r}$, $i = 1, 2, 3$

where $x_i(Q')$ are coordinates of receiver point on projected element and $x_i(P)$ are coordinates of source point. Putting values of coordinates of receiving point on the tangent plane in expression for $r_{,i}$ yields

$$r_{,i} = \frac{1}{r} (b_{0i}(\theta) + \rho b_{1i}(\theta)) \quad (2.153)$$

where b_{0i} and b_{1i} are constants that are function of θ for the particular element.

$$\begin{aligned}
 r_{,n} &= r_{,1} e_{31} + r_{,2} e_{32} + r_{,3} e_{33} \\
 &= \frac{1}{r} [(b_{01} + b_{11}\rho) e_{31} + (b_{02} + b_{12}\rho) e_{32} + (b_{03} + b_{13}\rho) e_{33}] \\
 &= \frac{1}{r} [(b_{01}e_{31} + b_{02}e_{32} + b_{03}e_{33}) + \rho(b_{11}e_{31} + b_{12}e_{32} + b_{13}e_{33})] \\
 &= \frac{1}{r} (b_{0n}(\theta) + \rho b_{1n}(\theta))
 \end{aligned} \tag{2.154}$$

Thus, all terms involved in the kernels can be transformed to original coordinate system x_α as function of polar coordinates ρ and θ .

Similarly,

$$\begin{aligned}
 D(u_i) &= u_i(Q^0) + \frac{\partial u_i}{\partial \zeta_1} \Delta \zeta_1 + \frac{\partial u_i}{\partial \zeta_2} \Delta \zeta_2 + \frac{1}{2} \frac{\partial^2 u_i}{\partial \zeta_1^2} (\Delta \zeta_1)^2 + \frac{\partial^2 u_i}{\partial \zeta_1 \partial \zeta_2} \Delta \zeta_1 \Delta \zeta_2 + \frac{1}{2} \frac{\partial^2 u_i}{\partial \zeta_2^2} (\Delta \zeta_2)^2 \\
 &= N^\alpha u_i^\alpha + \frac{\partial u_i}{\partial \zeta_1} (\rho \cos \theta - \zeta_1(Q_0)) + \frac{\partial u_i}{\partial \zeta_2} (\rho \sin \theta - \zeta_2(Q_0)) + \frac{1}{2} \frac{\partial^2 u_i}{\partial \zeta_1^2} (\rho \cos \theta - \zeta_1(Q_0))^2 \\
 &\quad + \frac{\partial^2 u_i}{\partial \zeta_1 \zeta_2} (\rho \cos \theta - \zeta_1(Q_0)) (\rho \sin \theta - \zeta_2(Q_0)) + \frac{1}{2} \frac{\partial^2 u_i}{\partial \zeta_2^2} (\rho \sin \theta - \zeta_2(Q_0))^2 \\
 &= \{A_0^\alpha(\theta) + \rho A_1^\alpha(\theta) + \rho^2 A_2^\alpha(\theta)\} u_i^\alpha, \quad \text{where } \alpha = 1, 8.
 \end{aligned} \tag{2.155}$$

All derivatives in equation (2.155) are calculated at Q_o , the closest point to P on S . Term $r_{,i} D(u_j)$ can be written as

$$\begin{aligned}
 r_{,i} D(u_j) &= \frac{1}{r} (b_{0i} + b_{1i}\rho) (A_0^\alpha + \rho A_1^\alpha + \rho^2 A_2^\alpha) u_j^\alpha \\
 &= \frac{1}{r} (c_{0i}^\alpha + c_{1i}^\alpha \rho + c_{2i}^\alpha \rho^2 + c_{3i}^\alpha \rho^3) u_j^\alpha
 \end{aligned} \tag{2.156}$$

Terms like $r_{,i} r_{,j} D(u_k)$ can be written as

$$\begin{aligned}
 r_{,i} r_{,j} D(u_k) &= \frac{1}{r^2} (b_{0i} + b_{1i}\rho) (c_{0i}^\alpha + c_{1i}^\alpha \rho + c_{2i}^\alpha \rho^2 + c_{3i}^\alpha \rho^3) u_k^\alpha \\
 &= \frac{1}{r^2} \{d_0^\alpha(i, j) + d_1^\alpha(i, j) \rho + d_2^\alpha(i, j) \rho^2 + d_3^\alpha(i, j) \rho^3 + d_4^\alpha(i, j) \rho^4\} u_k^\alpha
 \end{aligned}$$

Further $r^2 = e^2 + \rho^2$, where e is a constant for a particular element. It is already seen in section 2.5.1 that all temporal terms after analytical integration can be reduced to the form $(a + br + c/r^2)$. So all terms of displacement and traction kernels, in the expressions to be analytically integrated with respect to ρ , can be expressed completely as a function of ρ and θ . After analytical integration with respect to ρ , numerical integration with respect to θ is done as follows.

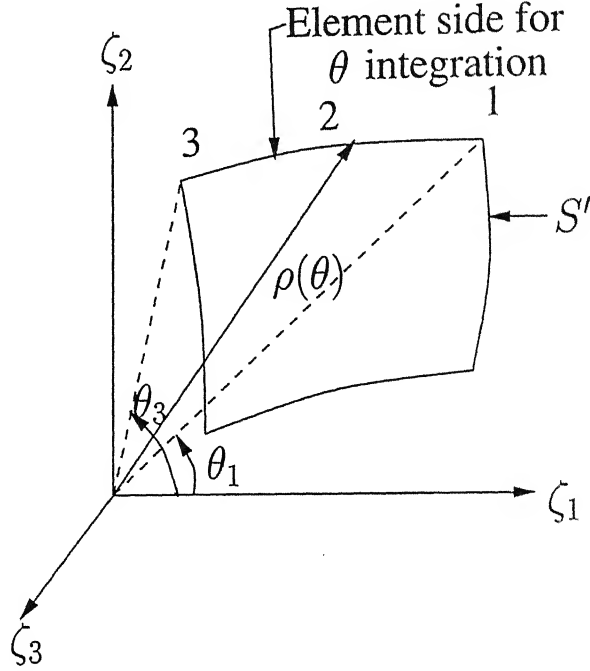


Figure 2.7: Definition for the angular variable integration.

Theta integration algorithm

Fig. 2.7 shows an element projected on the tangent plane and the coordinate system for semi-analytical integration. Each side of the element is given by three nodes. Any ray to the element starting from O' intersects two line segments, unless O' lies on the projected element itself. For every θ , ρ_{max} and ρ_{min} can be found corresponding to the farthest and closest point to O' on the element boundary. Now, intersection point of the ray with a side of the element is found by solving

$$\zeta_1 = N_i(\xi) \zeta_{1i} \quad (2.157)$$

$$\zeta_2 = N_i(\xi) \zeta_{2i} \quad (2.158)$$

$$y/x = \tan \theta \quad (2.159)$$

Hence, values of intrinsic coordinate ξ , pertaining to points of intersection of ray with both line segments of element boundary, are found corresponding to Gauss point value of θ . Thereafter, values of ζ_1 and ζ_2 can be computed from the values of intrinsic coordinates of intersection point. And ρ is calculated by $\rho^2 = \zeta_1^2 + \zeta_2^2$. Thus, values of ρ_{min} and ρ_{max} are computed for any value of θ .

Gaussian quadrature formula for integration with respect to θ is:

$$\begin{aligned} \int_{\rho_{\min}}^{\rho_{\max}} \int_{\theta_1}^{\theta_3} f(\rho, \theta) d\theta d\rho &= \sum_i \frac{1}{2}(\theta_3 - \theta_1) w_i \int_{\rho_{\min}}^{\rho_{\max}} f(\rho, \theta_i) d\rho \\ &= \sum_i \frac{1}{2}(\theta_3 - \theta_1) w_i g(\theta_i) \end{aligned} \quad (2.160)$$

Here, w_i are the weighting factors and θ_i are corresponding Gauss points over the interval $\theta_1 - \theta_2$. Thus, integration with respect to θ can be performed numerically.

This approach for nearly singular integrals is resorted to only if the distance of source point to receiver element is less than the length of diagonal of receiver element.

Angular variable transformation

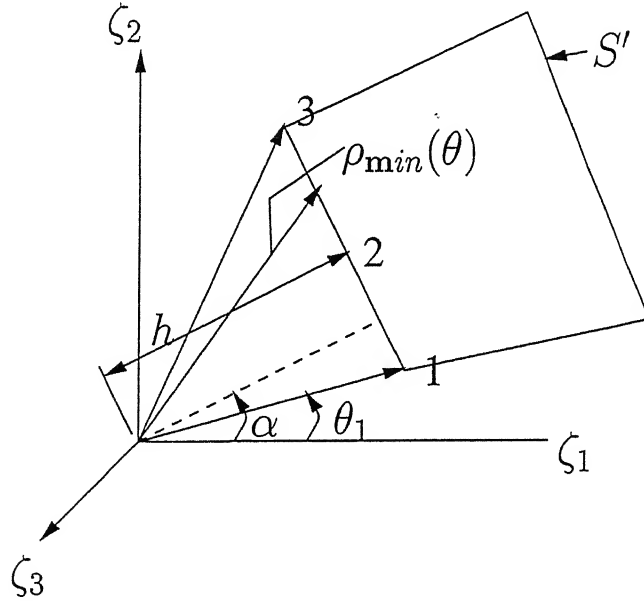


Figure 2.8: Nomenclature for angular transformation.

The number of integration points required in the angular direction to produce accurate results using polar coordinates increases rapidly as the source point projection approaches the edge of the projected element. This causes a problem not only for nearly singular integrals but also for singular integrals when using discontinuous elements, for which case the source point can be near the element edges. This phenomenon is termed as 'edge singularity'.

When O' is very close to an element edge (Fig. 2.8), the value of $\rho_{\min}(\theta)$ and hence the integrand with respect to the angular variable in the integral (2.160) can vary drastically

as θ varies from θ_1 to θ_3 . Thus a large number of integration points are required to perform the angular integration numerically.

In order to weaken the angular near singularity, Hayami [70] applied the angular variable transformation:

$$t(\theta) = \frac{h}{2} \log \left\{ \frac{1 + \sin(\theta - \alpha)}{1 - \sin(\theta - \alpha)} \right\} \quad (2.161)$$

where h is the perpendicular distance from point O' to the element edge and α is the angle made by this perpendicular with the ζ_1 axis of the coordinate system (Fig. 2.8). This transformation weakens the edge singularity in the angular direction as the Jacobian of the transformation is

$$\frac{d\theta}{dt} = \frac{1}{\rho_{\min}(\theta)} = \frac{\cos(\theta - \alpha)}{h} \quad (2.162)$$

Hence, the left hand side of equation (2.160) can be written as

$$\int_{\rho_{\min}}^{\rho_{\max}} \int_{\theta_1}^{\theta_3} f(\rho, \theta) d\theta d\rho = \int_{\rho_{\min}}^{\rho_{\max}} \int_{t(\theta_1)}^{t(\theta_3)} f(\rho, \theta(t)) \frac{d\theta}{dt} dt d\rho \quad (2.163)$$

Now, the integral can be written in the same form as the right hand side of equation (2.160) for its semi-analytical integration. This transformation is quite crucial for improving the accuracy of integration when source point is near the element edges.

Radial variable transformation

Consider a model radial variable integral:

$$I = \int_{\rho_{\min}}^{\rho_{\max}} \frac{\rho^m}{r^n} d\rho \quad (2.164)$$

where $r = \sqrt{\rho^2 + e^2}$ for planar elements. A radial variable transformation may be applied to weaken the near singularity due to $1/r^\alpha$. Hayami and Matsumoto [70] showed that the $L^{-1/5}$ transformation:

$$R(\rho) = -(\rho + e)^{-1/5} \quad (2.165)$$

gives near optimal results.

Equation (2.164) is transformed by the radial transformation $R(\rho)$ as:

$$I = \int_{R(\rho_{\min})}^{R(\rho_{\max})} \frac{\rho^m}{r^n} \frac{d\rho}{dR} dR \quad (2.166)$$

The $L_1^{-1/5}$ transformation gives:

$$\rho(R) = (-R)^{-5} - e \quad (2.167)$$

$$\frac{d\rho}{dR} = 5(R)^{-6} \quad (2.168)$$

Hence, the integral (2.164) can be expressed as:

$$I = \int_{R(\rho_{\min})}^{R(\rho_{\max})} \frac{((-R)^{-5} - e)^m (5(-R)^{-6})}{\{((-R)^{-5} - e)^2 + e^2\}^{n/2}} dR \quad (2.169)$$

which, in turn, can be transformed as :

$$I = \int_{-1}^1 \frac{((-R)^{-5} - e)^m (5(-R)^{-6})}{\{((-R)^{-5} - e)^2 + e^2\}^{n/2}} dR \frac{dR}{dx} dx = \int_{-1}^1 f(x) dx \quad (2.170)$$

where:

$$R = \frac{1}{2} [\{R(\rho_{\max}) - R(\rho_{\min})\} x + R(\rho_{\max}) + R(\rho_{\min})] \quad (2.171)$$

Above radial transformation may be used if the radial part of the integral on the projected element is numerically evaluated, instead of being analytically evaluated. At times, it may not be possible to evaluate integration of the radial part of the integral on the projected element analytically as in the case of integration of displacement kernel term for traction-singular quarter-point elements because of the presence of a square-root term present in the traction variable.

2.7 Quarter-point elements

In this crack element, the mid-point nodes of the element sides, normal to the crack front for eight-noded quadrilateral, or emanating from the crack-tip for the 6-noded triangle, are repositioned at the quarter-point locations on the crack side so that the following relation between field variables and distance r exist:

$$u(r) = A_1 + A_2\sqrt{r} + A_3r \quad (2.172)$$

$$t(r) = A_1 + A_2\sqrt{r} + A_3r \quad (2.173)$$

The displacement variation given in (2.172) contains the appropriate square-root of r term for modelling the near-front displacement field. However, since traction and displacement are independently modelled in the BEM, the quarter-point distortion does not reproduce

the correct traction singularity ahead of the crack. The inclusion of the correct singular term for the eight-noded element is accomplished by multiplying the shape functions for the element tractions by $\phi(r)$ as given below [71, 72],

$$\phi(r) = \frac{2}{1 + \xi} \quad (2.174)$$

The function $\phi(r)$ is $o(\frac{1}{\sqrt{r}})$ for r sufficiently small and assumes the value of one at the element side opposite to the crack-front or to the crack-tip, for the 8-node or 6-node elements, respectively. This ensures that correct singularity is achieved at the crack, and traction continuity is preserved along the element boundaries.

The combination of quarter-point distortion and shape function modification results in a quarter-point, traction-singular boundary element characterized by the following displacement and traction variations

$$u(r) = A_1 + A_2\sqrt{r} + A_3r \quad (2.175)$$

$$t(r) = B_1/\sqrt{r} + B_2 + B_3\sqrt{r} \quad (2.176)$$

Consider one side of a quadrilateral element, whose mid-side node has been shifted to

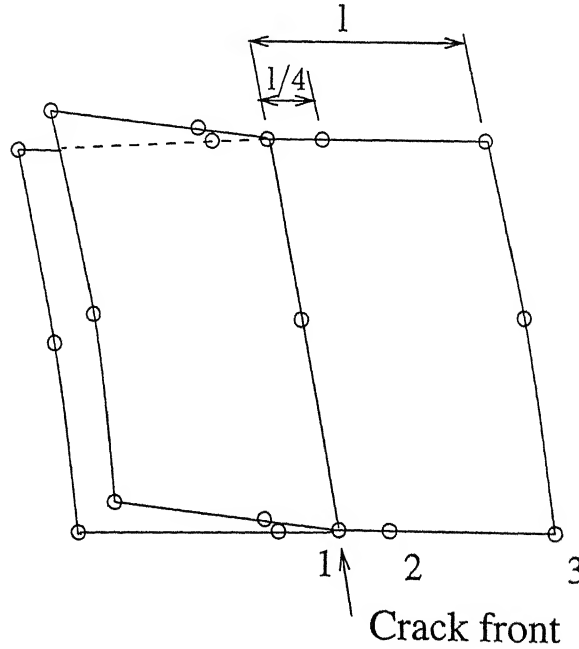


Figure 2.9: Quadratic quarter-point element

quarter-point position (Fig. 2.9). The singularity is included in the representation of the

tractions by using modified shape functions:

$$t_i = \bar{t}_i^1 \phi^1 \sqrt{\frac{l}{r}} + \bar{t}_i^2 \phi^2 \sqrt{\frac{l}{r}} + \bar{t}_i^3 \phi^3 \sqrt{\frac{l}{r}} \quad (2.177)$$

$$t_i = \bar{t}_i^1 \bar{\phi}^1 + \bar{t}_i^2 \bar{\phi}^2 + \bar{t}_i^3 \bar{\phi}^3 \quad (2.178)$$

where $\phi^1 = \frac{1}{2}\xi(\xi - 1)$, $\phi^2 = 1 - \xi^2$, $\phi^3 = \frac{1}{2}\xi(\xi + 1)$. And $\bar{\phi}^1, \bar{\phi}^2$ and $\bar{\phi}^3$ are the modified shape functions which include the $r^{-1/2}$ singularity.

Now, \bar{t}_i^j stands for the nodal values of t_i divided by the nodal values of $\bar{\phi}^j$:

$$\bar{t}_i^3 = t_i^3 \quad (2.179)$$

$$\bar{t}_i^2 = t_i^2 / 2 \quad (2.180)$$

$$\bar{t}_i^1 = \lim_{r \rightarrow 0} t_i^1 \sqrt{\frac{r}{l}} \quad (2.181)$$

The stress intensity factors can be computed directly by the boundary element code as follows:

$$\begin{aligned} K_I &= \bar{t}_2^1 \sqrt{2\pi l} \\ K_{II} &= \bar{t}_1^1 \sqrt{2\pi l} \\ K_{III} &= \bar{t}_3^1 \sqrt{2\pi l} \end{aligned} \quad (2.182)$$

It may be noted that the use of traction nodal values of the singular element at the crack tip for SIF computation is substantially less sensitive to the discretization than any of the displacement correlation procedures [60].

Almost all details of the formulation have been explained in this chapter. Same formulation works very well for quasi-static problems as well as by assigning very slow loading rates, dynamic problem reduces to static problem.

Chapter 3

Quasi-static Fracture Analysis

The effect of free surfaces on fracture characteristics for elastostatic problems is investigated using three-dimensional boundary element method. Stress intensity factors are calculated in BEM using traction values at the nodes along the crack front. A close correspondence between K_I computed from traction values and J_1^n integral is seen. Thus, it is possible to relate the evaluated state of stress at the crack vertex, where crack front meets the free surface, with a value of SIF. Thickness of boundary layer where free surface effects are predominant is estimated. Also, it is possible to estimate accurately the critical intersection angle of the crack front with the free surface at which square-root singularity is restored at the crack vertex. It may become possible to capture free surface retardation of crack growth accurately in crack propagation studies with the methodology used in this thesis.

3.1 Introduction

A crack front intersecting the free surface in a three-dimensional (3-D) body has been a subject of interest for the last three decades. Linear elastic fracture mechanics parameter stress intensity factor (SIF) is widely used in the characterization of material properties in the presence of a crack. SIF is defined as the strength of the square-root singularity at the crack tip. But SIF loses its significance at a corner point where a crack intersects a free surface. The power of the crack tip singularity changes in the vicinity of a corner point, and it is only possible to define stress intensity factors in an asymptotic sense. Precise behaviour is a function of Poisson's ratio (ν) and the inclination of the crack front to the free surface [2].

Benthem [1] analyzed a problem of a quarter-plane crack in a semi-infinite half-space subjected to symmetric loading. He derived that at the corner point, stresses have $r^{-0.452}$

singularity for Poisson's ratio equal to 0.3. Although it does not seem a dramatic change, it implies that the stress intensity factor at this point is equal to zero (or does not exist) since it is defined as the strength of the square-root singularity at the crack tip. It also causes the energy release rate to be equal to zero, since this can have a bounded, non-zero value only in the case of an exact r^{-1} singularity of the strain energy. Bažant and Estenssoro [2] confirmed Benthem's values for the singular eigenvalue at the crack vertex through a 3-D finite element analysis developed for conical regions. In addition, they considered intersections other than normal and found angles at which square-root singularity is restored. They used extrapolation procedures to estimate singularity indices corresponding to infinite degrees of freedom from results of eigenvalue analysis of a set of uniform grids. The success enjoyed by these local numerical analyses is not found to the same extent in finite element treatments of more global or complete problems which contain crack/surface intersections. Different predictions were made concerning the variation in energy release rate (G) with some results showing an increase in G in the free surface region, some a decrease and still others no change. Burton *et al.* [4] used a special set of integral equations for an elastic half-space weakened by a crack of finite width and infinite depth subjected to transverse excitation. They confirmed the existence of a weaker singularity at global crack/surface intersections with both integral equation formulation and finite element analysis of a finite geometry with adjustable singularity index at the crack vertex. They found by FEM a decay of G as free surface is approached ($z/a \rightarrow 0$) with the drop between the maximum value and that of the closest Gauss point (at $z/a = 0.015$) to the free surface being 30% of plane-strain value G_p when Poisson's ratio is 0.4. Nakamura and Parks [17] estimated thickness of boundary layer region as 3% of plate thickness. They used domain integral method to calculate local energy release rate J and calculated a drop in value of J of the order of 30% of two-dimensional plane-stress value of J . In FEM, calculation of J -integral at various positions along the crack front is constrained by the fact that accurate values of stresses are available only at Gauss points of the elements. Hence accurate determination of thickness of free surface boundary layer becomes difficult.

It can be observed in experiments that an initially straight-fronted crack in specimens such as a compact-tension specimen usually grows to a slightly curved shape under a fatigue load. Three-dimensional LEFM implies that for $\nu \neq 0$ the straight profiles associated with the varying energy release rates would not propagate as such but rather take up curved profiles with constant energy release rates. Burton *et al.* [4] generated critical crack profiles using FEM with each profile having less than 2% numerical variation in G with depth.

The crack profiles generated by them were significantly less curved than those observed in practice [5]. Similarly, using FEM, Bakker [18] predicted a relative tunnelling depth of 2.5 – 3% based on constant stress intensity distributions for self-similar crack propagation. Experimentally observed tunnelling depths on fatigue cracks are generally larger, closer to 5%, which is close to circular front. Using local eigenvalue analysis with FEM, Bažant and Estenssoro [2] found the critical intersection angle to be 101°, a value also observed experimentally [5] for $\nu = .3$. But in global situation, finite element analysis is not able to obtain an accurate stress state adjacent to the crack front in the region close to the free surface, especially for cracks which are not normal to the surface. Using FEM for analysis, Lin and Smith [6] found that slightly non-orthogonal intersection caused a great loss of path-independence in the value of J -integral up to 47% near the free surface.

The present work uses boundary element method to study the effect of free surface on state of stress near the crack vertex. SIFs can be computed along the crack front from nodal values of traction in boundary element analysis [73]. Amestoy *et al.* [74] derived for three dimensional configurations a path-independent parameter, J_1^n , equal to the potential energy release rate per unit of crack extension. The BEM is ideally suited to the evaluation of J_1^n integral, since the required stresses, strains and derivatives of the strains can be accurately calculated at the internal points in the body, with respective boundary integral equations. So it is possible to calculate J_1^n integral very close to the free surface, helping in more accurate estimation of thickness of boundary layer where free surface effects are predominant. In the present work, it is seen that SIFs, computed using nodal values of tractions at the crack front, closely correspond to J_1^n integral values along the crack front. Critical intersection angle of crack front with free surface computed in this work for a finite specimen matches closely with the value predicted by Bažant and Estenssoro for a half-space problem [2].

3.2 The Boundary Element Method

This section describes the salient features of the BEM applied to the present problem. The boundary integral equation relates displacement u_i and tractions t_i at the surface S of an elastic, homogeneous and isotropic body. It can be written as

$$C_{ij}(P)u_j(P) + \int_S T_{ij}(P, Q)u_j(Q) dS = \int_S U_{ij}(P, Q)t_j(Q) dS \quad (3.1)$$

where i, j range from 1 to 3 and P and Q are points on the surface S . The free-term tensor C_{ij} is calculated by general close-form expression developed by Mantic [56]. The

tensors $U_{ij}(P, Q)$ and $T_{ij}(P, Q)$ are the fundamental displacement and traction solutions, respectively, for a point force in an infinite domain (i.e., Kelvin's solution).

In this work, an approach [62] which combines the advantages of continuous and discontinuous elements in a single formulation has been used. In this formulation, expression of the shape and interpolation functions are unified in a form suitable for fully continuous, fully discontinuous or transition elements (i.e., discontinuous along one or more edges). One characteristic of the boundary element formulation is that discontinuities of the variables across the element edges do not invalidate the convergence of the technique [63].

The surface is divided into m eight-noded elements and on each element, the geometry, displacement and tractions are represented in terms of the respective nodal values x_i^s , u_i^s and t_i^s ($s = 1, 2, 3, \dots, 8$) as follows:

$$x_i(\xi, \eta) = \phi^s(\xi, \eta)x_i^s \quad (3.2)$$

$$u_i(\xi, \eta) = \phi_d^s(\xi, \eta)u_i^s \quad (3.3)$$

$$t_i(\xi, \eta) = \phi_t^s(\xi, \eta)t_i^s \quad (3.4)$$

where ϕ^s , ϕ_d^s , ϕ_t^s are shape functions of the intrinsic coordinates ξ and η .

The integral equation (3.1) is discretized as

$$C_{ij}(P^a)u_j(P^a) + \sum_{l=1}^m \sum_{s=1}^8 H_{ij}^{als} u_j^{ls} = \sum_{l=1}^m \sum_{s=1}^8 G_{ij}^{als} t_j^{ls} \quad (3.5)$$

where the surface point P has been taken to coincide with collocation node a of the discretization. Coefficients H_{ij}^{als} and G_{ij}^{als} are given by the integrals

$$G_{ij}^{als} = \int_{-1}^1 \int_{-1}^1 U_{ij}(P^a, Q^l(\xi, \eta)) \phi_t^s(\xi, \eta) J^l(\xi, \eta) d\xi d\eta \quad (3.6)$$

$$H_{ij}^{als} = \int_{-1}^1 \int_{-1}^1 T_{ij}(P^a, Q^l(\xi, \eta)) \phi_d^s(\xi, \eta) J^l(\xi, \eta) d\xi d\eta \quad (3.7)$$

where $J(\xi, \eta)$ is the Jacobian.

Three types of boundary nodes are identified depending on the function these fulfil:

1. Geometrical nodes: those used for interpolating the boundary geometry.
2. Interpolation nodes: the points on the boundary which define the interpolation of the variables. The system nodal values correspond to these nodes.
3. Collocation nodes: where the boundary integral equation is enforced.

Collocation and interpolation nodes for continuous elements coincide with the geometrical nodes. Collocation nodes and interpolation nodes for discontinuous elements and discontinuous side of transition elements are situated inside the element. For quarter-point element, geometrical and interpolation nodes coincide, but collocation corresponding to nodes on crack front is done at nodes situated inside the elements on either side of the crack front. To reduce the number of equations and enhance accuracy, equations corresponding to collocation nodes before and after a given interpolation node are added up [64].

Writing equation (3.5) for each of the n collocation nodes of the mesh leads, when proper boundary conditions are applied and the terms reordered, to a non-symmetric and fully populated system of $3n$ equations in $3n$ unknowns. Solving the system of equations generated from collocating displacement integral equation at all collocation nodes, boundary data of displacements and tractions get generated on the full surface of the specimen.

3.3 BEM Crack Elements

In this crack element, the mid-point nodes of the element sides, normal to the crack front for eight-noded quadrilateral, or emanating from the crack-tip for the 6-noded triangle, are repositioned at the quarter-point locations on the crack side so that the following relation between field variables and distance r exist:

$$u(r) = A_1 + A_2\sqrt{r} + A_3r \quad (3.8)$$

$$t(r) = A_1 + A_2\sqrt{r} + A_3r \quad (3.9)$$

The displacement variation given in (3.8) contains the appropriate square-root of r term for modelling the near-front displacement field. However, since traction and displacement are independently modelled in the BEM, the quarter-point distortion does not reproduce the appropriate traction singularity ahead of the crack. The inclusion of the correct singular term for the eight-noded element is accomplished by multiplying the shape functions for the element tractions by $\phi(r)$ as given below [71, 72],

$$\phi(r) = \frac{2}{1 + \xi} \quad (3.10)$$

The function $\phi(r)$ is $o(\frac{1}{\sqrt{r}})$ for r sufficiently small and becomes unity at the element side opposite to the crack front or to the crack-tip, for the 8-node or 6-node elements, respectively. This ensures that correct singularity is achieved at the crack, and traction continuity is preserved along the element boundaries.

The combination of quarter-point geometry and shape function modification results in a traction-singular boundary element characterized by the following displacement and traction variations

$$u(r) = A_1 + A_2\sqrt{r} + A_3r \quad (3.11)$$

$$t(r) = B_1/\sqrt{r} + B_2 + B_3\sqrt{r} \quad (3.12)$$

Consider one side of a quadrilateral element, whose mid-side nodes have been shifted to quarter-point position (Fig. 3.1). The singularity is included in the representation of the tractions by using modified shape functions:

$$t_i = \bar{t}_i^1 \phi^1 \sqrt{\frac{l}{r}} + \bar{t}_i^2 \phi^2 \sqrt{\frac{l}{r}} + \bar{t}_i^3 \phi^3 \sqrt{\frac{l}{r}} \quad (3.13)$$

$$t_i = \bar{t}_i^1 \bar{\phi}^1 + \bar{t}_i^2 \bar{\phi}^2 + \bar{t}_i^3 \bar{\phi}^3 \quad (3.14)$$

where $\phi^1 = \frac{1}{2}\xi(\xi - 1)$, $\phi^2 = 1 - \xi^2$, $\phi^3 = \frac{1}{2}\xi(\xi + 1)$.

Now, \bar{t}_i^j stands for the nodal values of t_i^j divided by the nodal values of ϕ^j :

$$\bar{t}_i^3 = t_i^3 \quad (3.15)$$

$$\bar{t}_i^2 = t_i^2/2 \quad (3.16)$$

$$\bar{t}_i^1 = \lim_{r \rightarrow 0} t_i^1 \sqrt{\frac{r}{l}} \quad (3.17)$$

The stress intensity factors may be computed directly by the boundary element code as follows:

$$\begin{aligned} K_I &= \bar{t}_2^1 \sqrt{2\pi l} \\ K_{II} &= \bar{t}_1^1 \sqrt{2\pi l} \\ K_{III} &= \bar{t}_3^1 \sqrt{2\pi l} \end{aligned} \quad (3.18)$$

It can be noted that the use of traction nodal values of the singular element at the crack front for SIF computation (3.18) is substantially less sensitive to the discretization than any of the displacement correlation procedures [73].

Further, for pure mode-I loading of the crack, the local energy release rate G (or J -integral) along the crack front can be expressed in terms of local stress intensity factor K_I according to

$$J = \frac{K_I^2(1 - \nu^2)}{E} \quad (3.19)$$

Since a plane strain state exists in the limit $r \rightarrow 0$ all along the crack front, the plane strain modulus $E/(1 - \nu^2)$ is used in this expression independent of the far field stress state.

3.4 J_1^n - integral

This section describes a J -integral suitable for 3-D crack configurations. Amestoy *et al.* [74] defined a J_1^n integral for linear or nonlinear elastic materials. J_1^n integral is equal to the potential energy release rate per unit of crack extension, i.e., the negative of the change of the potential energy of the configuration when a unit of crack front extends in the direction of the principal normal by an amount da at point s only, remaining elsewhere its original length. The value of J_1^n varies with the position s along the crack front and the term $J_1^n(s)$ is used to denote this dependence on position.

Given a configuration containing a traction-free crack with local axes x_1, x_2 and x_3 attached to the crack front at a distance s along the crack and where x_1 and x_3 lie in the plane of the crack at s , x_3 is tangent to the crack front at s , and x_1 is directed into the solid (Fig. 3.2), $J_1^n(s)$ is given by

$$\begin{aligned} J_1^n(s) &= \int_{\Gamma} (W^e n_1 - u_{i,1} t_i) d\Gamma - \int_A (\sigma_{i3} u_{i,1})_{,3} dA \\ &= J_C(s) + J_A(s) \end{aligned} \quad (3.20)$$

where

- $J_C(s)$ = a line integral evaluated over a contour that lies in the principal normal plane of the crack front at s and that encloses the crack-tip
- $J_A(s)$ = an integral evaluated over the planar area (surface) enclosed by the contour that includes the crack tip
- t_i = components of the traction vector defined according to the outward normal n along C , i.e., $t_i = \sigma_{ij} n_j$
- σ_{ij} = components of the stress tensor
- u_i = displacement in the x_i direction
- W_e = elastic strain energy density

Carpenter *et al.* [75] and Dodds *et al.* [76] had demonstrated the path-independence property of J_1^n integral for 3-point bend specimens. Dodds [77] demonstrated path-independence for J_1^n for tension and bending specimens. These studies concluded that quantity J_A is a well-behaved function and is less affected by numerical inaccuracies.

J_1^n is less sensitive to inaccuracy in computations in crack front elements as it is a global parameter. Values of stresses, strains and derivatives of strains are computed at

interior points using respective boundary integral equations for them. Interior variables are calculated more accurately in BEM because these are calculated with the help of global equations, rather than by local interpolation as in FEM. Rigby and Aliabadi [78] demonstrated the effectiveness of the boundary element method in combination with the J -integral technique for three-dimensional problems.

A typical distribution of Gauss points for J_I^n calculation is shown in Fig. 3.3. It can be seen that the area enclosed by the J -integral contour is divided into a number of segments, one of which is highlighted. For area integration, 2×2 Gauss points are chosen over each segment. J_C is evaluated by numerically integrating the contour integral over the outer arc (3 points Gauss quadrature is used for line integrals). The area integrand can be written as

$$I_A = \frac{\partial \sigma_{i3}}{\partial x_3} \frac{\partial u_i}{\partial x_1} + \sigma_{i3} \frac{\partial^2 u_i}{\partial x_1 \partial x_3} \quad (3.21)$$

I_A has a $1/r$ singularity but the area integral would tend to zero as $r \rightarrow 0$.

3.5 Numerical evaluation of boundary integrals

Analytical integration of the matrix coefficients in boundary integral equations is not, in general, possible and therefore, numerical quadrature must be used. The principal-value integrals involved in computation of H matrix (3.7) have been determined with the help of algorithm given by Guiggiani and Gigante [7], and non-linear transformation suggested by Doblaré and Gracia [66]. Algorithm proposed by Cruse and Aithal [8] and further extended to hypersingular kernel cases by Mi and Aliabadi [9], has been used for quasi-singular integrations. This algorithm is analogous to singularity subtraction technique. Nearest point on the element from collocation point is found by Newton-Raphson method. The element, over which integration is to be done, is projected on to the plane tangent at the closest node. In this method, boundary variables are expanded about the closest node. Integration is partially carried out in real space and partially in intrinsic space. Intrinsic space integration is fully numerical. Integration in real space, i.e., on projection of the element, is done semi-analytically in two stages: radial integration is done analytically and angular integration is done numerically. Angular variable transformation of Hayami [79] is used to weaken the angular near-singularity arising when collocation node is near the edge of an element.

A new algorithm for G -matrix for traction-singular elements

In the above quasi-singular integration procedure, radial integration in real space for traction-singular, quarter-point elements for G matrix (3.6) is done numerically as analytical integration is not possible due to an additional term $\sqrt{l/x}$ in shape functions for traction variables. The integrand, having the square root singular term in traction variable, is first integrated by parts resulting in two terms: an exact term and another term which is numerically integrated using $L^{-1/5}$ transformation given by Hayami and Matsumoto [70]. Integration by parts removes square-root singularity of traction variable from the integrand as shown below.

Suppose ABCD is a quarter-point element (Fig. 3.4). Side AB represents the crack front. Suppose this side AB is represented by $\xi = -1$ in intrinsic coordinates. Traction variable over the quarter-point element is represented in terms of the nodal values t_i^s ($s = 1, 2, 3, \dots, 8$) as

$$t_i(\xi, \eta) = (N^s(\xi, \eta)t_i^s) \phi(\xi) \quad (3.22)$$

where N^s are shape functions of the intrinsic coordinates ξ and η . And $\phi(\xi) = \frac{2}{1+\xi} = \sqrt{\frac{l}{x}}$. Terms l and x are explained in Fig. 3.4. For straight edge elements, x/l can be expressed as $x/l = a(\theta)\rho + b(\theta)$, where a and b are functions of θ only. For radial integration in real space, a general term of the integrand having $\sqrt{l/x}$ term can be expressed as

$$I = \int \frac{\rho^m}{(\rho^2 + e^2)^{n/2} \sqrt{a\rho + b}} d\rho \quad (3.23)$$

A field point on the projection of the element is located by (ρ, θ) coordinates. Distance between field point and collocation node is given by $\sqrt{\rho^2 + e^2}$, where e is the distance between the collocation point and its projection on to the tangent plane, i.e., center of the real space integration coordinate system.

Integral (3.23) can be integrated by parts and written in the form

$$I = \frac{2\sqrt{a\rho + b}\rho^m}{a(\rho^2 + e^2)^{n/2}} - \int \frac{2\sqrt{a\rho + b}}{a} \frac{(\rho^2 + e^2)^{n/2} m \rho^{m-1} - \rho^m n (\rho^2 + e^2)^{\frac{n}{2}-1} \rho}{(\rho^2 + e^2)^n} d\rho \quad (3.24)$$

Integral on the right hand side has been numerically integrated using $L^{-1/5}$ transformation given by Hayami and Matsumoto [70]. Integration by parts removes square-root singularity of traction variable from the integrand, thus improving the accuracy of integration.

3.6 Results and Discussion

Fig. 3.5 shows the geometry of the center crack tension specimen and the loading used in numerical analysis. The specimen has the parameters: $a/w = 0.24$, $h/w = 1$, $b/w = 0.5$ where a is the crack half-length, w is specimen half-width, h is half-height and b is specimen half-thickness. The material is assumed to be homogeneous and isotropic with shear modulus $\mu = 90$ G Pa and Poisson's ratio $\nu = 0.3$. The center crack specimen is loaded by a tensile load at $y = \pm h$ planes.

Due to the symmetry in the specimen geometry and loading, only one-eighth of the specimen is modelled in the boundary element analysis. Fig. 3.6 shows the boundary-element idealization of one-eighth of the center-crack specimen. Eight-node quadrilateral elements are used. A combination of continuous and discontinuous elements is used to reduce the overall degrees of freedom. The eight-node elements bordering the crack on the side of the crack surface are quarter-point elements, while the ones on the opposite side, i.e., ahead of the crack front are quarter-point, traction-singular elements. Triangular elements (collapsed eight-noded elements) are used to surround the intersection point of the crack front with the lateral facets. These triangular elements are modelled as quarter-point, traction-singular elements.

Appropriate boundary conditions are applied to the symmetry planes. This is done by restraining nodal displacements in the direction normal to the plane or planes of symmetry to which the node belongs. The nodes on the crack surface, except for those directly on the crack front or on the edges with lateral facets, are left free to move in three orthogonal directions.

Table 3.1 shows details of some of the meshes with varying degrees of refinement. Runs were performed for convergence study for a through straight center-crack specimen under Mode-I loading. The profiles of K_I along the thickness (Fig. 3.7) are seen to converge across the thickness except for the free boundary layer region. SIFs are calculated from values of traction at the crack front nodes. SIF value at the crack vertex is found to be sensitive to the boundary element idealization. The boundary element mesh used for analysis models square-root singularity all along the crack front including the crack vertex. But due to the actual singularity at the vertex being different from square-root, convergence in SIF at the vertex is not obtained with mesh refinement. But an increasing reduction in SIF at the vertex is seen, implying that singularity is weaker than square-root. Influence of weaker singularity is very well reflected in the lower value of SIF obtained at the crack vertex. Value of traction at crack vertex exhibits an integrated influence of reduced singularity

over the entire element at the crack vertex. Despite being mesh dependent, value of SIF calculated from crack vertex tractions reflects the level of singularity at the vertex. This feature may be used to capture accurately the changing singularity trends as intersection angle of the crack front changes to non-normal values.

The 3-D characteristics of the straight crack are studied using the mesh no. 4 (Table 3.1), which has 3317 nodes, 1075 elements and 9951 degrees of freedom. The selected mesh has 12 layers of elements on face containing the crack. The thicknesses of different layers after normalization with half-crack length are .008,.008,.024,.032,.048,.104,.208,.288,.316,.316,.316 and .316 respectively. Various three-dimensional aspects of fracture characteristics of a through-thickness center crack in a plate are enumerated as follows:

1. **Path-independence of J_1^n integral:** Circular contours around the crack front on planes parallel to the free surface are used for J_1^n computations. The computed values of J_C , J_A and J_1^n are shown in Fig. 3.8 and Fig. 3.9 as a function of radial distance of contour from crack front for several positions on the crack front. Although J_A varies with radial distance of outer contour from crack front, r , it clearly approaches zero as $r \rightarrow 0$. Also contribution of J_A term reduces sharply on moving away from free surface.

The parameter J_1^n varies through the thickness of the specimen and is the three-dimensional counterpart of the two-dimensional J integral. It should be noted that for 3-D configurations, J_C is no longer path-independent as it is for 2-D plane stress or plane strain configurations. The term J_A added to J_C gives path-independence to J_1^n . In Fig. 3.9, e.g., for $z/b = .004$, J_1^n shows almost zero variation for different contours while J_C shows 5% variation. But path-independence of J_1^n is not preserved at positions very close to the free surface. Shih *et al.* [80] reported a variation of 25% in the value of point-wise energy release rate near the free surface as calculated by domain integral method. In the present study, variations of nearly 50%, 16% and 8% are observed in J_1^n values at $z/b = 0.00006$, 0.0001 and 0.0002 respectively (Fig. 3.8). Here $z/b = 0.0$ denotes the free surface position. Thus, it is seen that path-independence of J_1^n is not preserved as one gets very close to the free surface. At the crack vertex, square-root singularity in the stresses is assumed for boundary element analysis, while a lower order singularity exists there. Hence, incorrect modelling of the stress field might have resulted in loss of path-independence near the free surface for J_1^n integral. But J_1^n values are seen to stabilize for contours at larger radial distance from crack front. Remote contour J_1^n values are taken as correct J_1^n values

in this work.

Fig. 3.10 shows variation of J_C along crack front for contours at different radial distances from crack front. Towards the mid-plane, J_C shows almost no variation with radial distance of contour from crack front. Also J_C matches closely with J computed from K_I with equation (3.19) closer to mid-plane. A lot of variation in value of J_C , calculated at $r/a = .008$, is seen in the thickness direction near the free surface. It implies stress field is changing sharply in thickness direction near crack vertex.

2. **Correspondence of J_1^n and K_I :** It is seen in Fig. 3.11 that J_1^n value at the free surface approaches the value of J calculated using equation (3.19) from K_I value computed with traction formula. Thus, SIF calculated from crack-tip tractions reflects the state of stress at the crack vertex, though the value of SIF is mesh-dependent.
3. **Thickness of free surface boundary layer:** Free surface boundary layer is the zone adjacent to the free surface where influence of the lower vertex singularity is felt. Burton *et al.* [4] found reduction in energy release rate to be 30% of plane-strain value at the closest Gauss point to the free surface ($z/a = .015$). In results from the present study, same reduction in value of J_1^n is seen at $z/a = .001$. An FEM analysis is constrained by the fact that accurate values of stresses can be calculated only at Gauss points of the elements, restricting calculations of G near free surface to the plane containing Gauss points of the elements in the layer adjoining the free surface. In BEM, values of stresses and derivatives of displacements can be calculated much closer to the free surface with the help of the respective boundary integral equations. Nakamura and Parks [17] estimated that corner singularity region extended up to a spherical radius of about 3% of plate thickness away from the intersection. The present study finds that boundary layer thickness, where J_1^n varies from low free surface values to 2-D plane strain value, is $z/a = .008$. Thus boundary layer where free surface effects are predominant is thinner than its previous estimates. In this study, a reduction to the extent of 50% of plane-strain J is observed in J_1^n value close to the free surface. Zero value of J_1^n is not achieved despite a weaker singularity than square-root at the vertex because square-root singularity in stresses is assumed all along the crack front in the boundary element model used for computation.
4. **Effect of plate thickness on SIF:** Fig. 3.12 shows values of normalized K_I along

the crack front for $\nu = 0.3$ for several thicknesses of the specimens. The two finite thickness extremes treated here are: (i) the thick specimen being that used to simulate the basic infinite geometry and having $b/a = 2.166$, (ii) the thin specimen having $b/a = 0.091$. For both the thick and the thin specimens, value of K_I is lower at free surface vertex ($z/a = 0$). For the thick specimen, it keeps increasing along the crack front till $z/a = 0.167$ and reaches a peak value there. Thereafter it decreases gradually to plane-strain value towards mid-surface. For the thin specimens, intermediate peak is never realized, rather K_I keeps increasing in value till mid-thickness. Similar behaviour was reported by Burton *et al.* [4].

5. **Effect of Poisson's ratio on SIF:** Fig. 3.13 shows influence of Poisson's ratio ν on Mode-I stress intensity distribution along the crack front. At the crack vertex, K_I reduces with increase in ν , implying singularity of stress field at the vertex grows weaker with increase in ν . Benthem [1] also found that Mode-I singularity exponent at the crack vertex gets weaker with increase in Poisson's ratio.

Opposite trend is observed with respect to Mode-II loading for normal intersection (Fig. 3.14). K_{II} at the crack vertex keeps increasing with increase in Poisson's ratio, implying an increasing trend in singularity exponent. Oscillation is noticed in K_{II} curves near the free surface. Explanation for this is that for Mode-II loading, singularity is stronger than square-root at crack vertex resulting in computed K_{II} value at the crack vertex being higher than that at the mid-surface. Consequently, free surface layer in pure Mode-II loading is taking more load or providing more resistance to the applied load. This results in inner layers taking less load in order to maintain equilibrium. Opposite behaviour is noticed for Mode-I loading where inner layers have higher SIF to compensate for part of the crack resistance lost in the breakthrough. Perhaps it is more difficult to handle a singularity stronger than square-root compared to a singularity weaker than square-root. A still thinner layer at the free surface would have smoothened the curve for K_{II} distribution along the crack front. Oscillations are also noticed in K_I curves in Fig. 3.7 for coarser meshes and K_I curves are smoothened on further refinement of the mesh. It seems that for Mode-II loading, greater mesh refinement is required compared to Mode-I loading.

6. **Transition from plane strain to plane stress in vicinity of crack front:** Plane strain constraint, defined as $\sigma_{zz}/\nu(\sigma_{xx} + \sigma_{yy})$, is equal to 0 for plane stress and to 1 for plane strain. For thick ($b/a = 2.166$) and thin ($b/a = .091$) plates,

contours in Fig. 3.15 and Fig. 3.16 respectively show how constraint values are lower in free boundary region compared to inner layers. Constraint keeps increasing with decreasing radial distance. For the thick plate, zero constraint region exists beyond radial distance from crack front, $r/a = .002$ near the free surface, and beyond $r/a = 1.7$ near mid-surface. If constraint > 0.9 is used as the criterion for the plane strain condition, the boundary of plane strain region lies near a radial distance of $.03a$ from the crack front at the mid-plane and at $r/a = .0002$ for $z/b = .003$. Near free surface, at $z/b = .00003$, constraint value of $.15$ is computed at $r/a = .0002$.

7. **Effects of crack front tunnelling:** Through-thickness fatigue cracks in plate geometries almost always show crack front tunnelling, i.e., a curved crack front with the the point of maximum length of the crack at the center. It is also observed that fatigue crack fronts penetrate the free surface at a non-zero angle with the normal to the free surface. Bazant and Estenssoro [2] argued that this angle is fixed by the angle at which the square-root singularity of stresses and strains at the free surface penetration is restored. They showed that the front edge of a planar Mode-I crack that propagates in an elastic isotropic plate in a plane normal to the plate surfaces must terminate at the surfaces with a certain angle β depending only on Poisson's ratio ν . Tests were carried out by Rolfe and Barsom [5] on structural steel in static loading according to E-399 ASTM Standard. Their test results showed that theoretical lines of inclination $\beta = 101^\circ$ with the plate surface agreed very well with the observed terminal directions of the first arrest marks, which corresponded to an essentially elastic fracture stage.

In the present study, calculations on tunnelling crack fronts are performed using circular crack fronts with different penetration angles, viz., 95° , 98° , 101° , 105° and 110° . The model selected for studying crack-tunnelling effect has 18 layers of elements of unequal thicknesses on face containing the crack. The model has 4245 nodes and 1345 elements and 12735 degrees of freedom. The thicknesses of different layers after normalization with half-crack length are $.008, .008, .016, .024, .024, .032, .048, .048, .048, .048, .064, .064, .064, .064, .08, .08, .08$ and $.08$ respectively. The specimen has geometrical parameters: $a/w = 0.24$, $h/w = 1$, $b/w = 0.22$. Also in the present study, mesh used for analysis of curved crack fronts is not orthogonal. For an orthogonal mesh, the elements surrounding the crack front have sides normal and parallel to the crack front. In a non-orthogonal mesh, the orientation of the element sides is arbitrary. In this study, the element sides that would be normal to the crack front for an orthog-

onal mesh are taken to be parallel to the free surface. This makes the direction of self-similar crack growth as parallel to the free surface in this study. The crack can grow in a self-similar manner in two directions: normal to the crack front or parallel to the free surface. A crack advance associated with energy release rate G calculated in the plane parallel to the free surface produces a crack that retains its shape [4]. Accordingly, self-similar crack growth direction has been taken as parallel to the free surface in this study.

Fig. 3.17 shows a comparison of the calculated through-thickness K_I -distributions for different penetration angles. Values of K_I are calculated from crack front tractions. These values exhibit certain oscillations along the crack front, as the modelled crack front is not smooth but is made of small straight line segments. The position of the corner nodes of crack front elements is determined from the assumed circular shape of the crack front, and the position of the mid-side nodes are then obtained as the mid-points of both neighbouring corner nodes. For correct interpolation of traction singularity in crack front elements in BEM, a restriction is imposed on the positions of nodes in the elements [81] requiring that crack front be straight. SIF values at the mid-side nodes is about 10% higher than those at the corner nodes. This SIF variation is caused by the inaccurate positioning of the mid-side nodes. The large difference of SIF values between the corner and the mid-side nodes demonstrates that the SIF variation along the crack front is very sensitive to the crack shape, even a small difference in crack front shape will cause a large discrepancy of SIF. Similar behaviour was reported by Lin and Smith [6] for a penny crack when polygonal line approximation is used for the crack front. They reported an 11% higher value at mid-side nodes compared to corner nodes, citing inaccurate positioning of the mid-side nodes as a reason for variation in SIF. But their SIF values were estimated by the J -integral method. They found it difficult to obtain an accurate stress state adjacent to the crack front in the region close to the free surface, especially for cracks which are not normal to the surface. They reported a loss of path-independence up to 47% near the free surface even for a slightly non-orthogonal intersection.

Fig. 3.18 shows the variation of K_I for different crack front intersection angles with free surface, after ignoring the mid-side node SIF values resulting in smooth profiles. It is seen that free surface SIF is greater than mid-surface SIF for intersection angles of 101° and higher. For intersection angle of 105° and beyond, SIF at the crack vertex is higher than SIF values of inner layers.

3.7 Conclusions

An elastostatic three-dimensional boundary element analysis of the center-crack tension specimen is performed. Values of J_1^n integral calculated along the crack front correspond well with the K_I values calculated from nodal traction values. At the corner intersection point of the crack front with the free surface, values of K_I , directly available from BEM solution, correspond closely with J_1^n value calculated on plane as close as $z/a = .000125$ to the free surface. Increase in Poisson's ratio reduces K_I value at the vertex for Mode-I problem and increases K_{II} for Mode-II problem. This trend is similar to Benthem's results [82] where stress singularity became weaker for Mode-I and stronger for Mode-II with increase in Poisson's ratio.

For curved crack fronts with non-normal intersection with free surface, K_I values at crack vertex are higher than mid-surface K_I values for crack intersection angle of 101° and higher than those of inner layers for intersection angles of 105° and above. Bazant and Estenssoro [2] had also estimated critical angle to be 101° for $\nu = 0.3$ using a finite element technique.

The value of SIF at the crack vertex, computed from crack-vertex traction, is seen to be mesh dependent. But SIF value reflects the influence of the exponent of singularity existing at the crack vertex. A lower value of SIF is computed for a weaker singularity at the vertex and a higher value of SIF is computed for a stronger singularity at the vertex. For the same level of mesh refinement, value of SIF is seen to be sensitive to change in singularity of stresses at the vertex brought about by changes in either Poisson's ratio of the material or intersection angle of the crack front with the free surface. It is possible to estimate the intersection angle at which the SIF at the crack vertex is equal to or higher than SIF of inner layers. So the intersection angle at which free surface vertex point becomes critical along with other parts of the crack front is estimated.

Burton *et al.* [4] surmised that the underlying theoretical assumptions and developments in LEFM were to a degree incapable of explaining all of the various phenomena actually present in retardation of crack front near the free surface. Bakker [18] mentioned the need of invoking plasticity and crack closure effects to explain free surface retardation. On the other hand, for quasi-brittle behaviour with only small-scale yielding, Smith [19] found that cracks identical in shape to those in fatigued metal models could be grown under monotonic loads (R = ratio of minimum K_I to maximum $K_I = 1.0$) in photoelastic bodies suggesting that closure effects might not strongly affect crack shapes.

The present study shows that the critical angle of intersection predicted by Bazant and

Estenssoro [2] for a half-space problem is also achievable by analysis of finite specimens using BEM. So this study removes the doubt that LEFM cannot explain 101° angle as critical angle of intersection for a Mode-I finite specimen. The presented approach may help in predicting crack growth profiles accurately for problems where crack front penetrates free surface.

Table 3.1: Mesh characteristics for Mode-I runs with straight crack front.

Mesh no.	crack front element size ($\Delta l/a$)	free surface element size ($\Delta z/a$)	size of regular elements (size/clear distance to crack front) (on face having crack)	No. of elements	No. of nodes
1	0.1	0.1	0.5	408	1256
2	0.1	0.008	0.5	620	1906
3	0.05	0.048	0.25	1182	3642
4	0.05	0.008	0.25	1075	3317
5	0.05	0.0008	0.25	1239	3821

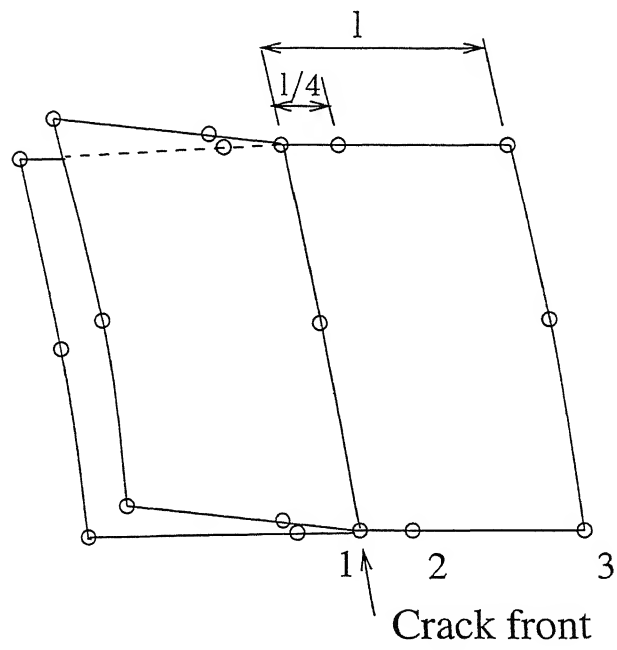


Figure 3.1: Crack front elements.

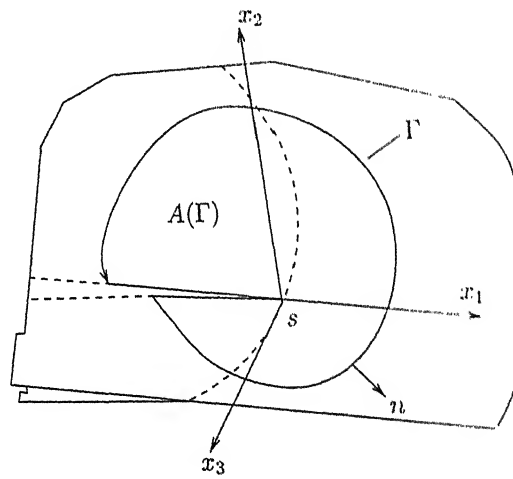


Figure 3.2: Contour and area surface for J_1^n .

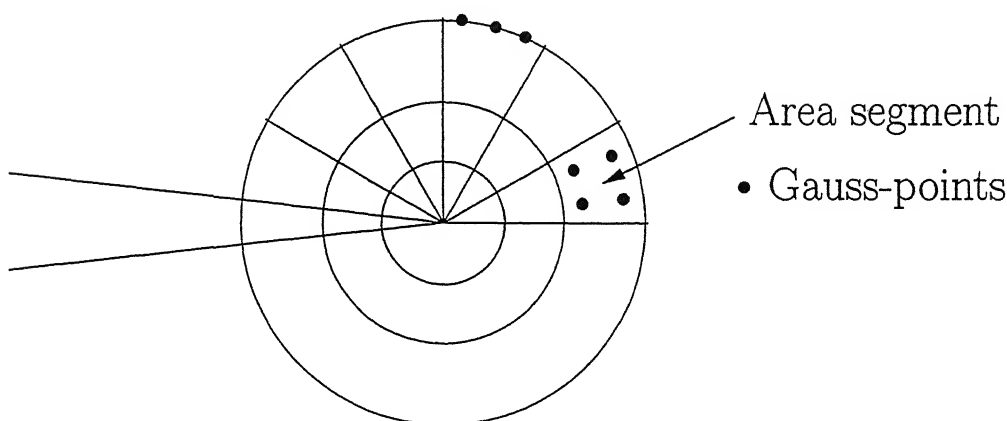


Figure 3.3: Distribution of internal points about the crack plane for J_1^n calculation.

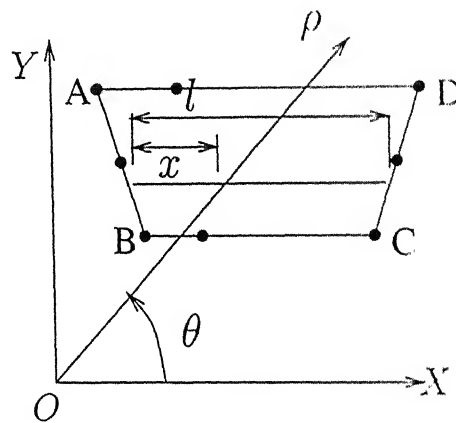


Figure 3.4: Quarter-point element projected in the plane tangent to the nearest node.

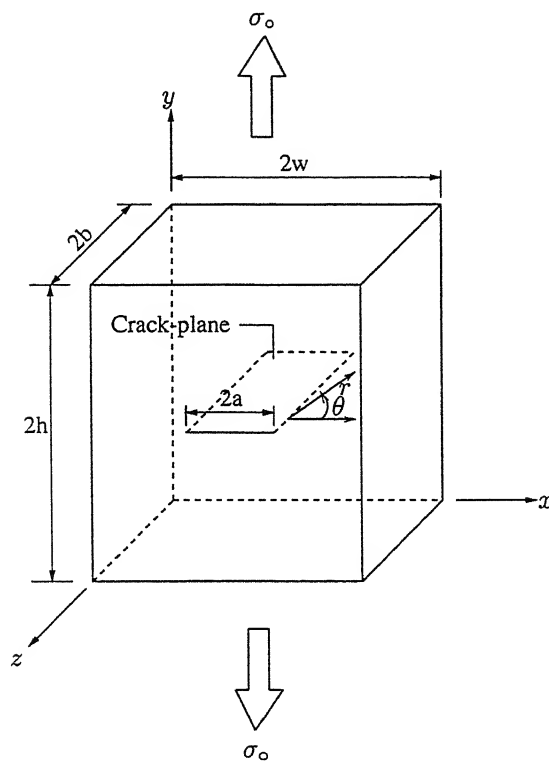


Figure 3.5: Center-crack tension specimen.

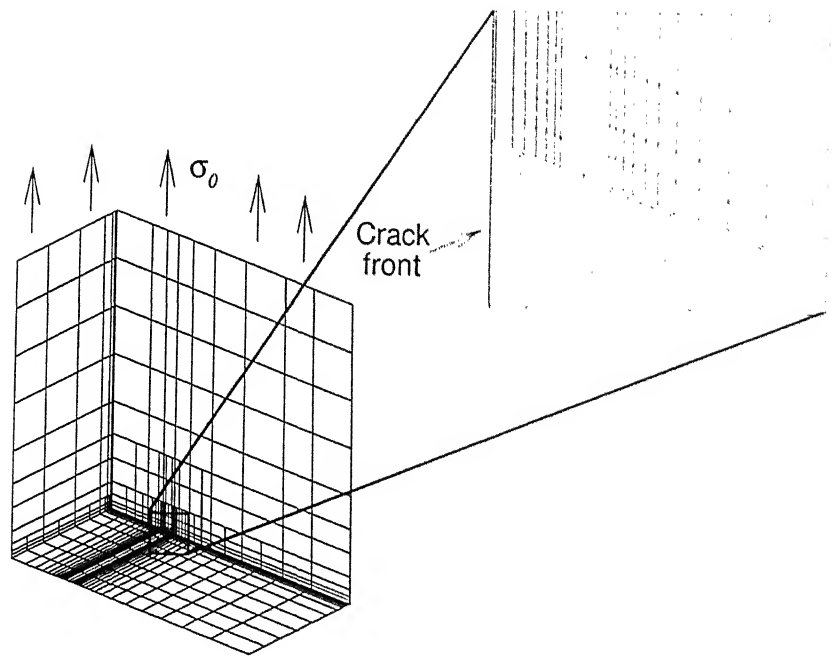


Figure 3.6: Boundary Element Mesh.

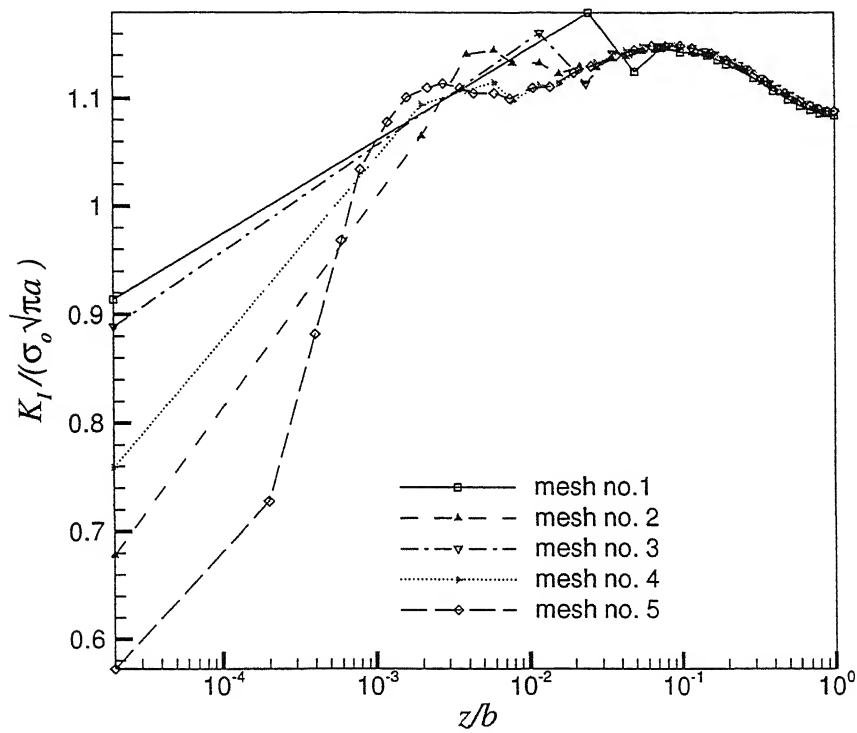


Figure 3.7: SIF distribution along crack front for different meshes (Table 3.1).

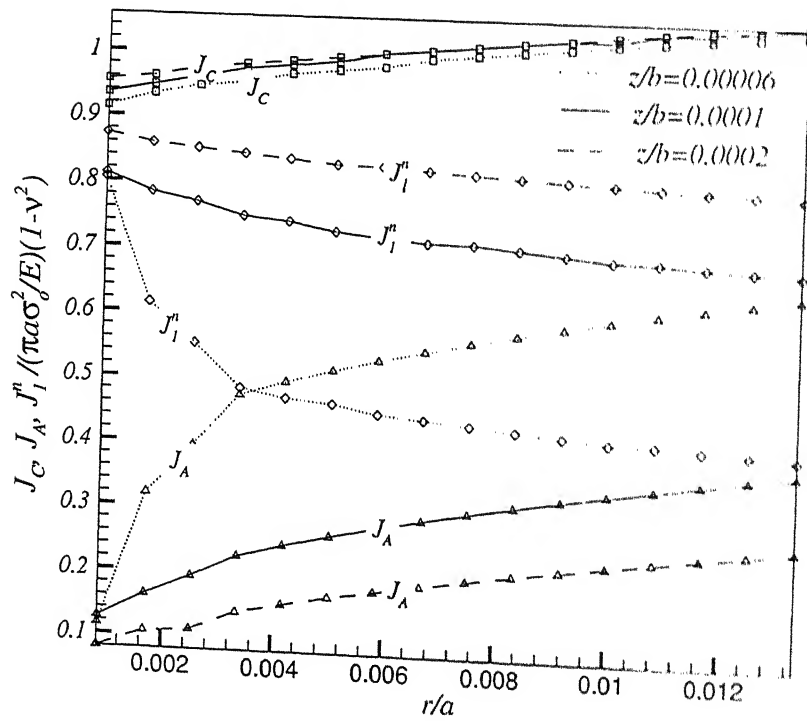


Figure 3.8: Variation of J_C , J_A and J_I^n with radial distance of contour from crack front.

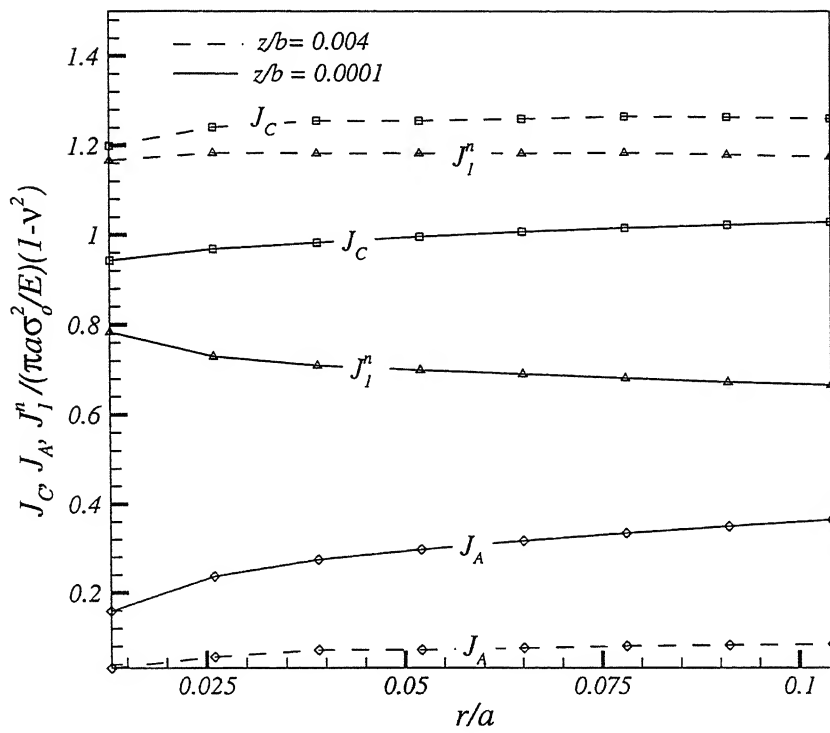


Figure 3.9: Variation of J_C , J_A and J_I^n with radial distance of contour from crack front.

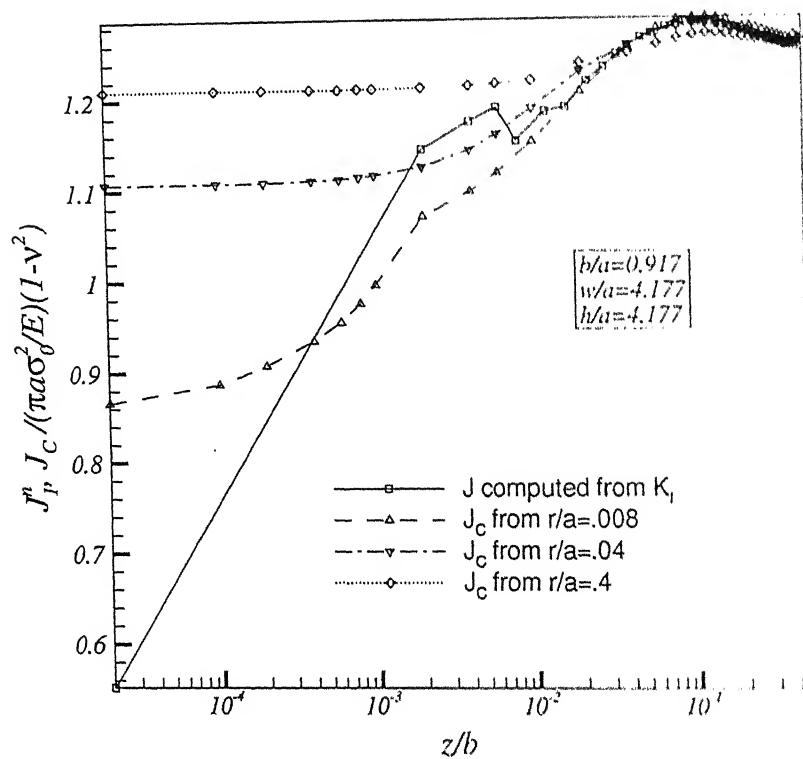


Figure 3.10: Variation of J_C along crack front for different radial contours.

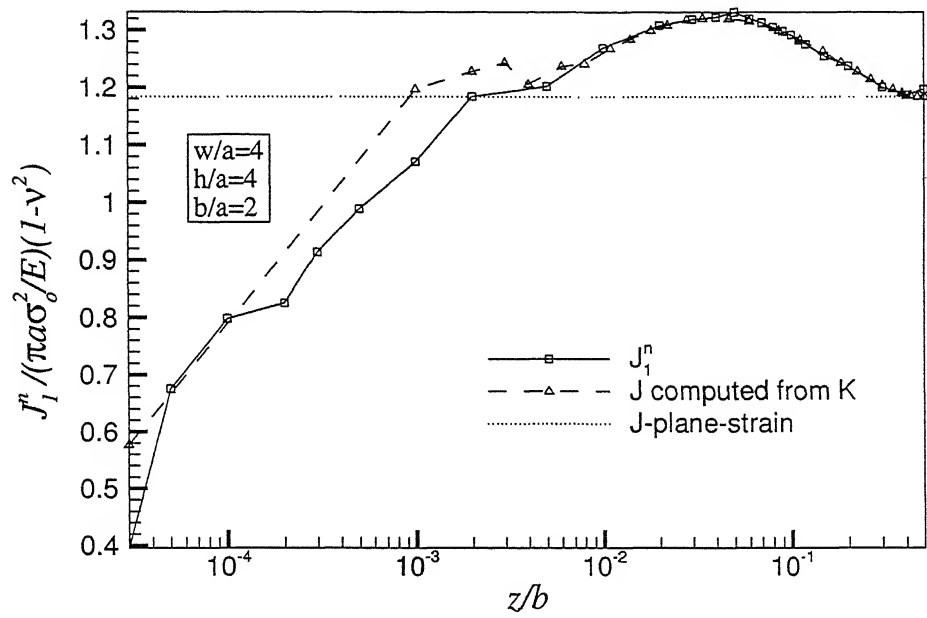


Figure 3.11: Variation of J_1^n along crack front.

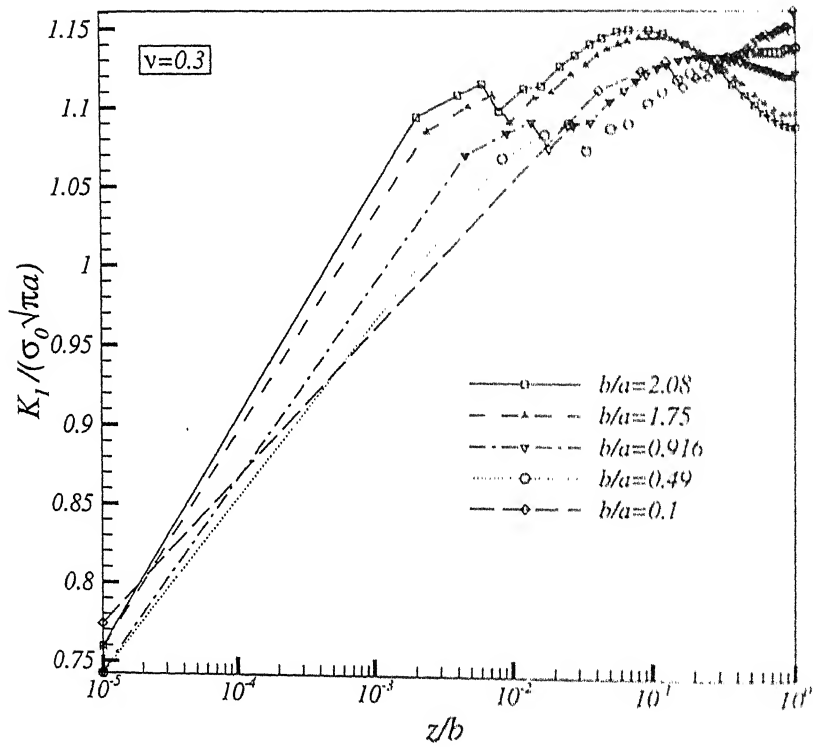


Figure 3.12: Variation of K_I along crack front for different thicknesses of specimen for normal intersection.

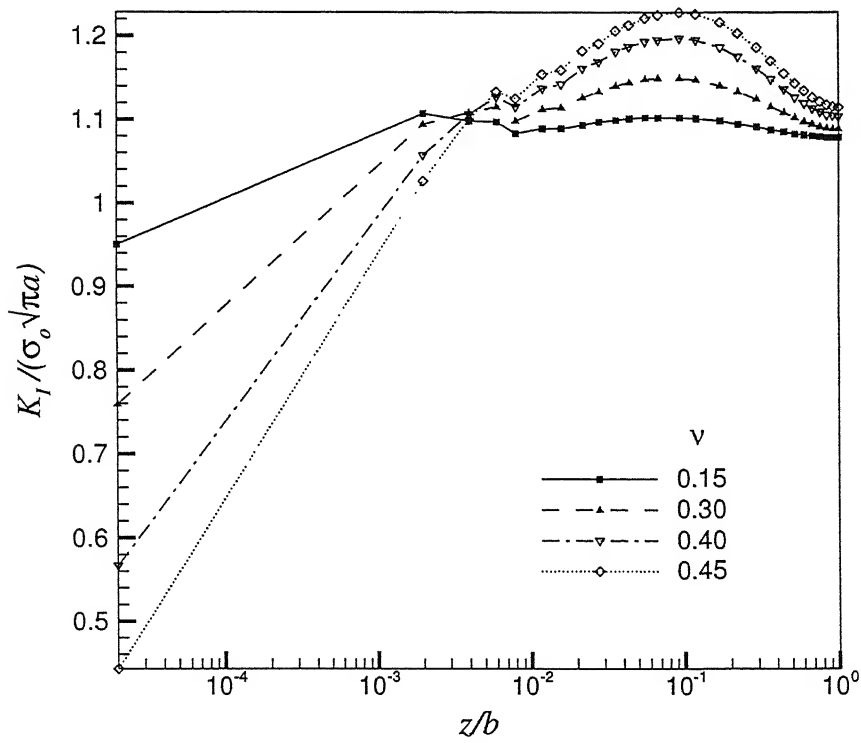


Figure 3.13: Variation of K_I along crack front for different Poisson's ratios for normal intersection.

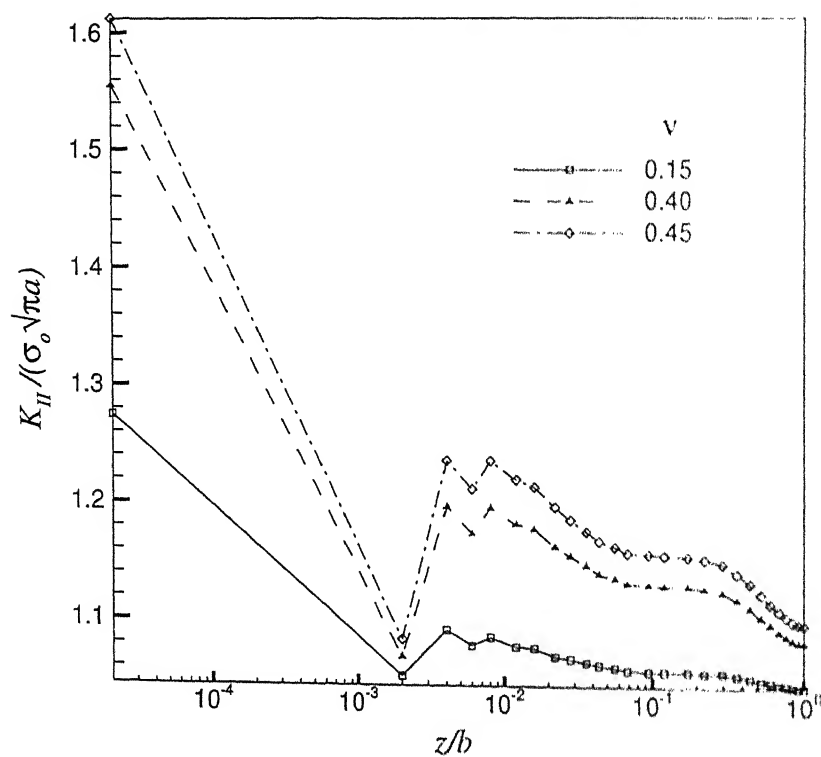


Figure 3.14: Variation of K_{II} along crack front for different Poisson's ratios for normal intersection.

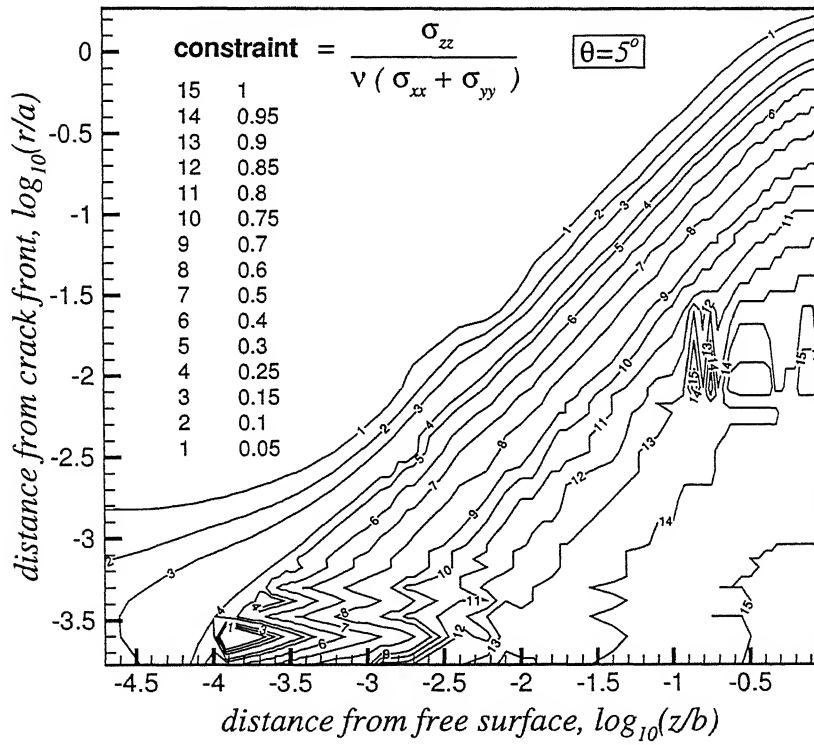


Figure 3.15: Contours of plane strain constraint for the thick plate ($b/a = 2.166$).

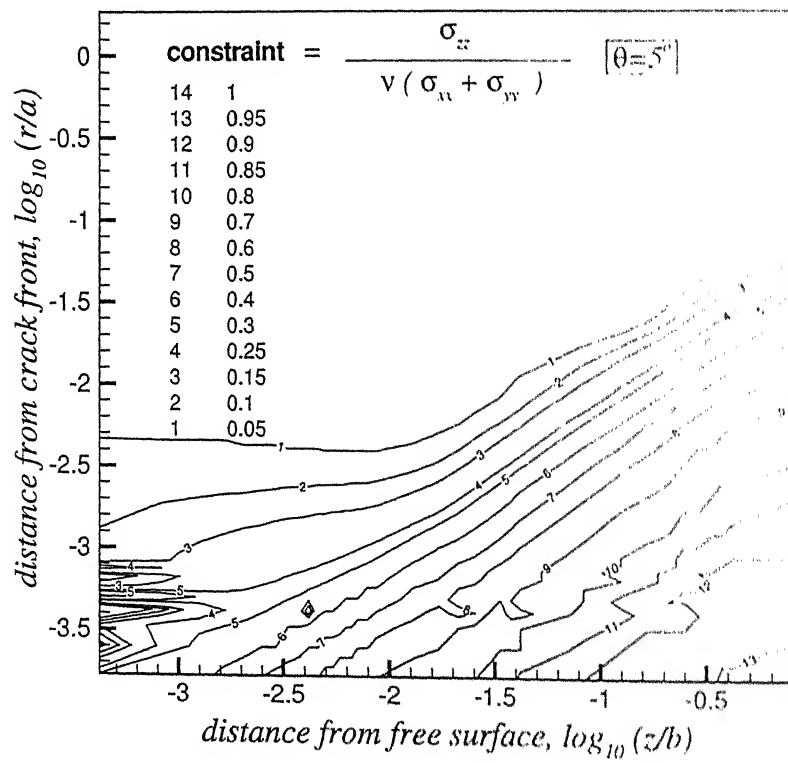


Figure 3.16: Contours of plane strain constraint for the thin plate ($b/a = .091$).

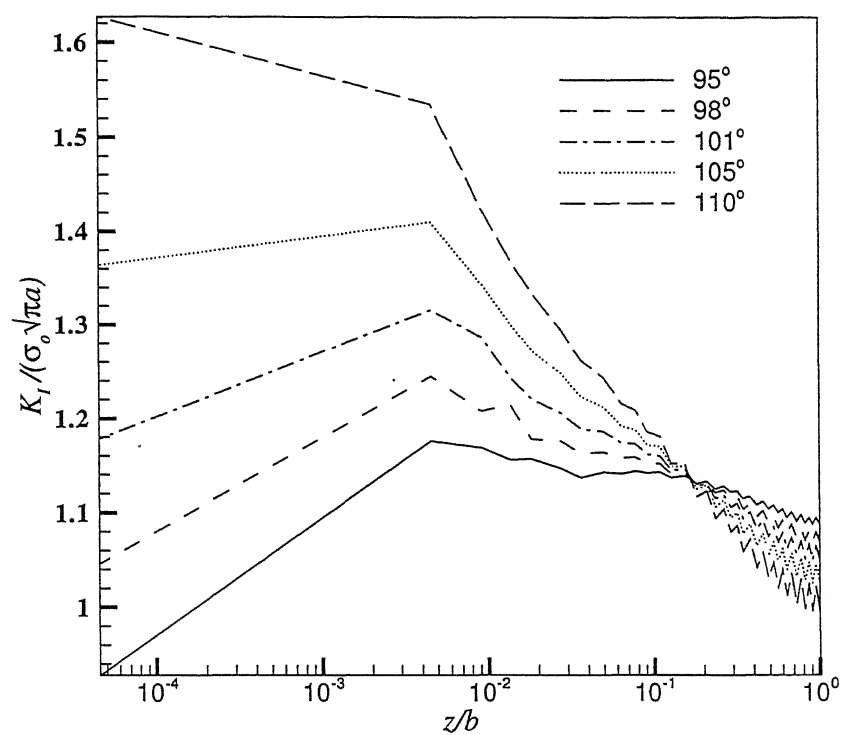


Figure 3.17: Variation of K_I along crack front for different intersection angles of crack front with free surface.

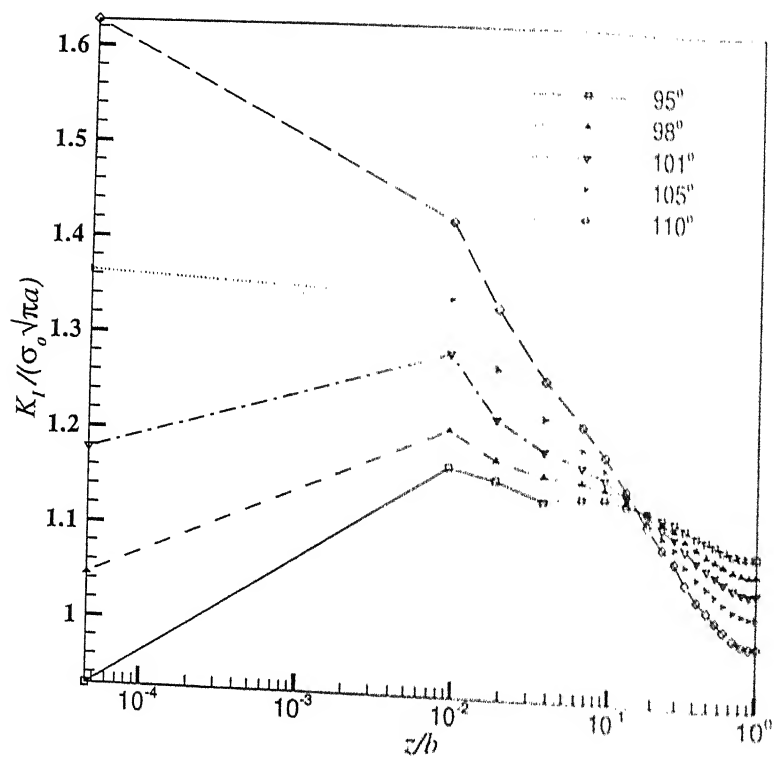


Figure 3.18: Variation of K_I along crack front for different intersection angles, using only corner node SIF values.

Chapter 4

Dynamic Analysis: Stationary Crack

This chapter deals with the implementation of a three-dimensional time-domain boundary integral formulation for a center-crack, finite solid under symmetrically applied step loading. The BEM displacement time domain formulations have, hitherto, been limited to analyzing two-dimensional crack problems, though hypersingular formulations have been used to analyze finite cracks in infinite domains. In this chapter, variation of dynamic stress intensity factor (DSIF) along the crack front for a stationary, through-thickness straight crack is studied for a finite solid under step loading. The state of stress is evaluated at the crack vertex, where crack front meets the free surface. The effect of free surface on DSIF is investigated. The effect of waves travelling in thickness direction is explained. It is possible to estimate accurately the critical intersection angle of the crack front with the free surface at which square-root singularity is restored at the crack vertex under step loading. A new partitioning scheme is proposed for spatial integration of elastodynamic kernels.

4.1 Introduction

While 2-D time domain boundary element formulations have received a lot of attention in recent years, 3-D time domain boundary element formulations have seen only limited applications. The reason is that time-domain boundary element algorithms become expensive for calculating response over large periods of time as information from earlier times must be used. The computational time and memory requirement become very large for 3-D problems.

Two different time-domain integral equation formulations are popular for the application of BEM for fracture problems. One is the conventional formulation where the integral representation of the boundary displacements is discretized. The second one is the hyper-

singular formulation where integral representations for both displacements and tractions are discretized. Hypersingular formulations have been used to analyze finite plane cracks in 3-D infinite domains [83,84]. Laplace transform BEM has also been used to analyze cracks in finite solids under dynamic loading [85]. Wen, Aliabadi and Rooke [86,87] presented a Laplace transform displacement discontinuity and fictitious stress formulations for 2-D and 3-D problems. They determined the stress intensity factors for several 2-D and 3-D problems using an equivalent stress approach. Domínguez and Gallego [60] used the direct time domain boundary element formulation in combination with the traction-singular quarter-point elements that had been used by Martínez and Domínguez [73] and Chirino and Domínguez [88] for static and time-harmonic computations, respectively. Time domain formulation is advantageous where an accurate solution is required from the very beginning and is the best possible approach for problems with time-dependent geometry [50]. For this study, direct time-domain approach is chosen so that the approach used to study free surface effect for a stationary crack can be easily extended to study free surface effect for a running crack in a finite solid. There are certain disadvantages associated with other approaches. In frequency domain analysis, internal damping reduces the maximum value reached by the SIF as a small amount of internal damping is required in frequency domain analysis to avoid spurious oscillations. In the Laplace transform approach, the solution has to be obtained for a certain minimum number of Laplace transform parameter values in order to obtain the inverted solution in the real time domain. In the case of moving boundary problems as in crack propagation, calculations for a set of transform parameters will need to be performed for each boundary configuration, thus, increasing the computational cost. Though the dual reciprocity approach requires less computer time, it does not reproduce very well the quick changes that SIF may have along time [89].

In the present work, the standard 3-D time-domain boundary integral formulation is implemented for a center-crack, finite solid under symmetrically applied loading. Variation of DSIF is studied along the crack front for the through-thickness crack. In this work, a new partitioning scheme is proposed and implemented for spatial integration of elastodynamic kernels. Algorithm for calculating principal value integrals suggested by Guiggiani and Gigante [7] is extended to elastodynamic analysis. Also, combination of projection technique with semi-analytical integration, used for nearly singular integrals for static problems by Cruse and Aithal [8] and Mi and Aliabadi [9], is extended to elastodynamic problems.

A crack front intersecting the free surface in a 3-D body has been a subject of interest for last three decades. Through-thickness fatigue cracks in plate geometries almost always

show crack front tunnelling, i.e., a curved crack front with the deepest point of the crack at the center. Benthem [1] analyzed a problem of a quarter-plane crack in a semi-infinite half-space subjected to symmetric quasi-static loading. For a crack front normal to the free surface, he derived that at the corner point, stresses have $r^{-.452}$ singularity for Poisson's ratio (ν) of 0.3. By a local finite element analysis, Bažant and Estenssoro [2] estimated the critical intersection angle to be 101° (for $\nu = 0.3$) for a stationary crack under elastostatic loading. By a finite element formulation similar to that used by Bažant and Estenssoro [2], Gudmundson and Östlund [3] found that a weaker singularity also exists at the corner point for a dynamically growing crack and estimated the critical angle to be 101° , almost independent of the crack-tip velocity. The success enjoyed by these local numerical analyses is not found to the same extent in finite element treatments of more global or complete problems which contain crack/surface intersections. Different predictions were made concerning the variation in energy release rate (G) with some results showing an increase in G in the free surface region, some a decrease and still others no change. Burton *et al.* [4] generated critical crack profiles using FEM with each profile having less than 2% numerical variation in G with depth. The crack profiles generated by them were significantly less curved than those observed in practice [5]. Thus in global situation, finite element analysis is not able to obtain an accurate stress state adjacent to the crack tip in the region close to the free surface, especially for cracks which are not normal to the surface. Using FEM for analysis, Lin and Smith [6] found that slightly non-orthogonal intersection caused a great loss of path-independence in the value of J -integral up to 47% near the free surface. Agrawal and Kishore [90] demonstrated the effectiveness of BEM in evaluating the state of stress at crack vertex and estimating critical intersection angle accurately for quasi-static loading. They achieved a close correspondence all along the crack front between J_1^n and K_I computed from the tractions at the nodes on the crack front. In a review article, Nishioka [91] has reported from an FEM analysis that value of the dynamic J -integral reduces near the free surfaces of the plate for a through-thickness straight crack. But author is not aware of any work in which critical intersection angle has been estimated for impact loading for a finite solid.

The present work uses boundary element method to study the effect of free surface on stress intensity factor distribution along the crack front for a stationary through-thickness crack in a finite solid under step loading. SIFs can be computed along the crack front from nodal values of traction in boundary element analysis [60]. Straight as well as curved crack profiles are studied. Critical intersection angle of crack front with free surface computed

in this work for Mode-I step loading for a finite solid matches closely with the value of critical angle predicted by Bažant and Estenssoro [2] for elastostatic loading for a half-space problem.

4.2 Transient Boundary Integral Formulation

Consider a homogeneous, isotropic and linearly elastic body of volume V bounded by a regular surface S , with its mass density ρ and dilatational and shear wave speeds as c_1 and c_2 respectively. Using Stoke's state of quiescent past corresponding to a point load with a Dirac delta function variation, Love's integral representation can be derived using Betti's reciprocal theorem. For zero initial conditions and zero body forces, the displacement of a point \mathbf{y} at time T can be represented by the following boundary integral equation:

$$C_{ij}(\mathbf{y})u_i(\mathbf{y}, T) = \int_S [G_{ij}(\mathbf{x}, \mathbf{y}, T) * t_i(\mathbf{x}, T) - H_{ij}(\mathbf{x}, \mathbf{y}, T) * u_i(\mathbf{x}, T)] dS(\mathbf{x}) \quad (4.1)$$

where

$$G_{ij} * t_i = \int_0^T G_{ij}(\mathbf{x}, T; \mathbf{y}, \tau) t_i(\mathbf{x}, \tau) d\tau \quad (4.2)$$

$$H_{ij} * u_i = \int_0^T H_{ij}(\mathbf{x}, T; \mathbf{y}, \tau) u_i(\mathbf{x}, \tau) d\tau \quad (4.3)$$

are Riemann convolution integrals. In the above, $u_i(\mathbf{x}, \tau)$ and $t_i(\mathbf{x}, \tau)$ are the displacement and traction components respectively at point \mathbf{x} and time τ . The free-term tensor C_{ij} is calculated by general close-form expression developed by Mantic [56]. The fundamental solutions G_{ij} and H_{ij} are displacements and tractions in direction i at a point \mathbf{x} at time T due to a unit impulse vector in direction j applied at a point \mathbf{y} at a preceding time τ . The fundamental solutions are given in explicit form as

$$G_{ij}(\mathbf{x}, T; \mathbf{y}, \tau) = \frac{1}{4\pi\rho} \left[(3a_{ij} - b_{ij}) \int_{1/c_1}^{1/c_2} \lambda \delta(v - \lambda r) d\lambda + a_{ij} \{ (1/c_1^2) \delta(v - r/c_1) - (1/c_2^2) \delta(v - r/c_2) \} + (b_{ij}/c_2^2) \delta(v - r/c_2) \right] \quad (4.4)$$

where $v = T - \tau$; $a_{ij} = h_i h_j / r^3$; $b_{ij} = \delta_{ij} / r$; $h_i = x_i - y_i$; r is the distance between points \mathbf{x} and \mathbf{y} . Also δ_{ij} is the Kronecker's delta and δ is the Dirac delta function.

$$H_{ij}(\mathbf{x}, T; \mathbf{y}, \tau) = \frac{1}{4\pi} \left[-6c_2^2 (5d_{ij} - e_{ij}) \int_{1/c_1}^{1/c_2} \lambda \delta(v - \lambda r) d\lambda + (12d_{ij} - 2c_{ij}) \{ \delta(v - r/c_2) - (c_2/c_1)^2 \delta(v - r/c_1) \} + 2r d_{ij} / c_2 \{ \dot{\delta}(v - r/c_2) - (c_2/c_1)^3 \dot{\delta}(v - r/c_1) \} \right]$$

$$\begin{aligned}
& - f_{ij}(1 - 2c_2^2/c_1^2)\{\delta(v - r/c_1) + (r/c_1)\dot{\delta}(v - r/c_1)\} - g_{ij}\{\delta(v - r/c_2) \\
& + (r/c_2)\dot{\delta}(v - r/c_2)\} \Big] \quad (4.5)
\end{aligned}$$

where $v \equiv T - \tau$; $h_i = x_i - y_i$; $d_{ij} = h_i h_j h_m n_m / r^5$; $f_{ij} = h_j n_i / r^3$; $g_{ij} = (h_i n_j + \delta_{ij} h_m n_m) / r^3$; $e_{ij} = f_{ij} + g_{ij}$. Also n_i are the components of outward pointing normal vector and $n_m h_m = n_1 h_1 + n_2 h_2 + n_3 h_3$.

4.3 Numerical implementation

The time-domain BEM in three-dimensions consists of two basic steps as explained in [49, 58, 59]:

1. A discretization of the real time axis into a sequence of equally spaced time intervals with the assumption of linear variation of displacement and constant variation of tractions over each time interval. When piecewise linear variation is used for both displacements and tractions, the time-stepping scheme becomes unstable [60, 61].
2. A discretization of boundary into 8-noded elements.

The time span of interest is divided into N equal time steps of size ΔT so that

$$T_n = n \Delta T, \quad n = 1, 2, \dots, N. \quad (4.6)$$

On the basis of these discretizations a time stepping solution of equation (4.1) can be established for the boundary displacements and tractions over each element and for each time step. The displacement boundary integral equation can be written as

$$C_{ij} u_i(\mathbf{y}, T_N) - \int_{T_{N-1}}^{T_N} \int_S [G_{ij} t_i - H_{ij} u_i] dS d\tau = \int_0^{T_{N-1}} \int_S [G_{ij} t_i - H_{ij} u_i] dS d\tau \quad (4.7)$$

where the integral on the right hand side is the contribution due to past dynamic history. This equation is also an exact statement since no approximation has yet been introduced. However, in order to solve the above equation, one has to approximate the time variation of the field quantities, in addition to the usual approximation of spatial variation. The time integration in the above equation is done analytically, and the spatial integration is done numerically. A system of algebraic equations is obtained at time step N through nodal collocation, i.e., by allowing \mathbf{y} to coincide sequentially with all the nodal points of the boundary.

4.3.1 Temporal and spatial interpolation of displacement and traction

The boundary variables are interpolated in terms of their values at nodes by

$$u_i(\mathbf{x}, \tau) = \sum_{n=1}^N [M_I^n u_i^{n-1}(\mathbf{x}) + M_F^n u_i^n(\mathbf{x})] \quad (4.8)$$

$$t_i(\mathbf{x}, \tau) = \sum_{n=1}^N [\mu_I^n t_i^{n-1}(\mathbf{x}) + \mu_F^n t_i^n(\mathbf{x})] \quad (4.9)$$

and

$$u_i^n(\mathbf{x}) = \sum_{c=1}^8 N^c[\xi(\mathbf{x})] u_i^{nc}, \quad i = 1, 2, 3 \quad (4.10)$$

$$u_i^{n-1}(\mathbf{x}) = \sum_{c=1}^8 N^c[\xi(\mathbf{x})] u_i^{(n-1)c}, \quad i = 1, 2, 3 \quad (4.11)$$

where u_i^{nc} and $u_i^{(n-1)c}$ represent nodal values of displacement at time nodes n and $(n-1)$ respectively. Similar interpolation is done for traction variables also. Here, N is the total number of time steps. M_I and M_F are the temporal interpolation functions, related to local time nodes I (initial) and F (final), and are of the following form for piece-wise linear variation:

$$M_I^n = \frac{T_n - \tau}{\Delta T} \phi_n(\tau) \quad (4.12)$$

$$M_F^n = \frac{\tau - T_{n-1}}{\Delta T} \phi_n(\tau) \quad (4.13)$$

where

$$\phi_n(\tau) = \begin{cases} 1 & \text{if } (n-1)\Delta T \leq \tau < n\Delta T \\ 0 & \text{otherwise} \end{cases}$$

or

$$\phi_n(\tau) = H(\tau - (n-1)\Delta T) - H(\tau - n\Delta T) \quad (4.14)$$

H being the Heaviside function.

The displacements are interpolated by piecewise linear functions. Traction are represented by piecewise constant functions which allow for sudden jump of their values from step to step. For tractions, temporal interpolation functions are of the form

$$\mu_I^n = 0.5 \phi_n(\tau) \quad (4.15)$$

$$\mu_F^n = 0.5 \phi_n(\tau) \quad (4.16)$$

For spatial interpolation of boundary variables, an approach [62] which combines the advantages of continuous and discontinuous elements in a single formulation is used in this work. In this formulation, expressions of the shape and interpolation functions are unified in a form suitable for fully continuous, fully discontinuous or transition elements (i.e., discontinuous only along one or more edges). Three types of boundary nodes are identified depending on the function they fulfil:

1. Geometrical nodes: those used for interpolating the boundary geometry.
2. Interpolation nodes: the points on the boundary which define the interpolation of the variables. The system nodal values correspond to these nodes.
3. Collocation nodes: where the boundary integral equation is enforced.

One property of the boundary element formulations is that the discontinuities of the variable across the element edges do not invalidate the convergence of the technique [63]. Collocation and interpolation nodes for continuous elements coincide with the geometrical nodes. Collocation nodes and interpolation nodes for discontinuous elements and discontinuous side of transition elements are situated inside the element. For quarter-point element, geometrical and interpolation nodes coincide, but collocation corresponding to nodes on crack front is done at nodes situated inside the elements on either side of the crack front. To reduce the number of equations and enhance accuracy, equations corresponding to collocation nodes before and after a given interpolation node are added up [64].

4.3.2 Analytical integration of temporal terms

The time integration in equation (4.7) after using equations (4.8) and (4.9) is done analytically and the spatial integration is performed numerically. Explicit expressions for time integrals may be found in [49, 58]. Temporal integration boils down to integration of terms like $\int_0^{\Delta T} \delta(T - \tau - r/c) M_I^1(\tau) d\tau$, $\int_0^{\Delta T} \int_{1/c_1}^{1/c_2} \lambda \delta(T - \tau - \lambda r) M_I^1(\tau) d\lambda d\tau$ etc.

For example,

$$\int_0^{\Delta T} \delta(T - \tau - r/c) (1 - \tau/\Delta T) \phi_1(\tau) (\tau) d\tau = \begin{cases} (1 - \frac{T}{\Delta T}) + \frac{1}{c\Delta T} r & \text{if } c(T - \Delta T) < r < cT \\ 0 & \text{otherwise} \end{cases} \quad (4.17)$$

Similarly, all temporal terms can be expressed in the form $a + br + \frac{d}{r^2}$ after analytical integration in time. Also a, b, d are constant in the separate zones defined in section 4.3.3. It is noticed that for the distance reached by both shear and compression waves travelling

from a source node up to a time ΔT , coefficient of $\frac{1}{r^2}$ is zero. Thus, the temporal terms are not adding to the singularity in r . Here, c is compression (c_1) or shear (c_2) wave speed.

4.3.3 Details of spatial integration

The kernels in elastodynamic case have discontinuous derivatives at points such that $r/c_{1(2)} = k\Delta T$ (k integer). Therefore, the standard numerical methods, like Gaussian integration, give poor results if applied over the whole element, say, E_i . Instead one has to partition each element E_i into sub-elements $E_i^k : E_i = \cup E_i^k$ with $E_i^k = \{(k-1)\Delta T < r/c < k\Delta T\}$. Then, an integral over E_i is the sum of sub-integrals over E_i^k , each sub-integral being evaluated using standard numerical methods. This technical difficulty is common to all BEM development using retarded potentials and time-marching schemes. It is reasonably tractable for 2-D problems. The partitioning is clearly a purely geometrical problem (find the intersection points of a given curve C with circles centered at a given point y and of equally spaced radii). On the contrary, its three-dimensional equivalent (find the intersection curves of a given surface S with spheres centered at a given point y and of equally spaced radii) is extremely complicated. However, Karabalis [59] had performed the spatial integrations by partitioning the receiver elements into very small rectangular sub-elements. With his scheme, the possibility of only certain portions of the source element being 'active' also could be taken into consideration.

In this work, a new scheme is proposed for partitioning of surface elements for 3-D problems as follows.

Partitioning scheme

Consider a boundary element S_p . It is mapped onto a square region R (Fig. 4.1) in the parameter plane having local intrinsic coordinates $\xi = (\xi_1, \xi_2)$. Suppose source point is y and a typical receiver point is x . Hence, a typical integral over the element S_p can be written as

$$\begin{aligned}
 I &= \int_{S_p} \int_0^T [V_{ij}(x(\xi), T; y, \tau) N^c(\xi, x) M(\tau) d\tau] dS(x) \\
 &= \int_{S_p} \left[\int_0^T V_{ij}(x(\xi), T; y, \tau) M(\tau) d\tau \right] N^c(\xi, x) dS(x) \\
 &= \int_R \int_0^T [V_{ij}(x(\xi), T; y, \tau) M(\tau) d\tau] N^c(\xi) J(\xi) d\xi_1 d\xi_2
 \end{aligned} \tag{4.18}$$

where V_{ij} is displacement or traction kernel, $M(\tau)$ is temporal interpolation function, and $N^c(\xi, \mathbf{x})$ are spatial interpolation functions of field variables.

Coordinates of a receiver point on a boundary element are given by a parametric representation in terms of shape function $M^c(\xi_1, \xi_2)$ and nodal coordinates x_i^c .

$$x_i = \sum_c M^c(\xi_1, \xi_2) x_i^c, \quad i = 1, 2, 3 \quad (4.19)$$

Let us indicate by $\eta = (\eta_1, \eta_2)$, the image of the point z on the element. Point z is closest to the source point. The first, second and third order derivatives are obtained by

$$\frac{\partial x_i}{\partial \xi_k} = \frac{\partial M^c}{\partial \xi_k} x_i^c \quad (4.20)$$

$$\frac{\partial^2 x_i}{\partial \xi_k^2} = \frac{\partial^2 M^c}{\partial \xi_k^2} x_i^c \quad (4.21)$$

$$\frac{\partial^3 x_i}{\partial \xi_k^3} = \frac{\partial^3 M^c}{\partial \xi_k^3} x_i^c \quad (4.22)$$

By employing a Taylor expansion about the closest point, it is easy to establish formula of the form

$$\begin{aligned} x_i = z_i &+ \left[\frac{\partial x_i}{\partial \xi_1} \Big|_{\xi=\eta} (\xi_1 - \eta_1) + \frac{\partial x_i}{\partial \xi_2} \Big|_{\xi=\eta} (\xi_2 - \eta_2) \right] \\ &+ \left[\frac{\partial^2 x_i}{\partial \xi_1^2} \Big|_{\xi=\eta} \frac{(\xi_1 - \eta_1)^2}{2} + \frac{\partial^2 x_i}{\partial \xi_1 \partial \xi_2} \Big|_{\xi=\eta} (\xi_1 - \eta_1)(\xi_2 - \eta_2) + \frac{\partial^2 x_i}{\partial \xi_2^2} \Big|_{\xi=\eta} \frac{(\xi_2 - \eta_2)^2}{2} \right] \\ &+ \left[\frac{1}{2} (\xi_1 - \eta_1)^2 (\xi_2 - \eta_2) \frac{\partial^3 x_i}{\partial \xi_1^2 \partial \xi_2} \Big|_{\xi=\eta} + \frac{1}{2} (\xi_1 - \eta_1) (\xi_2 - \eta_2)^2 \frac{\partial^3 x_i}{\partial \xi_1 \partial \xi_2^2} \Big|_{\xi=\eta} \right] \end{aligned} \quad (4.23)$$

Since geometry is interpolated with help of quadratic functions, above formula is exact. The terms $\frac{\partial^3 x_i}{\partial \xi_1^3}$ and $\frac{\partial^3 x_i}{\partial \xi_2^3}$ do not appear in the above expression as these are equal to zero due to quadratic interpolation of the geometry.

Following a common practice in the BEM, polar coordinates (ρ, θ) centered at η are defined in the parameter plane as

$$\xi_1 = \eta_1 + \rho \cos \theta \quad (4.24)$$

$$\xi_2 = \eta_2 + \rho \sin \theta \quad (4.25)$$

so that $d\xi_1 d\xi_2 = \rho d\rho d\theta$. Hence,

$$x_i - y_i = e_i + \rho \left[\frac{\partial x_i}{\partial \xi_1} \cos \theta + \frac{\partial x_i}{\partial \xi_2} \sin \theta \right]$$

$$\begin{aligned}
& + \rho^2 \left[\frac{\partial^2 x_i \cos^2 \theta}{\partial \xi_1^2} + \frac{\partial^2 x_i}{\partial \xi_1 \partial \xi_2} \cos \theta \sin \theta + \frac{\partial^2 x_i \sin^2 \theta}{\partial \xi_2^2} \right] \\
& + \rho^3 \left[\frac{1}{2} \cos^2 \theta \sin \theta \frac{\partial^3 x_i}{\partial \xi_1^2 \partial \xi_2} + \frac{1}{2} \cos \theta \sin^2 \theta \frac{\partial^3 x_i}{\partial \xi_1 \partial \xi_2^2} \right] \\
& = e_i + \rho A_i(\theta) + \rho^2 B_i(\theta) + \rho^3 C_i(\theta)
\end{aligned} \tag{4.26}$$

where $e_i = z_i - y_i$. Hence,

$$\begin{aligned}
r^2 &= \Sigma (x_i - y_i)^2 \\
&= \Sigma e_i^2 + 2\rho \Sigma (A_i(\theta) e_i) + \rho^2 (\Sigma A_i^2(\theta) + 2\Sigma (e_i B_i(\theta))) + 2\rho^3 (\Sigma A_i(\theta) B_i(\theta) + \Sigma (e_i C_i(\theta))) \\
&\quad + \rho^4 (2\Sigma (A_i(\theta) C_i(\theta)) + \Sigma B_i^2(\theta)) + 2\rho^5 \Sigma (B_i(\theta) C_i(\theta)) + \rho^6 \Sigma C_i^2(\theta)
\end{aligned} \tag{4.27}$$

For integration, the integration square ($-1 \leq \xi_i \leq 1$) is subdivided into triangles with common vertex at $\eta = (\eta_1, \eta_2)$. The integral (4.18) of a typical kernel over each triangle is calculated as

$$I = \int_{\theta_1}^{\theta_2} \int_0^{\rho_{\max}} F_{ij}(\rho, \theta) d\rho d\theta \tag{4.28}$$

where

$$F_{ij}(\rho, \theta) = W_{ij}(\mathbf{y}, \mathbf{x}(\xi(\rho, \theta))) N^c(\xi(\rho, \theta)) \rho J(\xi(\rho, \theta)) \tag{4.29}$$

where $W_{ij} = \int_0^T V_{ij}(\mathbf{x}, T; \mathbf{y}, \tau) M(\tau) d\tau$. The limits θ_1 and θ_2 are angles subtended by the arms of the triangle on the vertex $\eta = (\eta_1, \eta_2)$. Here ρ_{\max} is the value of ρ on a particular ray making angle θ , where it meets the opposite side of the triangle.

First of all, Gauss integration is performed over θ direction. Corresponding to the value of θ computed as per Gauss points, ρ_{\max} is calculated for the particular ray. The values of ρ on a particular ray corresponding to the distance of $c_1 n \Delta T$ or $c_2 n \Delta T$ are computed by a combination of bisection and Newton-Raphson methods applied on equation (4.27). For each ray, the value of ρ are found corresponding to positions of heads and tails of the wavefronts of compression and shear waves, starting from the source node, for the element and time interval under consideration. The ray is divided into three different zones for separate Gaussian integration. The three different zones are:

1. both compression and shear wave cover part of the ray.
2. only compression wave covers part of the ray.
3. only shear wave travels that portion of the ray in that particular time interval.

In a time interval, only those areas contribute to the integral which were not affected by the particular waves in previous time intervals. Thus, jump in the kernels at points such that $r = c_{1(2)} n \Delta T$ is handled accurately.

Evaluation of Principal-Value Integral

Principal value singularity occurs for traction kernel H_{ij} when source element becomes also a receiver. All temporal terms can be expressed in the form $a + br + \frac{d}{r^2}$ after analytical integration in time, as explained in section 4.3.2. Also a, b, d are constant in the respective zones defined in section 4.3.3, allowing use of techniques developed for integrating elastostatic kernels by splitting the radial integration over three separate zones.

The Cauchy principal value integral is treated in the same way, as done by Guiggiani and Gigante [7] for the elastostatic case. The non-linear transformation suggested by Doblaré and Gracia [66] is also incorporated.

Quasi-singular integration

Nearly-singular integrals need to be evaluated accurately. Algorithm proposed by Cruse and Aithal [8] and further extended to hypersingular kernel cases by Mi and Aliabadi [9] is applied to elastodynamic case. This algorithm is analogous to singularity subtraction technique. Nearest point on the element from collocation point is found by Newton-Raphson method. The element, over which integration is to be done, is projected on to the plane tangent at the closest node. In this method, boundary variables are expanded about the closest node. Integration is partially carried out in real space and partially in intrinsic space. Intrinsic space integration is fully numerical, while integration in real space, i.e., on projection of the element, is done semi-analytically in two stages: radial integration is done analytically and angular integration is done numerically. Angular variable transformation of Hayami [79] is used to weaken the angular near-singularity arising when collocation node is near the edge of an element. For traction-singular elements, integration of G matrix is performed using the procedure explained in [90].

4.3.4 Crack Elements

Quarter-point elements are used along the crack front and traction-singularity is incorporated in the quarter-point elements ahead of the crack front [71, 72]. The stress intensity factors can be computed directly by the boundary element code as follows:

$$\begin{aligned} K_I &= \bar{t}_2^1 \sqrt{2\pi l} \\ K_{II} &= \bar{t}_1^1 \sqrt{2\pi l} \\ K_{III} &= \bar{t}_3^1 \sqrt{2\pi l} \end{aligned} \tag{4.30}$$

where \bar{t}_i are the tractions (with square-root singularity embedded in them) at nodes on the crack front and l is the length of crack front elements in the direction of singularity. It may be noted that the use of traction nodal values of the singular element at the crack tip for SIF computation is substantially less sensitive to the discretization than any of the displacement correlation procedures [60].

4.4 Results and Discussion

Elastic analysis of a stationary crack subjected to symmetrically applied step load has been performed for this work. Fig. 4.2 shows the geometry of the center crack tension specimen and the loading used in numerical analysis. The specimen has the parameters: $a = 0.24$ cm, $w = 1$ cm, $h = 1$ cm and $b = 0.5$ cm where a is the crack half-length, w is specimen half-width, h is half-height and b is specimen half-thickness. The material is assumed to be linear elastic with properties as: shear modulus $\mu = 90$ GPa, Poisson's ratio $\nu = 0.3$ and density $\rho = 7800$ kg/m³. Hence, $c_1 = 6354$ m/s and $c_2 = 3396$ m/s. The center crack specimen is loaded by symmetrically applied tensile step pulses $\sigma(t) = \sigma_0 H(t)$ at $y = \pm h$ planes. This problem was solved by Chen [92] using finite differences as a plane-strain 2-D problem and has been frequently used as a reference to validate other methods. In our chosen geometry, height of the specimen is half the height in Chen's specimen. This is done to reduce hard-disk storage requirement for the computational run on the refined mesh. Influence of three-dimensional effects on DSIF along the crack front is studied in the present work.

Due to the symmetry in the specimen geometry and loading, only one-eighth of the specimen is modelled in the boundary element analysis. Fig. 4.3 shows the boundary-element idealization of one-eighth of the center-crack specimen corresponding to mesh no. 4 (Table 4.1). Eight-node quadrilateral elements are used. A combination of continuous and discontinuous elements is used to reduce the overall degrees of freedom. The eight-node elements bordering the crack on the side of the crack surface are quarter-point elements, while the ones on the opposite side, i.e., ahead of the crack front are quarter-point, traction-singular elements. Triangular elements (collapsed eight-noded elements) are used to surround the intersection point of the crack front with the lateral facets. These triangular elements are modelled as quarter-point, traction-singular elements.

Appropriate boundary conditions are applied to the symmetry planes. This is done by restraining nodal displacements in the direction normal to the plane or planes of symmetry to which the node belongs. The nodes on the crack surface, except for those directly on

the crack front or on the edges with lateral facets, are left free to move in three orthogonal directions.

Table 4.1 shows details of some of the meshes with varying degrees of refinement. Runs were performed for convergence study of transient response for a straight through center crack under Mode-I step loading ($\sigma(t) = \sigma_o H(t)$). The profiles of dynamic stress intensity factor $K_I(t)$ are seen to converge across the thickness except for the free boundary layer region (Figs. 4.4, 4.5, 4.6). Fig. 4.6 shows variation of DSIF across the thickness for the time instant $tc_1/h = 3.177$. It is seen that mesh convergence in DSIF values is observed all along the crack front except for the crack vertex region. DSIFs are calculated from values of traction at the crack-tip nodes. The 3-D characteristics of the straight crack are studied using the mesh no. 4 (Table 4.1), which has 1994 nodes, 620 elements and 5982 degrees of freedom. The selected mesh has 12 layers of elements on the face having the crack. The thicknesses of different layers after normalization with half-crack length are .008,.008,.016,.024,.032,.048,.104,.12, .12,.12,.12 and .12 respectively. Various three-dimensional aspects of fracture characteristics of a through thickness center crack in a plate under step loading are enumerated as follows:

1. **Weaker singularity at the crack vertex for Mode-I loading:** For the position of crack vertex on the crack front, variation of normalized dynamic stress intensity factor ($K_I(t)/(\sigma_o\sqrt{\pi a})$) versus time (tc_1/h) is shown in Fig. 4.4. At the crack vertex, the stress singularity is known to be weaker than square-root. Hence stress intensity factor, defined as the strength of the square-root singularity at the crack tip, loses its significance at the corner point where crack front intersects the free surface. This is very well reflected by lack of convergence in value of DSIF at the vertex with increasing mesh refinement. At the free surface, DSIF is much lower for mesh no. 1 and 3 compared to mesh no. 2 as element layer adjoining the free surface is thinner in mesh no. 1 and 3. Value of DSIF at the crack vertex is sensitive to thickness of elements near the free surface. Thinner elements are needed close to free surface to estimate free surface effect accurately. Despite being mesh dependent, DSIF calculated from crack-tip tractions reflects the level of singularity at the crack vertex.

Value of DSIF at mid-surface are close to plane-strain values as obtained by Chen [92]. Peak value of 2.637 occurs at the mid-surface for the specimen having $b/w = 0.5$. Value of normalized SIF for quasi-static loading at the mid-surface for the same specimen is evaluated as 1.088 by boundary element analysis. Parton and Boriskovsky [33] mentioned a 2.45 fold increase in the DSIF value over the static value in the Mode-

I problem considered by Chen. A factor of 2.42 is observed in the present results for the considered geometry.

2. **Influence of von Schmidt wave produced by incoming longitudinal wave at the free surface near the crack vertex:** Variations and several local peaks in DSIF versus time curve caused by interaction of crack tip with Rayleigh wave, von Schmidt wave and reflected scattered waves for a two-dimensional plane strain Mode-I problem with step loading are well explained [93, 94]. The present three-dimensional analysis brings out the influence of waves travelling back and forth in the thickness direction. The same cannot be observed in a two-dimensional analysis. A von Schmidt wave is generated by the grazing incident longitudinal wave at the free surface near crack vertex. This wave propagates back and forth in the thickness direction influencing the value of DSIF along the crack front. Goodier and Bishop [95] and Roesler [96] showed the existence of a 'head wave' or von Schmidt wave trailing behind a P-wave, arising from reflection of a grazing-incident P-wave at a free boundary. Beinert [97] experimentally observed the splitting of a primary dilatational pulse into a train of equally spaced transverse pulses, when an elastic plate is loaded at its edge by a short-duration shock. Each of these transverse waves travels across the plate, with the velocity, c_2 , at an angle γ given by $\sin \gamma = c_2/c_1$.

Influence of the von Schmidt wave propagating back and forth in the thickness direction is noticeable by the mild fluctuations at regular time intervals of transit time a shear wave takes to travel the thickness of the specimen (Fig. 4.7). Fig. 4.8 shows that peak value of DSIF occurs at different positions along the crack front at different instants of time. At certain instants of time, peak value of DSIF is at mid-thickness position and other times peak DSIF position is shifted inside. This shows that the above described propagation of von Schmidt wave in thickness direction is causing mild variations in DSIF in the thickness direction.

Fig. 4.9 shows the variation of divergence and x_1 -component of curl of the displacement vector at an internal point ($x_1/w = 0.23, x_2/h = 0.01, x_3/b = 0.476$) with respect to time. Timings of the rise and fall in the curve of 'curl' seen in the figure imply the existence of a transverse wave travelling back and forth in thickness direction. But the plot of divergence does not exhibit any fluctuations corresponding to the times of rise and fall in the 'curl' curve, implying that neither Rayleigh wave nor dilatational wave is responsible for the mild fluctuations in values of DSIF in

thickness direction seen in Fig. 4.8. Only transverse waves travelling back and forth in thickness direction are responsible for these fluctuations.

3. **Effect of plate thickness on SIF:** Influence of the von Schmidt wave is further highlighted in Fig. 4.10 where mid-surface $K_I(t)$ is plotted for specimens of different thicknesses. Peak value of DSIF in this plot is 2.64 for $b/w = 0.5$, 2.41 for $b/w = 0.22$ and 2.18 for $b/w = 0.022$. So reduction in peak value of DSIF is observed on thinning of the specimen due to smearing effect of greater number of traverses of shear waves across the thickness of the specimen.
4. **Stronger singularity at the crack vertex for Pure Mode-II loading:** Plots of $K_{II}(t)$ are shown in Fig. 4.11 for different positions along the crack front for the problem of symmetrically applied shear step loading on the center crack specimen. It is seen that DSIF is higher at the crack vertex compared to any other position on the crack front. Benthem [82] had found by finite difference method that a stronger than square-root singularity exists at the point where crack front intersects the free surface for a normal intersection for Mode-II elastostatic loading. Peak value of normalized DSIF at mid-surface position is observed to be 3.38. Influence of stronger singularity is reflected in the higher value of DSIF obtained at the crack vertex. Thus the present analysis is able to assess both weaker and stronger singularity by DSIF value at the crack vertex being lower or higher than corresponding plane-strain values.
5. **Effects of crack tip tunnelling:** Through-thickness fatigue cracks in plate geometries almost always show crack front tunnelling, i.e., a curved crack front with the point of maximum length of the crack at the center. It is also observed that fatigue crack fronts penetrate the free surface at a non-zero angle with the normal to the free surface. Bažant and Estenssoro [2] argued that this angle is fixed by the angle at which the square-root singularity of stresses and strains at the free surface penetration is restored. They showed that the front edge of a planar Mode-I crack that propagates in an elastic isotropic plate in a plane normal to the plate surfaces must terminate at the surfaces with a certain angle β depending only on Poisson's ratio ν . Tests were carried out by Rolfe and Barsom [5] on structural steel in static loading according to E-399 ASTM Standard. Their test results showed that theoretical lines of inclination $\beta = 101^\circ$ with the plate surface agreed very well with the observed terminal directions of the first arrest marks, which corresponded to an essentially elastic fracture stage. Gudmundson and Östlund [3] found that a weaker

singularity exists at the corner point for a dynamically growing crack and estimated the critical angle to be 101° almost independent of crack velocity. These studies were conducted using a local analysis for quarter-plane crack in a semi-infinite half-space subjected to symmetric loading.

In the present study, calculations on tunnelling crack fronts are performed using circular crack fronts with different penetration angles, viz., 95° , 98° , 101° , 105° and 110° . The model selected for studying crack-tunnelling effect has 9 layers of elements of unequal thicknesses on face containing the crack. The model has 825 nodes and 262 elements and 2475 degrees of freedom. The thicknesses of different layers after normalization with half-crack length are .004, .004, .008, .016, .032, .064, .128, .256 and .358 respectively. The specimen has geometrical parameters: $a/w = 0.24$, $h/w = 1$, $b/w = 0.22$. Also in the present study, mesh is not orthogonal at the crack front, i.e., crack tip elements are not oriented normally to the crack front. The self-similar crack growth direction is taken as parallel to the free surface, rather than normal to the crack front. Burton *et al.* [4] also advanced crack front parallel to the free surface to produce a crack that retains its shape during propagation.

Fig. 4.12 shows a comparison of the calculated crack-vertex $K_I(t)$ -distributions for different penetration angles. It is seen that DSIF at crack vertex increases with increase in intersection angle. Values of $K_I(t)$ are calculated from crack tip tractions. The modelled crack front is not smooth but is made of small straight line segments. For correct interpolation of traction singularity in crack tip elements in BEM, a restriction is imposed on the positions of nodes in the elements requiring that element edge on the crack front be straight [81]. Fig. 4.13 shows the plots of $K_I(t)$ for different crack front intersection angles at the mid-surface. It is seen that free surface DSIF is greater than mid-surface DSIF for intersection angles of 101° and higher. At mid-surface, DSIF decreases with increase in intersection angle. For intersection angle of 101° , Fig. 4.14 shows that DSIF at crack vertex is higher than DSIF of inner layers implying that crack front has become critical at the corner point where crack front meets the free surface.

Runs are also made for curved crack fronts on a mesh as refined as mesh no. 4 (Table 4.1). Results from refined mesh (Fig. 4.15) show that free surface DSIF values are lower than mid-surface values for intersection angle of 98° and vice-versa is true for intersection angle of 101° . So value of critical intersection angle estimated by the boundary element analysis exhibits mesh-independence. Thus critical intersection

angle can be assessed accurately for finite domains with time-domain BEM.

4.5 Conclusions

1. Time-domain 3-D BEM is implemented for studying influence of free-surface on DSIF in a center-crack specimen under step loading. This work shows the efficacy of BEM and DSIF calculated from nodal traction values in studying three-dimensional aspects in crack/surface intersection problems for impact loading.
2. A new partitioning scheme is proposed and implemented for spatial integration for time-domain BEM.
3. Lower values of DSIF are found at corner point for Mode-I loading, confirming the existence of lower singularity in stress at corner point. The value of DSIF at the crack vertex, computed from crack-tip traction, is seen to be mesh dependent. But computed DSIF value reflects the influence of the exponent of singularity existing at the crack vertex. A lower value of DSIF is computed for a weaker singularity at the vertex and a higher value of DSIF is computed for a stronger singularity at the vertex. For the same level of mesh refinement, value of DSIF is seen to be sensitive to change in singularity of stresses at the vertex brought about by changes in intersection angle of the crack front with the free surface.
4. Von Schmidt waves, travelling back and forth in thickness direction, influence the variation of DSIF along the crack front. Peak DSIF values are seen to reduce with the reduction in thickness of the specimen.
5. It is possible to estimate the intersection angle at which the DSIF at the crack vertex is equal to or higher than DSIF of inner layers. So the intersection angle at which free surface vertex point becomes critical along with other parts of the crack front is estimated. Values of $K_I(t)$ at crack vertex are seen to be higher than values of $K_I(t)$ at inner layers for crack intersection angles of 101° and above, implying that crack has become critical at the vertex for intersection angle of 101° .

Table 4.1: Mesh characteristics for Mode-I runs with straight crack front.

Mesh no.	b/w	crack tip element size ($\Delta l/a$)	free surface element size ($\Delta z/a$)	size of regular elements (size/clear distance to crack-tip) (on face having crack)	No. of elements	time step $c_1 \Delta T/h$
1	.5	0.1	0.004	2.0	340	0.12708
2	.5	0.1	0.1	0.5	408	0.06354
3	.5	0.1	0.008	0.5	449	0.06354
4	.21	0.1	0.008	0.5	620	0.06354

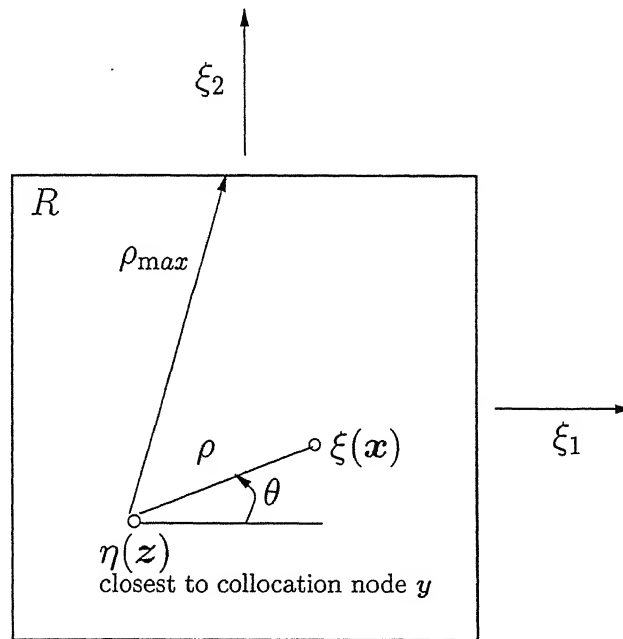


Figure 4.1: Image in the parameter plane and polar coordinates

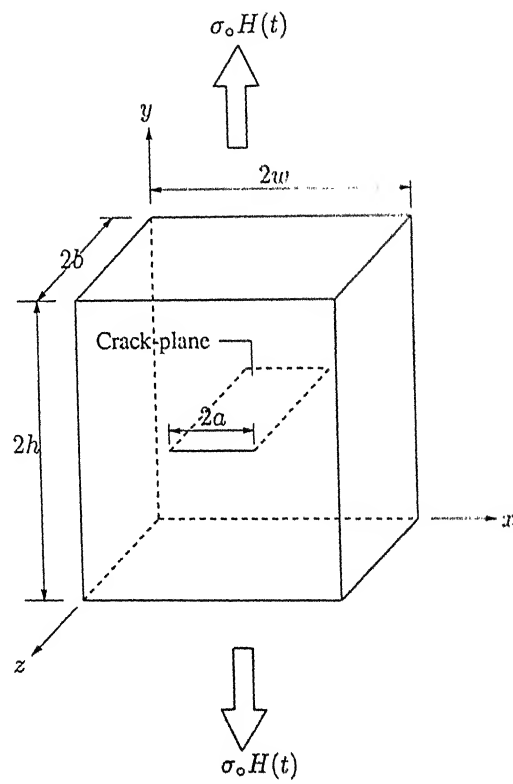


Figure 4.2: Center-crack tension specimen

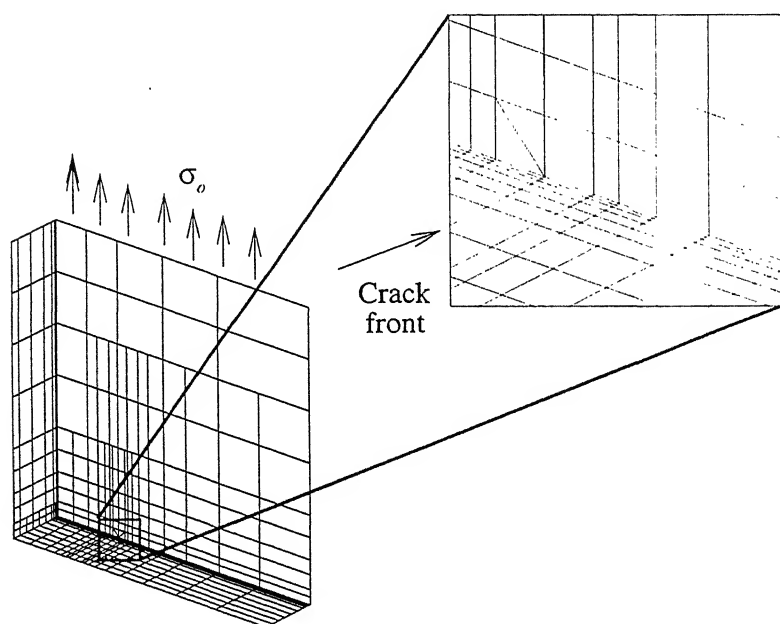


Figure 4.3: Boundary Element Mesh

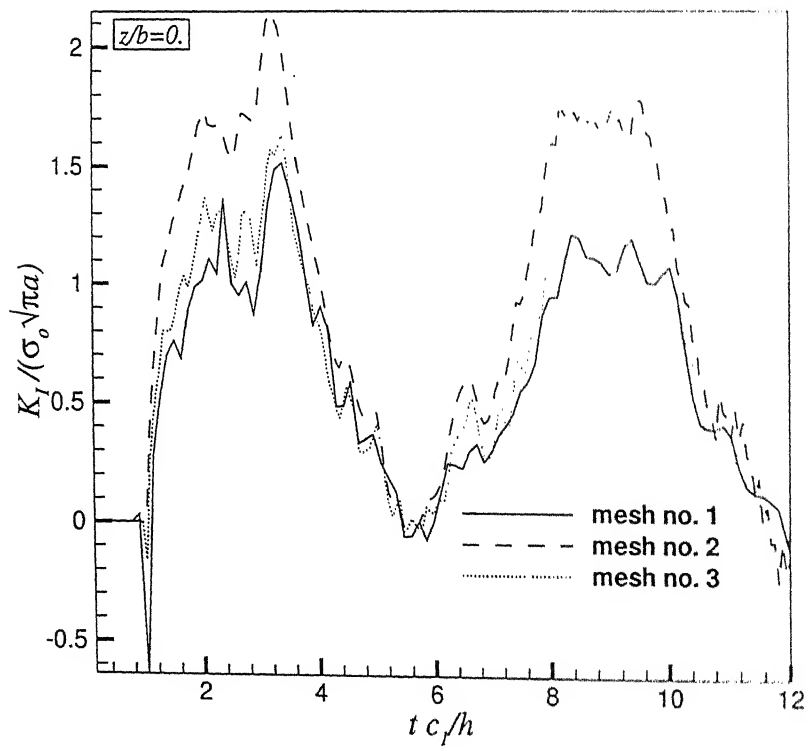


Figure 4.4: DSIF variation with time at crack vertex for different meshes (Table 4.1)

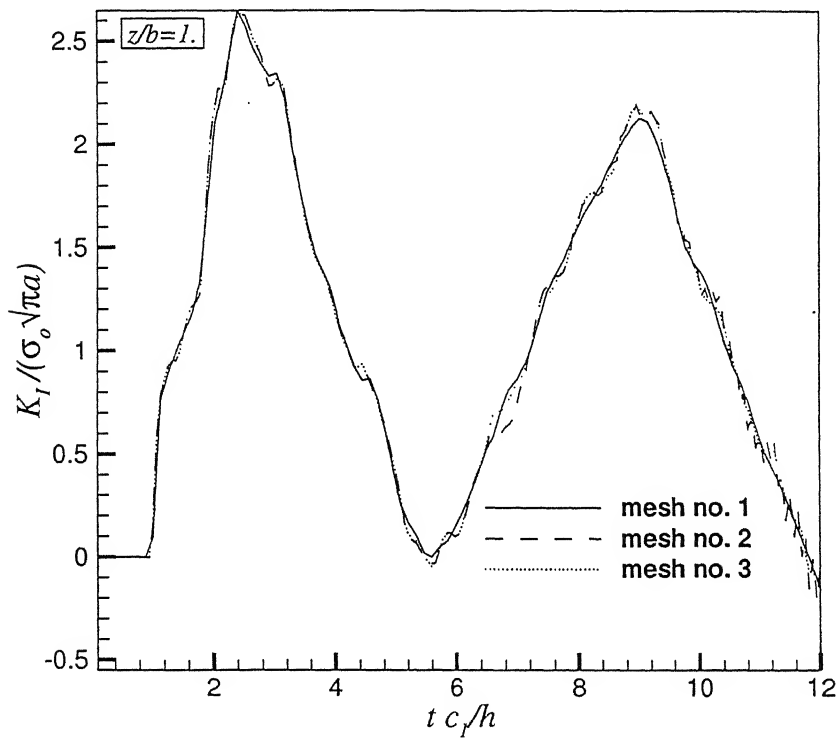


Figure 4.5: DSIF variation with time at mid-surface position on crack front for different meshes (Table 4.1)

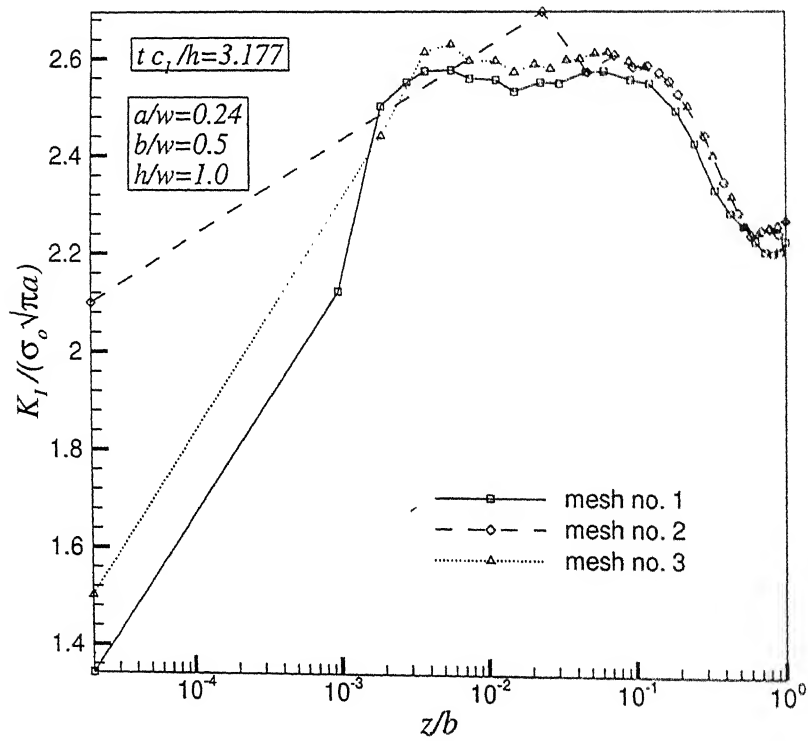


Figure 4.6: DSIF variation along crack front for time instant $t c_1/h = 3.177$ for different meshes (Table 4.1)

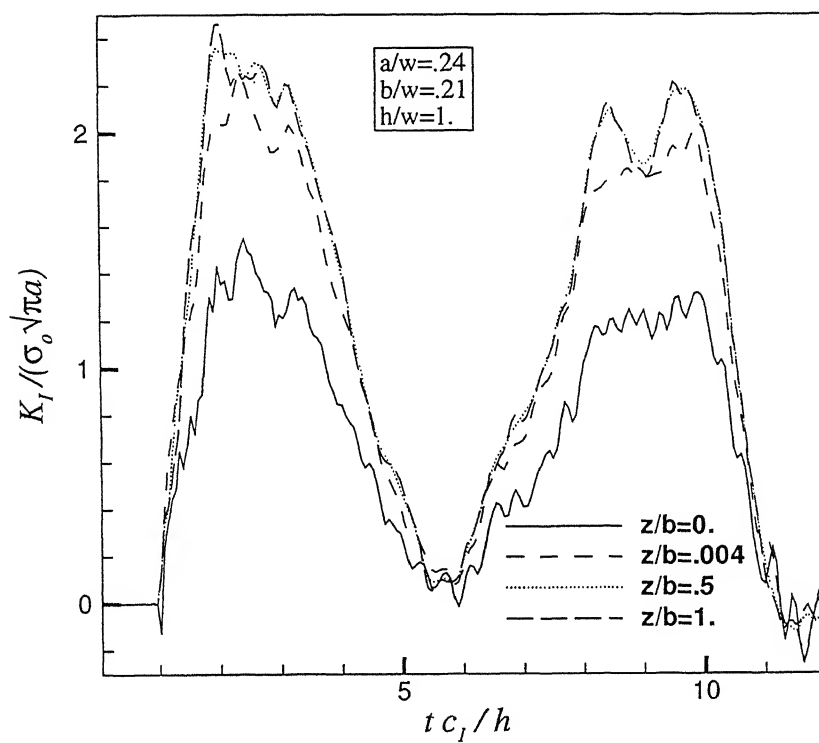


Figure 4.7: Plots of $K_I(t)$ for different positions on the crack front for Mesh no. 4 (Table 4.1)

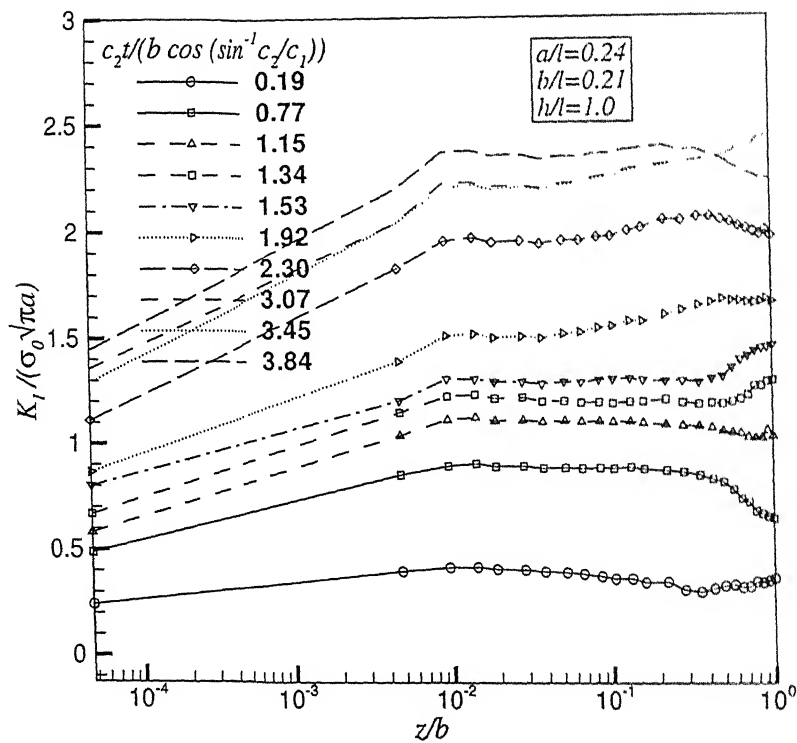


Figure 4.8: DSIF variation along the crack front at different instants of time, starting from the instant longitudinal wave strikes the crack face

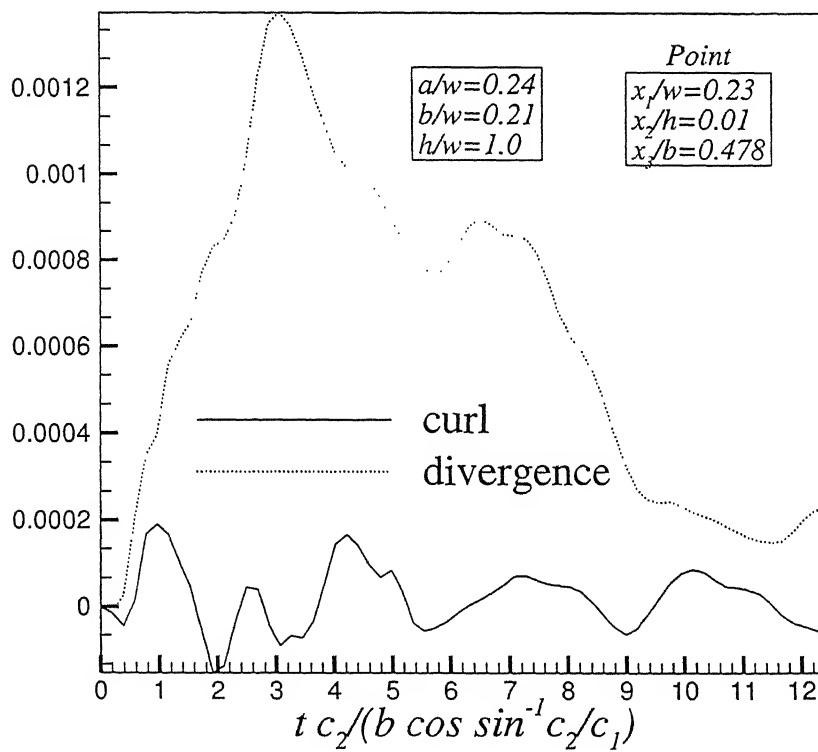


Figure 4.9: Plot of x_1 -component of curl of displacement vector at an internal point with respect to time from the instant longitudinal wave strikes the crack face

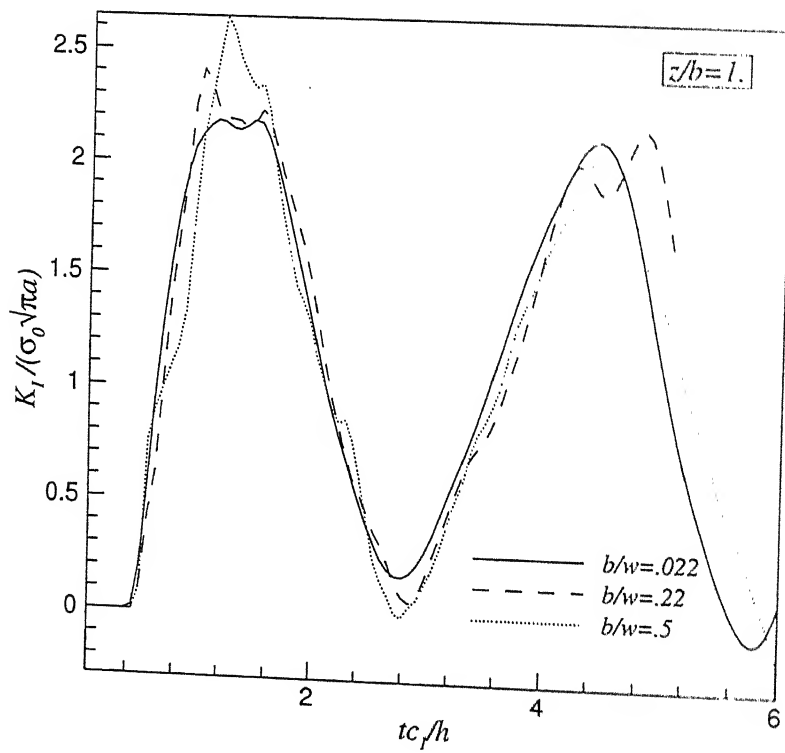


Figure 4.10: Comparison of mid-surface $K_I(t)$ for different thicknesses of Mode-I specimen

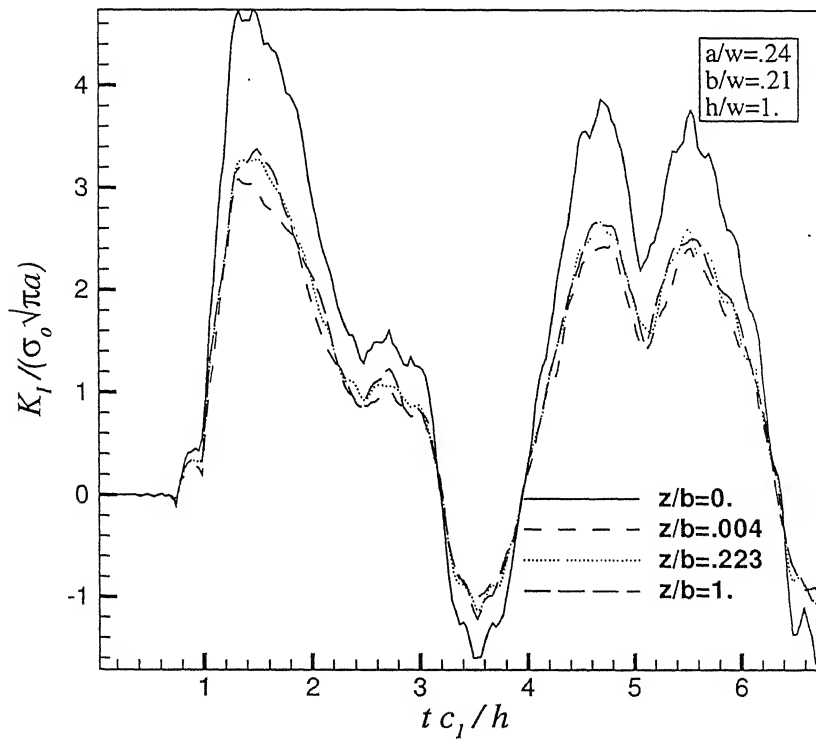


Figure 4.11: Plots of $K_{II}(t)$ at different positions along crack front for Mode-II loading

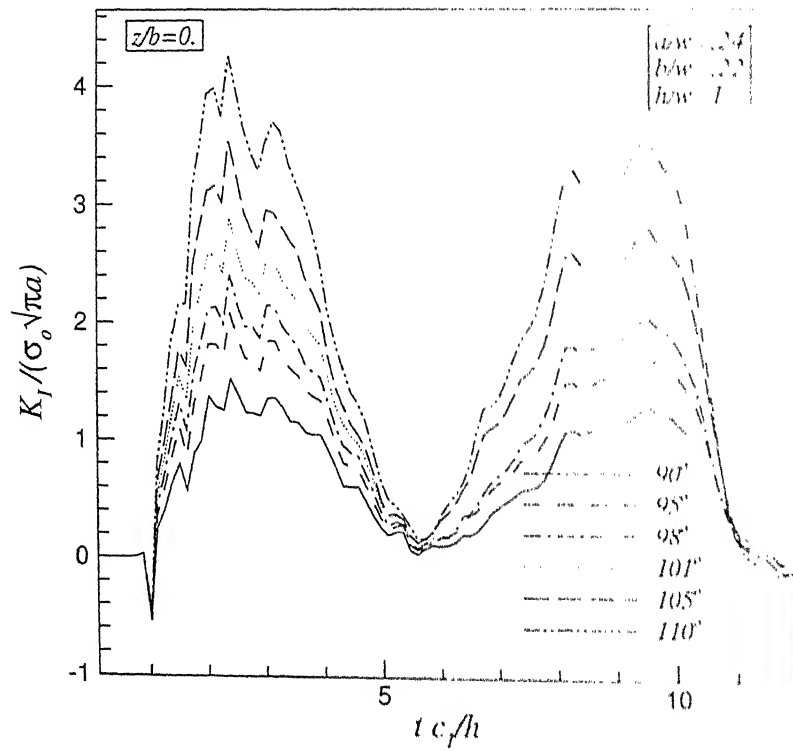


Figure 4.12: Plots of $K_I(t)$ at crack vertex for different intersection angles of crack front with free surface

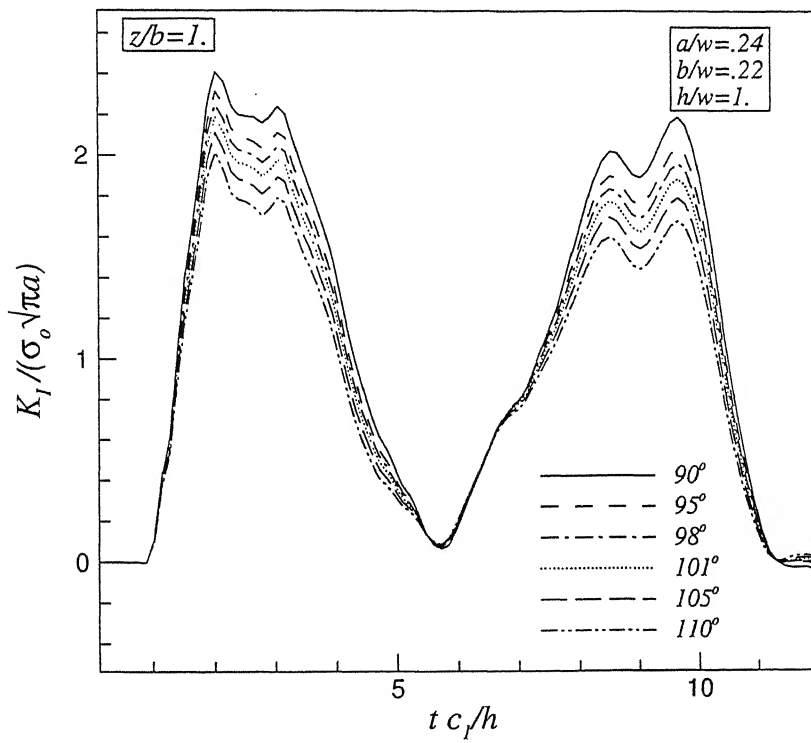


Figure 4.13: Plots of $K_I(t)$ at mid-surface for different intersection angles of crack front with free surface

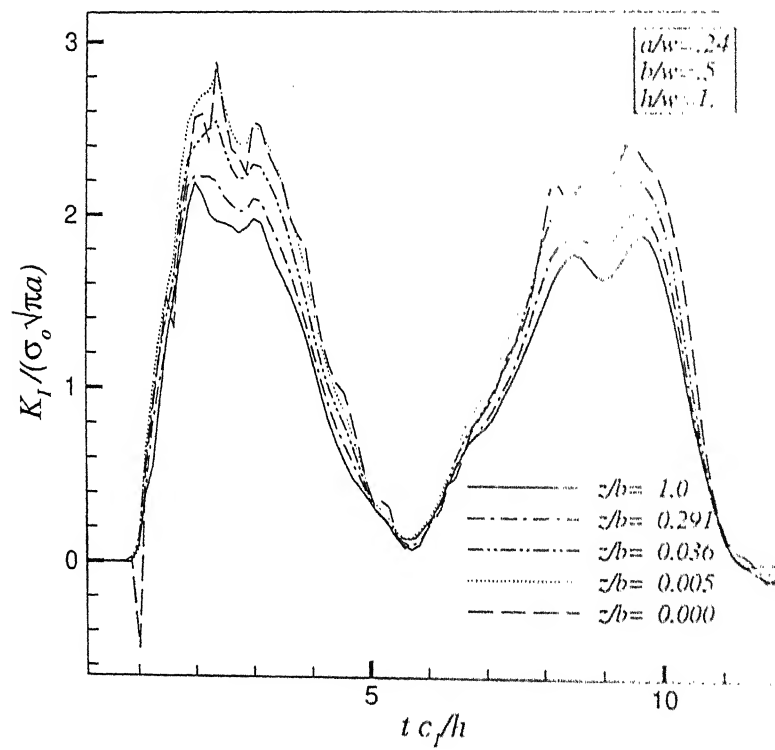


Figure 4.14: Plots of $K_I(t)$ at different positions along crack front for intersection angle of 101°

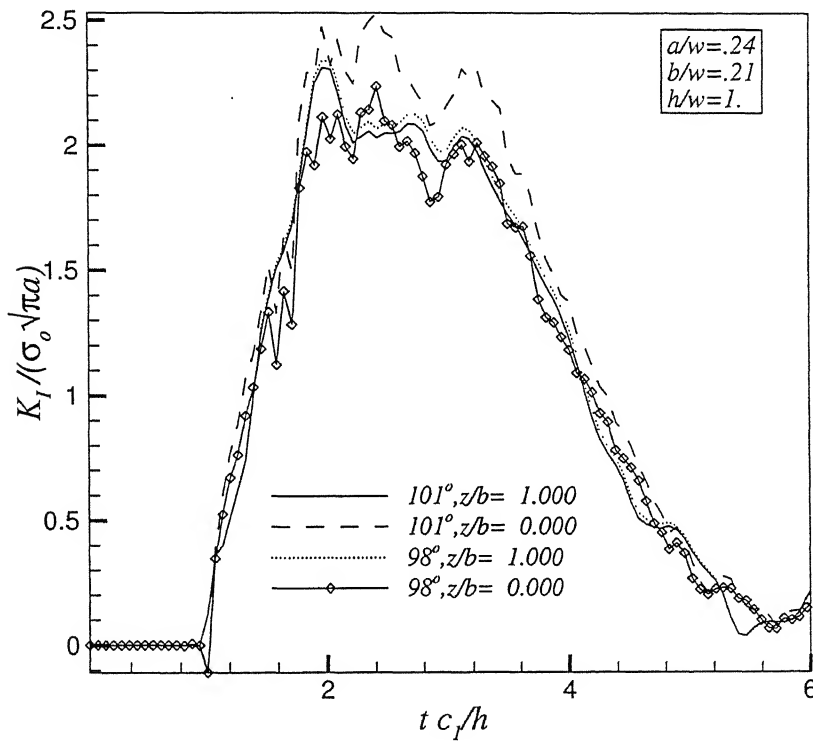


Figure 4.15: Comparison of $K_I(t)$ at free-surface and mid-surface for intersection angles of 101° and 98°

Chapter 5

Dynamic Analysis: Running Crack

This chapter deals with the implementation of a three-dimensional time-domain boundary integral formulation for a moving center-crack in a finite solid under suddenly applied crack face pressure. The BEM displacement time domain formulations have, hitherto, been limited to analyzing two-dimensional crack problems, though hypersingular formulations have been used to analyze finite cracks in infinite domains. In this chapter, variation of dynamic stress intensity factor (DSIF) along the crack front for a moving, through-thickness straight crack is studied for a finite solid under step loading. The state of stress is evaluated at the crack vertex, where crack front meets the free surface. The effect of free surface on DSIF is investigated. It is possible to estimate accurately the critical intersection angle of the crack front with the free surface at which square-root singularity is restored at the crack vertex under step loading for various speeds of crack propagation. It is also predicted in this work that for high speeds of crack propagation, crack front maintains its straight profile.

5.1 Introduction

In the present work, the standard 3-D time-domain boundary integral formulation is implemented for a self-similar moving center-crack for a finite solid under suddenly applied crack face pressure loading. Variation of DSIF is studied along the crack front for the through-thickness crack.

A crack front intersecting the free surface in a 3-D body has been a subject of interest for last three decades. Through-thickness fatigue cracks in plate geometries almost always show crack front tunnelling, i.e., a curved crack front with the deepest point of the crack at the center. Benthem [1] analyzed a problem of a quarter-plane crack in a semi-infinite

half-space subjected to symmetric quasi-static loading. For a crack front normal to the free surface, he derived that at the corner point, stresses have $r^{-1/2}$ singularity for Poisson's ratio (ν) of 0.3. By a local finite element analysis, Bazant and Estenssoro [2] estimated the critical intersection angle to be 101° (for $\nu = 0.3$) for a stationary crack under elastostatic loading. By a finite element formulation similar to that used by Bazant and Estenssoro [2], Gudmundson and Östlund [3] found for a half-space problem that a weaker singularity also exists at the corner point for a dynamically growing crack and estimated the critical angle to be 101° , almost independent of the crack-tip velocity. They found that for angles between 90° and about 101° , singularity weakened further with increasing velocity and for angles larger than about 101° , singularity became stronger with increasing velocity.

The success enjoyed by these local numerical analyses is not found to the same extent in finite element treatments of more global or complete problems which contain crack/surface intersections. Different predictions were made concerning the variation in energy release rate (G) with some results showing an increase in G in the free surface region, some a decrease and still others no change for quasi-static analysis. Burton *et al.* [4] generated critical crack profiles using FEM with each profile having less than 2% numerical variation in G with depth. The crack profiles generated by them were significantly less curved than those observed in practice [5]. Using FEM for analysis, Lin and Smith [6] found that slightly non-orthogonal intersection caused a great loss of path-independence in the value of J integral up to 47% near the free surface. Thus in global situation, finite element analysis is not able to obtain an accurate stress state adjacent to the crack tip in the region close to the free surface, especially for cracks which are not normal to the surface. In a review article, Nishioka [91] has reported from an FEM analysis that value of the dynamic J -integral reduces near the free surfaces of the plate for a through-thickness straight running crack. Agrawal and Kishore demonstrated the effectiveness of BEM in evaluating state of stress at crack vertex and estimating critical intersection angles accurately for quasi-static loading [90] and for impact loading of a stationary crack [98].

The present work uses direct 3-D time-domain formulation of boundary element method to study the effect of free surface on stress intensity factor distribution along the crack front for a moving through-thickness crack in a finite solid under step loading. The algorithm used in the present work is similar to the one used by Gallego and Dominguez [10] for analysis of running crack in 2-D analysis. SIFs are computed along the crack front from nodal values of traction in boundary element analysis [60]. Straight as well as curved crack profiles are studied in the present work. Critical intersection angle of crack front

with free surface computed in this work for step loading matches closely with the value of critical angle predicted by Bažant and Estenssoro [2] for elastostatic loading for a half-space problem. But author is not aware of any work in which critical intersection angles have been estimated for impact loading for a moving crack for a finite solid.

Also for high speeds of crack propagation, a straight crack front is predicted by the present work. At crack vertex, DSIF value is calculated to be higher than that at rest of the crack front for high crack speeds, just an opposite behavior to low speed crack propagation or stationary crack case. Ravi-Chandar and Knauss [38] had observed with high speed micrography that under conditions of low stress intensity the crack front exhibits “thumbnail” curvature similar to the crack profiles associated with quasi-static fracture processes. They also observed that at increasing stress intensity the crack front straightens out and is identifiable as a front of multiple micro-fractures. Parton [37] experimentally observed that if crack velocity exceeds a certain value, then the arrival of waves reflected from the free boundaries to the crack tip does not affect its velocity, implying that the zone of process occurrence has a certain inertia, i.e., it shows some resistance to the ‘attempts’ to change its velocity. Based on the boundary element analysis in this study, it seems to the author that beyond a certain crack velocity, crack behaviour undergoes a distinct change or inertial terms start dominating the square-root singular terms. The possibility that the extent of the stress intensity factor during dynamic crack growth under transient conditions is more limited than a steady-state analysis would indicate was first suggested by the analysis of Ma and Freund [40]. Under severe transient conditions, the local crack tip field is not accurately represented by a stress intensity factor field. At higher crack speeds, the higher-order terms in the near-field asymptotic expansion can have a significant influence on the crack tip stress field [41] even for the case of constant crack speed, following fracture initiation. During the early stages of crack growth, the other terms may dominate the square root singular term under certain conditions. During the early phase of crack growth, the transient nature of stress field prevents a complete stress intensity factor from becoming established outside the near-tip three-dimensional zone. This feature erodes the value of the stress intensity factor concept in characterizing the fracture resistance of the material.

A long-standing issue of fundamental importance in dynamic fracture research is the connection between the dynamic fracture toughness and the crack tip velocity. The debate, for the most part, has centered around the question of uniqueness of a relationship between K_I^d and v . Kobayashi and Dally [42], Rosakis *et al.* [43] and Zehnder and Rosakis [44],

among others, provided data sets that seem to indicate that K_I^d v relation is reasonably viewed as a material property. On the other hand, the results of Kobayashi and Mall [45] and Ravi-Chandar and Knauss [39], based on photo-elasticity and the method of caustics in transmission, respectively, suggest that there is no such correspondence. The fundamental difficulty of achieving a well-developed stress intensity factor field may be playing a significant role in these differences in results. The problem may also lie in the assumption of linear elastic material response. Both the analysis and the models that underlie the interpretations of these experiments are two-dimensional in nature. In either case, the three-dimensional effects that are overlooked may have too much of an influence to be neglected in considering the process [40].

For a stationary crack under suddenly applied uniform crack face pressure, Ma and Freund [40] found that stress intensity factor field is found only for points closer to the crack tip than about 5–10 percent of the distance to the cylindrical shear wave front, implying that the extent of the K field is so small at the onset of growth. They found that measured and calculated stress intensity factor histories compare very well for relatively low crack face pressures, but there is significant disagreement beyond crack growth initiation for higher pressures. The time required, before the singular stress becomes a good estimate of the total stress, decreases as the delay time increases. Delay time is the time between the onset of crack growth and the time instant when pressure is suddenly applied on the crack face.

Conditions of K_I^d dominance exist either extremely close to the crack-tip or are eventually established at long times after crack initiation. However, the higher order transient asymptotic representation is more successful in describing the actual field even at times close to the event of crack initiation or at distances relatively far away from the moving crack tip. The transient effect is manifested through the time derivative of the dynamic stress intensity factor even if the crack-tip speed is constant.

It is necessary to apply the higher order asymptotic expansion which includes the transient history of the crack growth to describe the near tip deformation fields. Also the crack growth is indeed controlled by a material related criterion. This criterion gives the unique relationship between the dynamic fracture toughness K_{IC}^d and the crack-tip speed v . The existence of such a criterion was seen validated in a simulation by Liu and Rosakis [46] by using the higher order transient expansion, while the lack of the uniqueness of a relationship between K_{IC}^d and v has been observed when the K_I^d -dominant assumption or the steady state higher order expansion is used [39, 45].

In the present study, the author has investigated if it is possible to capture this loss of square-root dominance by the boundary element analysis. SIF is calculated from crack-tip or crack front tractions in BEM. Value of traction at a node on crack front exhibits an integrated influence of level of singularity over the elements adjoining it. **Any weakening of singularity, for example at crack vertex due to free surface effect or loss of dominance of square-root terms at high speeds of crack propagation, gets reflected in the value of SIF calculated from nodal tractions.**

In the past three decades, the application of the finite element method (FEM) to dynamic crack propagation has made important advances. Interesting reviews can be found in the papers by Aoki *et al.* [47] and by Atluri and Nishioka [48]. Two different approaches followed are based on one of the following two concepts: a stationary mesh, which includes a 'node release' mechanism, or a moving mesh which normally includes a singular element.

The BEM has appeared as an alternative for elastic fracture mechanics problems. This method seems to be a better choice than FEM for elastodynamic fracture mechanics because the discretization is restricted to the boundary surface and the concept of singular element is simplified. In particular when dealing with dynamic crack propagation, the remeshing is conceptually much simpler in BEM than in any domain technique. Classical methods like finite difference method or FEM are difficult to apply to the study of crack growth because of their intrinsic numerical dissipation of high frequency elastic waves.

Several different boundary element formulations exist for study of dynamic fracture. Hypersingular formulations have been used to analyze finite plane cracks in 3-D infinite domains [83,84]. Laplace transform BEM has been used to analyze cracks in finite solids under dynamic loading [85]. Wen, Aliabadi and Rooke [86,87] presented a Laplace transform displacement discontinuity and fictitious stress formulations for 2-D and 3-D problems. They determined the stress intensity factors for several 2-D and 3-D problems using an equivalent stress approach. Das [99] used the displacement discontinuity method to determine the slip of a planar crack propagating in an infinite medium. Das and Kostrov [100] presented displacement and traction equations for 3-D dynamic shear crack propagation problems. Koller *et al.* [101] used the traction equation expressed in terms of displacement discontinuity to analyse dynamic anti-plane cracks. Fedelinski *et al.* [102] extended the dual boundary element formulation in time-domain to analyses of mixed-mode fast growing cracks. Time domain formulation is advantageous where an accurate solution is required from the very beginning and is the best possible approach for problems with

time-dependent geometry [50].

Domínguez and Gallego [60] used the direct time domain boundary element formulation in combination with the traction-singular quarter-point elements that had been used by Martínez and Domínguez [73] and Chirino and Domínguez [88] for static and time-harmonic computations, respectively. Gallego and Domínguez [10] modelled the crack growth in two-dimensional analysis by using moving singular elements and a remeshing technique. For moving elements, they used space- and time-dependent interpolation functions. The same algorithm is extended in the present work to 3-D analysis of problems of dynamic crack propagation in finite bodies. To author's knowledge this is the first time that direct displacement time-domain 3-D BEM is used to study dynamic crack propagation in finite bodies using moving mesh procedure.

5.2 Analytical problem of self-similar, constant velocity, crack-propagation from a finite initial length

A crack propagation problem is described here to facilitate comparison with numerical results later. The analytical problem considered is the growth of a half plane crack in an otherwise unbounded body of a homogeneous, isotropic elastic solid. Suppose that a uniform normal pressure of magnitude σ_∞ begins to act on the faces of the crack at a certain instant, say time $t = 0$. The crack starts growing after an initial delay time τ . The pressure expands over the newly-created crack faces. The analytical solution for the dynamic stress intensity factor in the interval $0 < t < \tau$ (i.e., the crack is stationary) is

$$K(t) = B\sigma_\infty\sqrt{c_1 t} \quad (5.1)$$

Here c_1 is the longitudinal wave speed for the medium and B is a function of Poisson's ratio given in [11]. For times $t > \tau$, the dynamic stress intensity factor for the propagating crack is

where the slowness function $S_+(1/v)$ is an integral arising from Wiener-Hopf factorization for the moving crack problem by Freund [11, 12]. Freund [12] notes that $S_+(1/v)$ is "not too different from unity over the full range of its argument" and it is given as

$$S_+(1/v) = \exp\left[-\frac{v}{\pi} \int_{c_2}^{c_1} \tan^{-1}\left\{\frac{4\sqrt{(1-c^2/c_1^2)(c^2/c_2^2-1)}}{(2-c^2/c_2^2)^2}\right\} \frac{dc}{c(c-v)}\right] \quad (5.4)$$

Values for $S_+(1/v)$ and $k(v)$ for Poisson's ratio of 0.3 for several values of v/c_R are shown in Table 5.1. Here, B is defined as

$$B = 2 \frac{\sqrt{(1-2\nu)/\pi}}{1-\nu} \quad (5.5)$$

For the particular situation of crack face pressure expanding over the newly created crack faces, DSIF is independent of arbitrary delay time after $t > \tau$.

5.3 Transient Boundary Integral Formulation

Consider a homogeneous, isotropic and linearly elastic body of volume V bounded by a regular surface S , with its mass density ρ and dilatational and shear wave speeds as c_1 and c_2 respectively. Using Stoke's state of quiescent past corresponding to a point load with a Dirac delta function variation, Love's integral representation can be derived using Betti's reciprocal theorem. For zero initial conditions and zero body forces, the displacement of a point \mathbf{y} can be represented by the following boundary integral equation:

$$C_{ij}(\mathbf{y})u_i(\mathbf{y}, T) = \int_S [G_{ij}(\mathbf{x}, \mathbf{y}, T) * t_i(\mathbf{x}, T) - H_{ij}(\mathbf{x}, \mathbf{y}, T) * u_i(\mathbf{x}, T)] dS(\mathbf{x}) \quad (5.6)$$

where

$$G_{ij} * t_i = \int_0^T G_{ij}(\mathbf{x}, T; \mathbf{y}, \tau) t_i(\mathbf{x}, \tau) d\tau \quad (5.7)$$

$$H_{ij} * u_i = \int_0^T H_{ij}(\mathbf{x}, T; \mathbf{y}, \tau) u_i(\mathbf{x}, \tau) d\tau \quad (5.8)$$

are Riemann convolution integrals. In the above, $u_i(\mathbf{x}, \tau)$ and $t_i(\mathbf{x}, \tau)$ are the displacement and traction components respectively at point \mathbf{x} and time τ . The free-term tensor C_{ij} is calculated by general close-form expression developed by Mantic [56]. The fundamental solutions G_{ij} and H_{ij} are the displacements and tractions in direction i at a point \mathbf{x} at time T due to a unit impulse vector in direction j applied at a point \mathbf{y} at a preceding time τ . The fundamental solutions are given in explicit form as

$$G_{ij}(\mathbf{x}, T; \mathbf{y}, \tau) = \frac{1}{4\pi\rho} \left[(3a_{ij} - b_{ij}) \int_{1/c_1}^{1/c_2} \lambda \delta(v - \lambda r) d\lambda \right]$$

$$+a_{ij}\{(1/c_1^2)\delta(v-r/c_1) - (1/c_2^2)\delta(v-r/c_2)\} + (b_{ij}/c_2^2)\delta(v-r/c_2)\} \quad (5.9)$$

where $v = T - \tau$; $a_{ij} = h_i h_j / r^3$; $b_{ij} = \delta_{ij} / r$; $h_i = x_i - y_i$; r is the distance between points \mathbf{x} and \mathbf{y} . Also δ_{ij} is the Kronecker's delta and δ is the Dirac delta function.

$$\begin{aligned} H_{ij}(\mathbf{x}, T; \mathbf{y}, \tau) = & \frac{1}{4\pi} \left[-6c_2^2(5d_{ij} - e_{ij}) \int_{1/c_1}^{1/c_2} \lambda \delta(v - \lambda r) d\lambda + (12d_{ij} - 2c_{ij}) \{ \delta(v - r/c_2) \right. \\ & - (c_2/c_1)^2 \delta(v - r/c_1) \} + 2rd_{ij}/c_2 \{ \dot{\delta}(v - r/c_2) - (c_2/c_1)^3 \dot{\delta}(v - r/c_1) \} \\ & - f_{ij}(1 - 2c_2^2/c_1^2) \{ \delta(v - r/c_1) + (r/c_1) \dot{\delta}(v - r/c_1) \} - g_{ij} \{ \delta(v - r/c_2) \\ & \left. + (r/c_2) \dot{\delta}(v - r/c_2) \} \right] \quad (5.10) \end{aligned}$$

where $v = T - \tau$; $h_i = x_i - y_i$; $d_{ij} = h_i h_j h_m n_m / r^5$; $f_{ij} = h_j n_i / r^3$; $g_{ij} = (h_i n_j + \delta_{ij} h_m n_m) / r^3$; $e_{ij} = f_{ij} + g_{ij}$. Also n_i are the components of outward pointing normal vector and $n_m h_m = n_1 h_1 + n_2 h_2 + n_3 h_3$.

5.4 Numerical implementation

The time-domain BEM in three-dimensions consists of two basic steps as explained in [49, 58, 59]:

1. A discretization of the real time axis into a sequence of equally spaced time intervals with the assumption of linear variation of displacements and tractions over each time interval. When piecewise linear variation is used for both displacements and tractions, the time-stepping scheme is supposed to become unstable [60, 61].

But in this study, piecewise constant interpolation for traction variable is seen to give poor results in 3-D time domain analysis. So traction variable is also linearly interpolated in time like displacement variable. Good results are obtained and instability is not seen to affect the results. It is, in contrast, with stationary crack results where linear time-stepping for traction variable results in instability. It is possible that for moving elements, self-effect dominates over the other-effect [103] for linear interpolation of tractions over time and hence, resulting in stability of numerical scheme.

2. A discretization of boundary into 8-noded elements.

The time span of interest is divided into N equal time steps of size ΔT so that

$$T_n = n \Delta T, \quad n = 1, 2, \dots, N. \quad (5.11)$$

On the basis of these discretizations a time stepping solution of equation (5.6) can be established for the boundary displacements and tractions over each element and for each time step.

The displacement boundary integral equation can be written as

$$C_{ij}u_i(\mathbf{y}, T_N) - \int_{T_{N-1}}^{T_N} \int_S [G_{ij}t_i - H_{ij}u_i] dS d\tau = \int_0^{T_{N-1}} \int_S [G_{ij}t_i - H_{ij}u_i] dS d\tau \quad (5.12)$$

where the integral on the right hand side is the contribution due to past dynamic history. This equation is also an exact statement since no approximation has yet been introduced. However, in order to solve the above equation, one has to approximate the time variation of the field quantities, in addition to the usual approximation of spatial variation. The time integration in the above equation is done analytically, and the spatial integration is done numerically. A system of algebraic equations is obtained at time step N through nodal collocation, i.e., by allowing \mathbf{y} to coincide sequentially with all the nodal points of the boundary.

Equation (5.12) can be written in a more condensed form as a typical BE equation:

$$C_{ij}^p u_i^{Np} + \sum_{n=1}^N \sum_{q=1}^Q H_{ij}^{Nnpq} u_i^{nq} = \sum_{n=1}^N \sum_{q=1}^Q G_{ij}^{Nnpq} t_i^{nq} \quad (5.13)$$

or, in matrix form:

$$\sum_{n=1}^N \mathbf{H}^{Nn} \mathbf{u}^n = \sum_{n=1}^N \mathbf{G}^{Nn} \mathbf{t}^n \quad (5.14)$$

where \mathbf{u}^n and \mathbf{t}^n include the three displacement and traction components of all the nodes at time step n . Here, p and q denote the collocation point and integration element respectively. And Q are the number of elements in the boundary element mesh.

5.4.1 Temporal and spatial interpolation of displacement and traction

The boundary variables are interpolated in terms of their values at nodes by

$$u_i(\mathbf{x}, \tau) = \sum_{n=1}^N [M_I^n u_i^{n-1}(\mathbf{x}) + M_F^n u_i^n(\mathbf{x})] \quad (5.15)$$

$$t_i(\mathbf{x}, \tau) = \sum_{n=1}^N [M_I^n t_i^{n-1}(\mathbf{x}) + M_F^n t_i^n(\mathbf{x})] \quad (5.16)$$

and

$$u_i^n(\mathbf{x}) = \sum_{c=1}^8 N^c [\xi(\mathbf{x})] u_i^{nc}, \quad i = 1, 2, 3 \quad (5.17)$$

$$u_i^{n-1}(\mathbf{x}) = \sum_{c=1}^8 N^c [\xi(\mathbf{x})] u_i^{(n-1)c}, \quad i = 1, 2, 3 \quad (5.18)$$

where u_i^{nc} and $u_i^{(n-1)c}$ represent nodal values of displacement at time nodes n and $(n-1)$ respectively. Similar interpolation is done for traction variables also. Here, N is the total number of time steps. M_I and M_F are the temporal interpolation functions, related to local time nodes I (initial) and F (final), and are of the following form for piece-wise linear variation:

$$M_I^n = \frac{T_n - \tau}{\Delta T} \phi_n(\tau) \quad (5.19)$$

$$M_F^n = \frac{\tau - T_{n-1}}{\Delta T} \phi_n(\tau) \quad (5.20)$$

where

$$\phi_n(\tau) = \begin{cases} 1 & \text{if } (n-1)\Delta T \leq \tau \leq n\Delta T \\ 0 & \text{otherwise} \end{cases}$$

or

$$\phi_n(\tau) = H(\tau - (n-1)\Delta T) - H(\tau - n\Delta T) \quad (5.21)$$

H being the Heaviside function.

Both displacements and tractions are interpolated by piecewise linear functions in the present work.

For spatial interpolation of boundary variables, an approach [62] which combines the advantages of continuous and discontinuous elements in a single formulation is used in this work. In this formulation, expressions of the shape and interpolation functions are unified in a form suitable for fully continuous, fully discontinuous or transition elements (i.e., discontinuous only along one or more edges). Three types of boundary nodes are identified depending on the function they fulfil:

1. Geometrical nodes: those used for interpolating the boundary geometry.
2. Interpolation nodes: the points on the boundary which define the interpolation of the variables. The system nodal values correspond to these nodes.

3. Collocation nodes: where the boundary integral equation is enforced.

One property of the boundary element formulations is that the discontinuities of the variable across the element edges do not invalidate the convergence of the technique [63]. Collocation and interpolation nodes for continuous elements coincide with the geometrical nodes. Collocation nodes and interpolation nodes for discontinuous elements and discontinuous side of transition elements are situated inside the element. For quarter-point element, geometrical and interpolation nodes coincide, but collocation corresponding to nodes on crack front is done at nodes situated inside the elements on either side of the crack front. To reduce the number of equations and enhance accuracy, equations corresponding to collocation nodes before and after a given interpolation node are added up [64].

5.4.2 Analytical integration of temporal terms

The time integration in equation (5.12) after using equations (5.15) and (5.16) is done analytically and the spatial integration is performed numerically. Explicit expressions for time integrals may be seen in [49, 58]. Temporal integration boils down to integration of terms like $\int_0^{\Delta T} \delta(T - \tau - r/c) M_I^1(\tau) d\tau$, $\int_0^{\Delta T} \int_{1/c_1}^{1/c_2} \lambda \delta(T - \tau - \lambda r) M_I^1(\tau) d\lambda d\tau$ etc.

For example,

$$\int_0^{\Delta T} \delta(T - \tau - r/c) (1 - \tau/\Delta T) \phi_1(\tau) (\tau) d\tau = \begin{cases} (1 - \frac{T}{\Delta T}) + \frac{1}{c\Delta T} r & \text{if } c(T - \Delta T) < r < cT \\ 0 & \text{otherwise} \end{cases} \quad (5.22)$$

Similarly, all other temporal terms can be expressed in the form $a + br + \frac{d}{r^2}$ after analytical integration in time. For moving elements, temporal integration also results in an additional r^2 term. It is noticed that for the distance reached by both shear and compression waves travelling from a source node up to a time ΔT , coefficient of $\frac{1}{r^2}$ is zero. Thus, the temporal terms, i.e., time integrations are not adding to the singularity in r . Here, c is compression (c_1) or shear (c_2) wave speed.

5.4.3 Spatial integration

The kernels in elastodynamic case have discontinuous derivatives at points such that $r/c_{1(2)} = k\Delta T$ (k integer). Therefore, the standard numerical methods, like Gaussian integration, give poor results if applied over the whole element. So a partitioning scheme is used for elements so as to facilitate accurate spatial integration [98].

Principal value singularity occurs for traction kernel H_{ij} when source element becomes also a receiver. The Cauchy principal value integral is treated in the same way, as done

by Guiggiani and Gigante [7] for the elastostatic case with the help of partitioning scheme proposed in [98]. The non-linear transformation suggested by Doblaré and Gracia [66] is also incorporated.

Angular variable transformation of Hayami [79] is used to weaken the angular near-singularity arising when collocation node is near the edge of an element.

5.4.4 Crack Elements

Quarter-point elements are used along the crack front and traction-singularity is incorporated in the quarter-point elements ahead of the crack front [71, 72]. The stress intensity factors can be computed directly by the boundary element code as follows:

$$\begin{aligned} K_I &= \bar{t}_2^I \sqrt{2\pi l} \\ K_{II} &= \bar{t}_1^I \sqrt{2\pi l} \\ K_{III} &= \bar{t}_3^I \sqrt{2\pi l} \end{aligned} \quad (5.23)$$

where \bar{t}_i are the tractions at nodes on the crack front and l is the length of crack front elements in the direction of singularity. It may be noted that the use of traction nodal values of the singular element at the crack tip for SIF computation is substantially less sensitive to the discretization than any of the displacement correlation procedures [60].

5.5 Formulation for a moving singular element

This formulation is useful for multi-domain or symmetric modelling to simulate crack growth. In multi-domain modelling, a boundary is introduced along the crack, following the known direction of propagation. Because of symmetry of the problem under consideration, only one-eighth of the domain is analysed. Assume that crack propagates at a speed v and that at time T , the position of the crack front and the discretization of the part of the boundary that contains the crack are shown in Fig. 5.1. The elements adjoining the crack front are quarter-point elements. After a time increment ΔT , the crack front has moved $v\Delta T$. As the crack front advanced from left to right, all the elements before and after the crack front are also shifted to the right by $v\Delta T$. Only centroids of the leftmost and the rightmost columns of elements shift by $\frac{1}{2}v\Delta T$, the leftmost and the rightmost edges remaining stationary. Thus, the leftmost column of elements increase in size and the rightmost column of elements decrease in size and elements in between these two columns of elements remain the same size. Crack propagation is studied in the present work till the

time the rightmost column of elements can be decreased no further in size. To start with a mesh is prepared having small elements in the leftmost column and large elements in the rightmost column, so as to allow large amount of crack growth without requiring addition of new column of elements to the left of crack front and deletion of an existing column of elements to the right of crack front. Above scheme of element movement helps in reducing computations of matrices, as will be explained later. In the boundary element mesh shown in Fig. 4.3, elements on the bottom plane move with the crack front. Elements on the front, top and the back faces are also moved with the crack front in a similar fashion as the elements on the bottom face.

The BE matrix for time step N can now be written in a subdivided form as

$$\sum_{n=1}^N \begin{pmatrix} \mathbf{H}_{ff}^{Nn} & \mathbf{H}_{fc}^{Nn} \\ \mathbf{H}_{cf}^{Nn} & \mathbf{H}_{cc}^{Nn} \end{pmatrix} \begin{pmatrix} \mathbf{u}_f^n \\ \mathbf{u}_c^n \end{pmatrix} = \sum_{n=1}^N \begin{pmatrix} \mathbf{G}_{ff}^{Nn} & \mathbf{G}_{fc}^{Nn} \\ \mathbf{G}_{cf}^{Nn} & \mathbf{G}_{cc}^{Nn} \end{pmatrix} \begin{pmatrix} \mathbf{t}_f^n \\ \mathbf{t}_c^n \end{pmatrix} \quad (5.24)$$

where the subindex 'f' stands for the nodes whose position remains fixed during the remeshing process and 'c' for those that change position during that process. It is important that when equation (5.24) is written for a new time step N , the sub-matrices corresponding to changing collocation nodes and/or to changing collocation elements have to be calculated anew for all the previous time steps n . The translation property of the fundamental solution cannot be used in those cases because the position of the nodes at time step N is not the same as before. Thus H_{ij}^{Nnpq} and G_{ij}^{Nnpq} depend on the N and n values and not only on the difference $N - n$. But for the combination of moving elements and moving collocation nodes, where there is no change in relative position of collocation nodes and integration elements, translation property can still be made use of, starting from the time interval when crack starts propagating. All moving elements, except for the leftmost and the rightmost columns of elements, fall into this category.

For moving elements, the space interpolation functions of the variables move with the elements and therefore, these functions are not only space dependent but also time dependent. Displacements and tractions for moving elements are represented as follows:

$$u_i(\mathbf{x}, \tau) = \sum_{n=1}^N [M_I^n u_i^I(\mathbf{x}, \tau) + M_F^n u_i^F(\mathbf{x}, \tau)] \quad (5.25)$$

$$t_i(\mathbf{x}, \tau) = \sum_{n=1}^N [M_I^n t_i^I(\mathbf{x}, \tau) + M_F^n t_i^F(\mathbf{x}, \tau)] \quad (5.26)$$

In the regular formulation of the time domain BEM, the space shape functions are separated from the time integrals which are done analytically. This is not possible when space shape

functions are time-dependent. In order to do the time integration, an approximation of the space shape functions' time dependence is used [10]. Two terms of their series expansion are taken:

$$\begin{aligned}
 u_i^I(\mathbf{x}, \tau) &= u_i^{n-1}(\mathbf{x}) + (\tau - T_{n-1})\dot{u}_i^{n-1}(\mathbf{x}) \\
 u_i^F(\mathbf{x}, \tau) &= u_i^n(\mathbf{x}) + (\tau - T_n)\dot{u}_i^n(\mathbf{x}) \\
 t_i^I(\mathbf{x}, \tau) &= t_i^{n-1}(\mathbf{x}) + (\tau - T_{n-1})\dot{t}_i^{n-1}(\mathbf{x}) \\
 t_i^F(\mathbf{x}, \tau) &= t_i^n(\mathbf{x}) + (\tau - T_n)\dot{t}_i^n(\mathbf{x})
 \end{aligned} \tag{5.27}$$

Assume that for each time step the elements move with a constant speed v in x_1 -direction same as that of the crack front, the shape functions can be written as

$$\begin{aligned}
 u_i(x_1, x_2, x_3, \tau) &= u_i(x_1 - v\tau, x_2, x_3) \\
 &= u_i(x, x_2, x_3)
 \end{aligned} \tag{5.28}$$

The functions on the opposite sides of the equation in (5.28) are different, of course, but the values of the functions represent one and the same physical quantity. The x, x_2, x_3 -coordinate system translates at speed v in the x_1 - or x -direction with the origin of coordinates in this system on the crack front.

Then,

$$\dot{u}_i(x_1, x_2, x_3, \tau)|_{\tau=T_{n-1}} = -v \frac{\partial u_i^{n-1}(\mathbf{x})}{\partial x} \tag{5.29}$$

$$\dot{u}_i(x_1, x_2, x_3, \tau)|_{\tau=T_n} = -v \frac{\partial u_i^n(\mathbf{x})}{\partial x} \tag{5.30}$$

The expressions of shape functions for $u_i(\mathbf{x})$ and $t_i(\mathbf{x})$ are those of the usual shape functions and their derivatives are easily obtained. In the present work for traction singular elements, $t_i(\mathbf{x})$ is singular of the kind $x^{-1/2}$ which makes its derivative singular of the kind $x^{-3/2}$ and the concerned integral a hypersingular one. Gallego and Dominguez [10] computed the finite part of these integrals in their 2-D analysis of moving crack problem. Similar approach is followed and finite part of these integrals is computed as explained later.

5.6 Finite-part integration

Owing to the unknown transformation properties of the finite-part integrals undergoing a non-linear coordinate transformation, the definition formula of the finite-part integrals

is applied in extrinsic coordinate system. The resulting integrals are regular and may be evaluated by standard Gaussian quadrature rules [104].

In this work, integration is performed in extrinsic polar coordinates with origin at projection of collocation node on the plane tangent on the closest point on the element under integration (Fig. 5.3). Corresponding to a Gauss point G , a point G_o is found on the crackfront along the direction of singularity of stresses. Subtraction of value of the kernel at point G_o from the kernel at point G makes the integrand regular by weakening the $x^{-3/2}$ singularity. Corresponding term which is added requires finite part integration. Corresponding to (ρ, θ) coordinates of point G , intrinsic coordinates (ξ, η) are calculated, thus, facilitating evaluation of shape functions at the Gauss point G .

Finite-part integration over the element is done by choosing Gauss points along the crack front and doing finite-part analytical integration along the direction of singularity of stresses for each Gauss point.

5.7 Details of moving mesh algorithm

Equation (5.16) for the interpolation of traction variable t_i for eight-noded elements can be written as

$$t_i(\mathbf{x}, \tau) = \sum_{n=1}^N \sum_{c=1}^8 \left[N^c[\xi(\mathbf{x})] - v(\tau - T_{n-1}) \frac{\partial N^c[\xi(\mathbf{x})]}{\partial x} \Big|_{\tau=T_{n-1}} \right] M^I(\tau) t_i^{(n-1)c} \\ + \left[N^c[\xi(\mathbf{x})] - v(\tau - T_n) \frac{\partial N^c[\xi(\mathbf{x})]}{\partial x} \Big|_{\tau=T_n} \right] M^F(\tau) t_i^{nc} \quad (5.31)$$

Similar expression can be written for the displacement variable. In the chosen problem, crack front is advancing in x_1 - or x -direction. Hence, derivative of shape functions at instant $\tau = T_{n-1}$ and $\tau = T_n$ are calculated from the geometry of the element at time nodes T_{n-1} and T_n respectively as given below:

$$\frac{\partial N^c}{\partial x} \Big|_{\tau=T_{n-1} \text{ or } \tau=T_n} = \frac{\partial N^c}{\partial \xi} \frac{\partial \xi}{\partial x} \Big|_{\tau=T_{n-1} \text{ or } \tau=T_n} + \frac{\partial N^c}{\partial \eta} \frac{\partial \eta}{\partial x} \Big|_{\tau=T_{n-1} \text{ or } \tau=T_n} \quad (5.32)$$

By substitution of Equation (5.31) into the boundary integral equation (5.6), the time integrals can be separated from the space integrals and the coefficients of the system can be written as

$$\int_{S_p} \int_{T_{n-1}}^{T_n} G_{ij}(\mathbf{x}, T_N; \mathbf{y}, \tau) t_i(\mathbf{x}, \tau) d\tau dS =$$

$$\begin{aligned}
& \int_{S_p|_{\tau=T_{n-1}}} \int_{T_{n-1}}^{T_n} G_{ij}(\mathbf{x}, T_N; \mathbf{y}, \tau) M^I(\tau) N^c[\xi(\mathbf{x})] u_i^{(n-1)c} d\tau dS \\
& + \int_{S_p|_{\tau=T_n}} \int_{T_{n-1}}^{T_n} G_{ij}(\mathbf{x}, T_N; \mathbf{y}, \tau) M^F(\tau) N^c[\xi(\mathbf{x})] u_i^{nc} d\tau dS \\
& + \int_{S_p|_{\tau=T_{n-1}}} \int_{T_{n-1}}^{T_n} G_{ij}(\mathbf{x}, T_N; \mathbf{y}, \tau) (-v)(\tau - T_{n-1}) M^I(\tau) \left. \frac{\partial N^c[\xi(\mathbf{x})]}{\partial x} \right|_{\tau=T_{n-1}} u_i^{(n-1)c} d\tau dS \\
& + \int_{S_p|_{\tau=T_n}} \int_{T_{n-1}}^{T_n} G_{ij}(\mathbf{x}, T_N; \mathbf{y}, \tau) (-v)(\tau - T_n) M^F(\tau) \left. \frac{\partial N^c[\xi(\mathbf{x})]}{\partial x} \right|_{\tau=T_n} u_i^{nc} d\tau dS \quad (5.33)
\end{aligned}$$

In above integral over element S_p , temporal integrations are done analytically. Displacement interpolation in a quarter-point element with crack front at $\xi = -1$ (say) can be expressed as

$$\begin{aligned}
u_i(\xi, \eta) &= a_i(\eta)\xi^2 + b_i(\eta)\xi + c_i(\eta) \\
&= a_i(\eta)(2\sqrt{x/L} - 1)^2 + b_i(\eta)(\sqrt{x/L} - 1) + c_i(\eta) \\
&= \frac{x}{L}(4a_i(\eta)) + \sqrt{\frac{x}{L}}(-4a_i(\eta) + b_i(\eta)) + (a_i(\eta) - b_i(\eta) + c_i(\eta)) \quad (5.34)
\end{aligned}$$

where terms x and L denote the distance of field point and extent of crack element respectively from the crack front along the direction of singularity as explained for quadrilateral elements in Fig. 5.3. Traction interpolation in a traction-singular quarter-point element with crack front at $\xi = -1$ can be expressed as

$$\begin{aligned}
t_i(\xi, \eta) &= \sqrt{\frac{L}{x}} [a_i(\eta)\xi^2 + b_i(\eta)\xi + c_i(\eta)] \\
&= \sqrt{\frac{x}{L}}(4a_i(\eta)) + (-4a_i(\eta) + b_i(\eta)) + (a_i(\eta) - b_i(\eta) + c_i(\eta)) \sqrt{\frac{L}{x}} \\
&= A_i(\eta) + B_i(\eta)\sqrt{\frac{x}{L}} + C_i(\eta)\sqrt{\frac{L}{x}} \quad (5.35)
\end{aligned}$$

The derivative of traction variable with respect to coordinate along the direction of crack propagation x (considered here) can be written as

$$\begin{aligned}
\frac{\partial t_i}{\partial x} &= \left(B_i(\eta) \frac{1}{2\sqrt{x}\sqrt{L}} - C_i(\eta) \frac{\sqrt{L}}{2x^{3/2}} \right) \frac{1}{\cos \alpha} + \\
&\quad \left(\frac{\partial A_i(\eta)}{\partial \eta} + \frac{\partial B_i(\eta)}{\partial \eta} \sqrt{\frac{x}{L}} + \frac{\partial C_i(\eta)}{\partial \eta} \sqrt{\frac{L}{x}} \right) \frac{\partial \eta}{\partial x} \\
&= A_{1i}(\eta) + B_{1i}(\eta)\sqrt{\frac{x}{L}} + C_{1i}(\eta)\sqrt{\frac{L}{x}} + D_{1i}\frac{\sqrt{L}}{x^{3/2}} \quad (5.36)
\end{aligned}$$

where α has value 0° for quadrilateral elements where quadrilateral sides having quarter-point nodes are parallel to the direction of crack propagation. For triangular elements at the crack vertex in the modelled geometry, α represents the angle made by the ray joining the field point to the crack vertex with the direction of crack propagation. Here, the term containing $\sqrt{\frac{L}{x}}$ is integrated by Gauss-Jacobi integration rules. The term containing $\frac{1}{x^{3/2}}$ requires finite-part integration. Integration is performed in extrinsic polar coordinates ρ and θ and is treated as follows:

$$\begin{aligned} \int \int F(\rho, \theta) \frac{\sqrt{L}}{x^{3/2}} \rho d\rho d\theta &= \int \int (F(\rho(\xi, \eta), \theta(\xi, \eta)) - F_o(\xi = -1, \eta)) \frac{\sqrt{L}}{x^{3/2}} \rho d\rho d\theta \\ &+ \int_{-1}^1 J(\eta) F_o(\xi = -1, \eta) \int_0^L \frac{\sqrt{L}}{x^{3/2}} dx d\eta \end{aligned} \quad (5.37)$$

where $J(\eta)$ is the Jacobian for mapping of the element edge along the crack front to intrinsic coordinates $\eta = -1$ to 1 . Here, L and x can be written in terms of ρ and θ for straight-edge elements in the form $(a(\theta)\rho + b(\theta))$. First integral on the right hand side can now be calculated by Gauss-Jacobi integration rules. And the second integral on the right hand side is written as

$$\int_{-1}^1 J(\eta) F_o(\xi = -1, \eta) \int_0^L \frac{\sqrt{L}}{x^{3/2}} dx d\eta = \sum_i w_i J(\eta_i) F_o(\xi = -1, \eta = \eta_i) \text{F.P.} \int_0^L \frac{\sqrt{L}}{x^{3/2}} dx$$

And

$$\text{F.P.} \int_0^L \frac{\sqrt{L}}{x^{3/2}} dx = -2 \quad (5.38)$$

5.8 Results and Discussion

Elastic analysis of a running crack subjected to uniform step pressure on crack faces has been performed for this work. Fig. 5.4 shows the geometry of the center crack specimen used in the numerical analysis. The specimen has the parameters: $a = 0.24$ cm, $w = 1$ cm, $h = 1$ cm and $b = 0.21$ cm where a is the crack half-length, w is specimen half-width, h is half-height and b is specimen half-thickness. The material is assumed to be linear elastic with properties as: shear modulus $\mu = 90$ GPa, Poisson's ratio $\nu = 0.3$ and density $\rho = 7800$ kg/m³. Hence, $c_1 = 6354$ m/s and $c_2 = 3396$ m/s. The center crack specimen is loaded by suddenly applied uniform normal pressure to crack faces $\sigma_{yy}(t) = -\sigma_o H(t)$. This problem was solved analytically by Freund [11] for a semi-infinite crack in an unbounded domain. Analytical solution [11] is valid until unloading waves from the free boundary or

waves diffracted from the other crack tip reach the crack tip under consideration. Influence of three-dimensional effects on DSIF along the crack front is studied in the present work.

Due to the symmetry in the specimen geometry and loading, only one-eighth of the specimen is modelled in the boundary element analysis. Fig. 4.3 shows the boundary-element idealization of one-eighth of the center-crack specimen. Eight-node quadrilateral elements are used. A combination of continuous and discontinuous elements is used to reduce the overall degrees of freedom. The eight-node elements bordering the crack on the side of the crack surface are quarter-point elements, while the ones on the opposite side, i.e., ahead of the crack front are quarter-point, traction-singular elements. Triangular elements (collapsed eight-noded elements) are used to surround the intersection point of the crack front with the lateral facets. These triangular elements are modelled as quarter-point, traction-singular elements.

Appropriate boundary conditions are applied to the symmetry planes. This is done by restraining nodal displacements in the direction normal to the plane or planes of symmetry to which the node belongs. The nodes on the crack surface, except for those directly on the crack front or on the edges with lateral facets, are left free to move in three orthogonal directions.

Table 5.2 shows details of the mesh used for boundary element analysis. The mesh has 1994 nodes, 620 elements and 5982 degrees of freedom. It has 12 layers of elements on the face having the crack. The thicknesses of different layers after normalization with half-crack length are .008,.008,.016,.024,.032,.048,.104,.12, .12,.12,.12 and .12 respectively. Various three-dimensional aspects of fracture characteristics of a through thickness center crack in a plate under step loading on crack faces are enumerated as follows:

1. **Weaker singularity at the crack vertex for Mode-I loading at low crack speeds:** Fig. 5.5 shows the DSIF variation with time for the case of a stationary crack under suddenly applied crack face pressure. The plot clearly shows the influence of lower stress singularity at crack vertex resulting in lower DSIF values at the crack vertex. At the crack vertex for a stationary crack, the stress singularity is known to be weaker than square-root. In these plots, $z/b = 0.0$ denotes the free surface position along the crack front and $z/b = 1.0$ denotes the mid-surface position.

Figs. 5.6,5.7 show the computed values of normalized Mode-I DSIF versus normalized time for crack propagation velocities $v = 0.2c_R$ and $0.4c_R$, respectively. The boundary element results are compared with analytical solutions for $0.2c_R$ and $0.4c_R$, denoted in the figures by dotted lines. It can be seen from the figures that the

agreement between the boundary element mid-surface DSIF values and plane-strain analytical results is quite good for $v = 0.2c_R$. The mid-surface curve for $v = 0.4c_R$ lies quite below the plane strain analytical curve. This reflects the effect of loss of dominance of square-root singularity at high speeds of crack propagation. The analytical solutions are for the case of half-plane crack propagating in an unbounded domain under the action of suddenly applied uniform normal pressure acting on the crack faces as discussed in section 5.2.

For a running crack, reduction in value of DSIF at crack vertex is noticed at low crack speeds (Figs. 5.6,5.7). At crack vertex, value of DSIF is lower than the rest of the crack front for $v/c_R = 0.2$ and 0.4 . But this behaviour changes at speeds beyond $v/c_R = 0.4$ (Figs. 5.8,5.9). For higher crack speeds, DSIF value at crack vertex becomes higher than the rest of crack front. This may be the result of greater erosion of dominance of square-root singularity along the crack front inside the specimen rather than near the crack vertex at higher speeds of crack propagation. Also this implies that free surface retardation of crack front would not occur at high crack speeds. This result is in tune with experimental observations where at high crack speeds, straight crack front is observed. Ravi-Chandar and Knauss [38] explained that there is no longer a single crack front, but an ensemble of cracks propagating along the apparent crack front.

Figs. 5.10,5.11 show plots of DSIF along the crack front at various instants of time for two different crack velocities respectively. It is seen that the curves have oscillations in their values along the crack front. Mid-side nodes have lower values of DSIF than corner nodes of elements on crack front. This may be a result of sensitivity of boundary element method to spatial instability [101], which is manifesting itself in crack propagation problems. Figs. 5.12,5.13 show DSIF variation along crack front by considering tractions at either corner or mid-side nodes for DSIF computations respectively. These plots clearly show increased DSIF value at crack vertex for crack speed of $v/c_R = 0.8$.

Again, Figs. 5.14,5.15 show the variation of DSIF with time at the crack vertex and mid-surface respectively for time step $c_1\Delta T/h = 0.06354$ for different crack speeds. Figs. 5.16,5.17 show the same plots for a reduced time step size $c_1\Delta T/h = 0.015885$. It is clearly seen that around or beyond $v/c_R = 0.4$, free surface values of DSIF are higher than mid-surface values, implying that there will be no crack retardation at free surface at speeds beyond $v/c_R = 0.4$. The results seem to indicate that that be-

yond a certain crack velocity, crack behaviour undergoes a distinct change or inertial terms start dominating the square-root singular terms. Parton [37] experimentally observed that if crack velocity exceeds a certain value, then the arrival of waves reflected from the free boundaries to the crack tip does not affect its velocity, implying that the zone of process occurrence has a certain inertia, i.e., it shows some resistance to the 'attempts' to change its velocity. So crack speed $v = 0.4c_R$ appears to be the 'critical' speed beyond which behaviour at crack vertex gets reversed. The value of DSIF at crack vertex becomes higher than the rest of the crack front, just opposite to the behaviour for a stationary or low speed crack.

Another observation, worth noting, from these figures is that stationary part of DSIF curves are much below the stationary analytical solution for smaller time step plots. This concurs with the conclusion of Ma and Freund [40] that time is needed for the stress intensity factor controlled field (K_I^d -dominant field) to be fully established. This shows that DSIF values computed from boundary element analysis are sensitive to loss of square-root dominance in transient analysis.

2. **Effects of crack tip tunnelling:** Through-thickness fatigue cracks in plate geometries almost always show crack front tunnelling, i.e., a curved crack front with the the point of maximum length of the crack at the center. It is also observed that fatigue crack fronts penetrate the free surface at a non-zero angle with the normal to the free surface. Bazant and Estenssoro [2] argued that this angle is fixed by the angle at which the square-root singularity of stresses and strains at the free surface penetration is restored. They showed that the front edge of a planar Mode-I crack that propagates in an elastic isotropic plate in a plane normal to the plate surfaces must terminate at the surfaces with a certain angle β (Fig. 5.18) depending only on Poisson's ratio ν . Tests were carried out by Rolfe and Barsom [5] on structural steel in static loading according to E-399 ASTM Standard. Their test results showed that theoretical lines of inclination $\beta = 101^\circ$ with the plate surface agreed very well with the observed terminal directions of the first arrest marks, which corresponded to an essentially elastic fracture stage. Gudmundson and Östlund [3] found that a weaker singularity exists at the corner point for a dynamically growing crack and estimated the critical angle to be 101° almost independent of crack velocity. These studies were conducted using a local analysis for quarter-plane crack in a semi-infinite half-space subjected to symmetric loading. The present study deals with the analysis of a center crack finite solid under suddenly applied uniform normal pressure to crack faces.

In the present study, calculations on tunnelling crack fronts are performed using circular crack fronts with different penetration angles, viz., 95° , 98° , 101° , 105° and 110° using a mesh similar to that of Table 5.2. Also in the present study, mesh is not orthogonal at the crack front, i.e., crack tip elements are not oriented normally to the crack front. The self-similar crack growth direction is taken as parallel to the free surface, rather than normal to the crack front (Fig. 5.18). Burton *et al.* [4] also advanced crack front parallel to the free surface to produce a crack that retains its shape during propagation.

Fig. 5.19 shows a comparison of the calculated crack-vertex $K_I(t)$ distributions for different penetration angles for an example case of crack speed $v = 0.4c_R$. It is seen that DSIF at crack vertex increases with increase in intersection angle. Values of $K_I(t)$ are calculated from crack tip tractions. The modelled crack front is not smooth but is made of small straight line segments. For correct interpolation of traction singularity in crack tip elements in BEM, a restriction is imposed on the positions of nodes in the elements requiring that element edge on the crack front be straight [81]. Fig. 5.20 shows the plots of $K_I(t)$ for different crack front intersection angles at the mid-surface position. It is seen that free surface DSIF is greater than mid-surface DSIF for intersection angles of 101° and higher. At mid-surface, DSIF decreases with increase in intersection angle. For intersection angle of 101° , Fig. 5.21 shows that DSIF at crack vertex is higher than DSIF of inner layers implying that crack front has become critical at the corner point where crack front meets the free surface. Thus critical intersection angle can be assessed accurately for finite domains with time-domain BEM.

5.9 Conclusions

1. Time-domain 3-D BEM is implemented for studying influence of free-surface on DSIF in a center-crack specimen under suddenly applied uniform pressure to crack faces. This work shows the efficacy of BEM and DSIF calculated from nodal traction values in studying three-dimensional aspects in crack/surface intersection problems for impact loading.
2. A moving mesh procedure is proposed and implemented for 3-D time-domain displacement boundary element analysis.

3. Lower values of DSIF are found at corner point for Mode-I loading for low speeds of crack propagation, confirming the existence of lower singularity in stresses at corner point. But at crack speeds beyond $v = 0.4c_R$, higher values of DSIF are computed compared to the rest of the crack front. The study correctly predicts that for high speeds of crack propagation, crack front maintains its straight profile.
4. Values of DSIF calculated from nodal tractions at crack front show sensitivity to loss of square-root dominance in transient fields.
5. It is possible to estimate the intersection angle at which the DSIF at the crack vertex is equal to or higher than DSIF of inner layers. So the intersection angle at which free surface vertex point becomes critical along with other parts of the crack front is estimated. Values of $K_I(t)$ at crack vertex are seen to be higher than values of $K_I(t)$ at inner layers for crack intersection angles of 101° and above, implying that crack has become critical at the vertex for intersection angles of 101° .

Table 5.1: Values of the Freund [11,12] slowness function $S_+(1/v)$ for various crack speeds v for Poisson ratio $\nu = 0.3$

v/c_R	$S_+(1/v)$	$k(v)$
0.2	0.96032	0.87766
0.4	0.90746	0.73836
0.5	0.90746	0.65976
0.6	0.90746	0.57280
0.8	0.71753	0.35859

Table 5.2: Mesh characteristics for Mode-I runs with straight crack front.

Mesh no.	b/w	crack tip element size ($\Delta l/a$)	free surface element size ($\Delta z/a$)	size of regular elements (size/clear distance to crack-tip) (on face having crack)	No. of elements	time step $c_1 \Delta T/h$
1	.21	0.1	0.008	0.5	620	0.06354

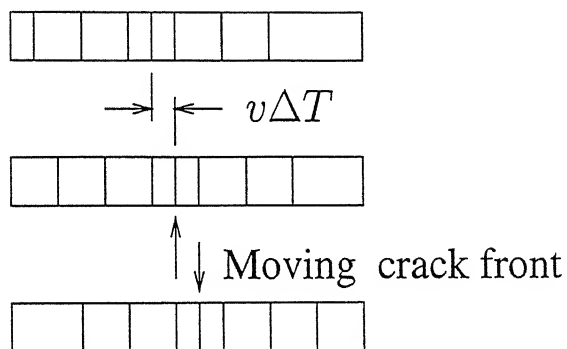


Figure 5.1: Movement of the elements

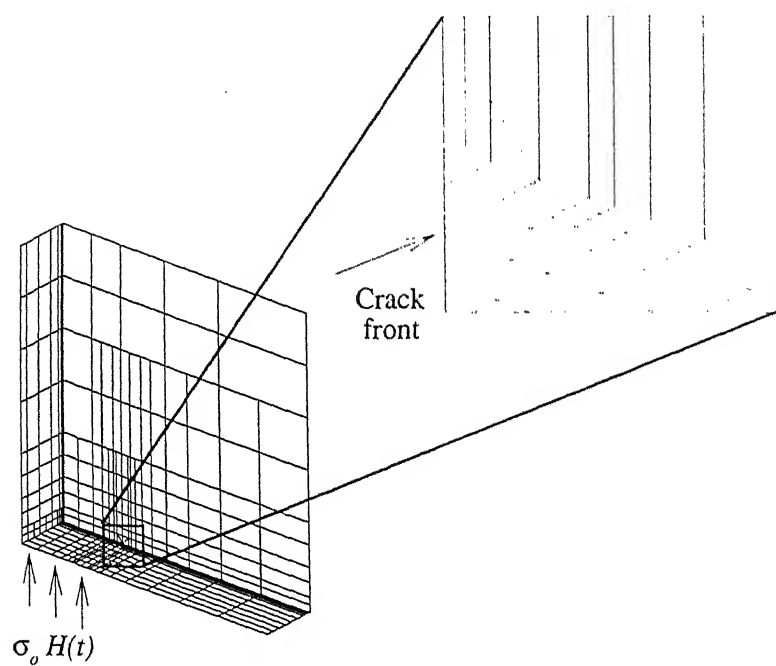


Figure 5.2: Boundary Element Mesh

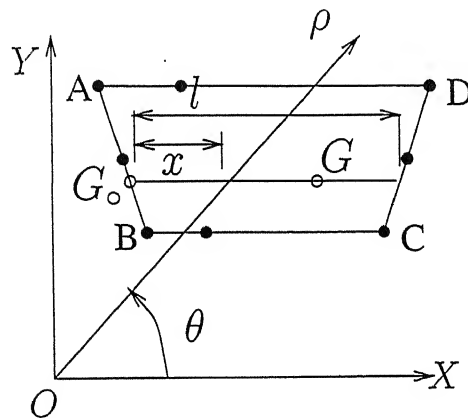


Figure 5.3: Quarter-point element projected in the plane tangent to the nearest node.

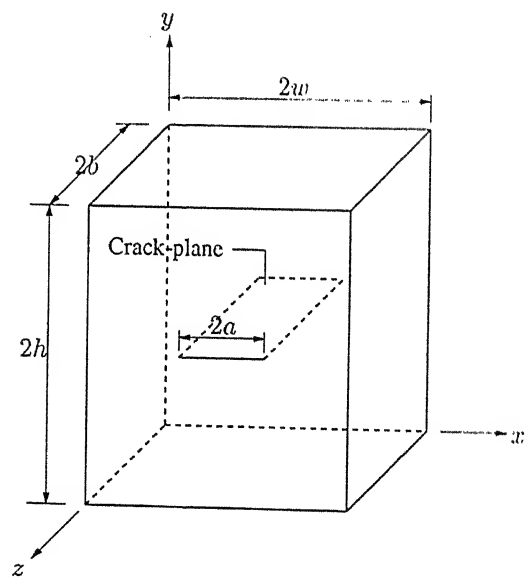


Figure 5.4: Center-crack specimen

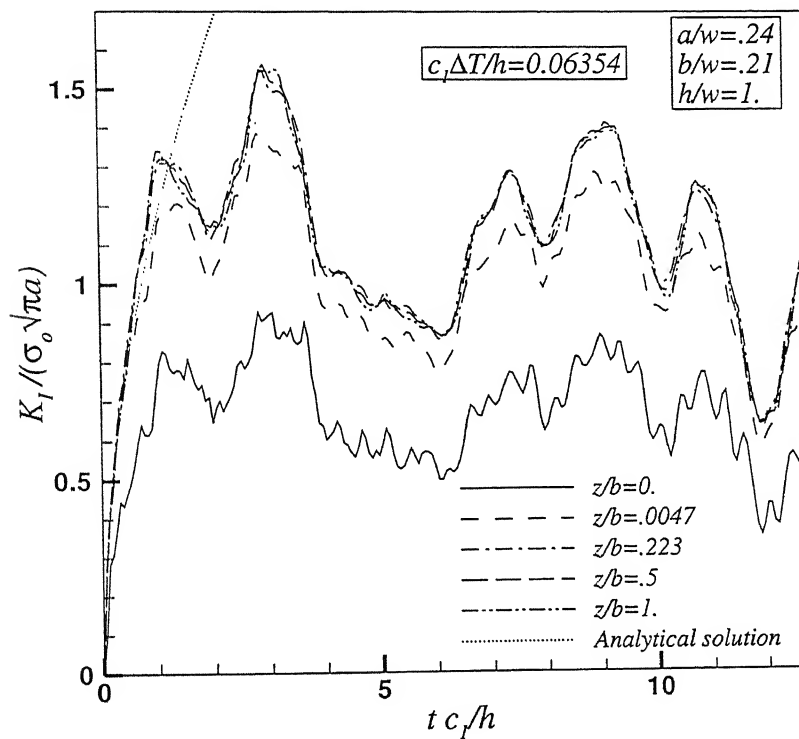


Figure 5.5: Plots of $K_I(t)$ at different positions on crack front for suddenly applied crack face pressure and comparison with analytical solution of problem of semi-infinite crack in an unbounded body

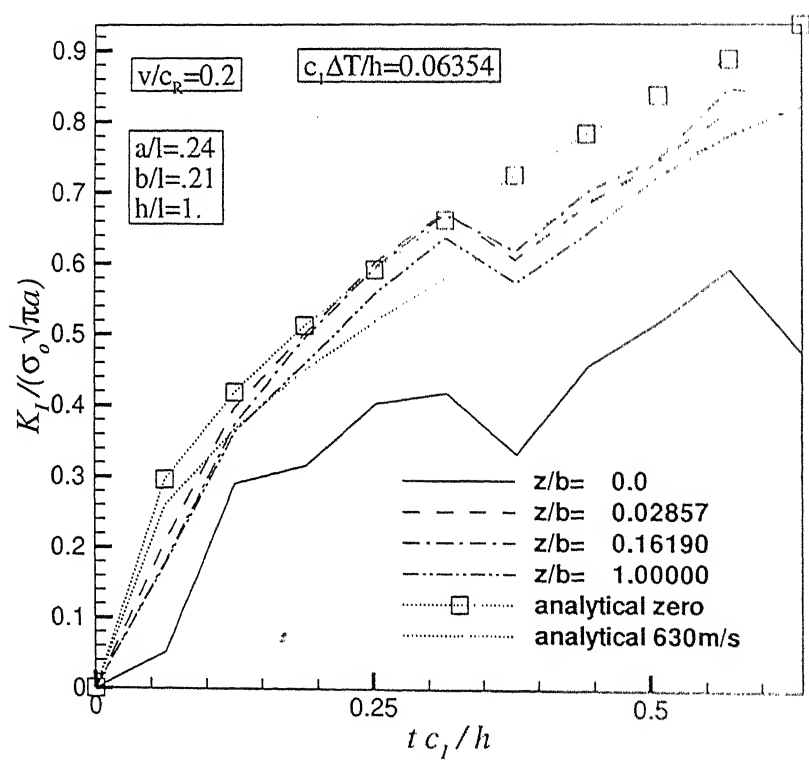


Figure 5.6: DSIF variation with time for different positions along the crack front for $v/c_R = 0.2$ (delay time $c_I \tau / h = 0.3177$)

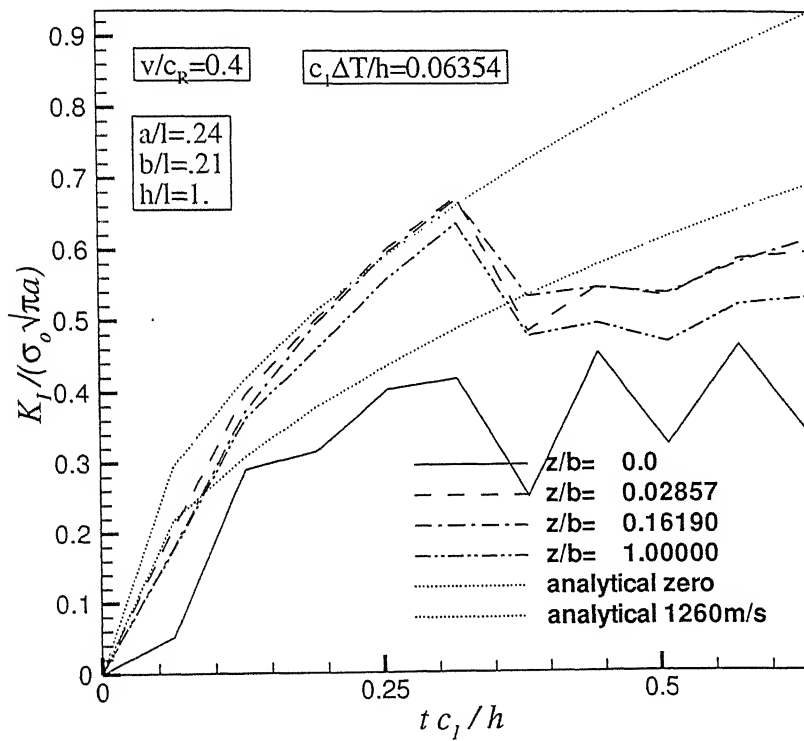


Figure 5.7: DSIF variation with time for different positions along the crack front for $v/c_R = 0.4$ (delay time $c_I \tau/h = 0.3177$)

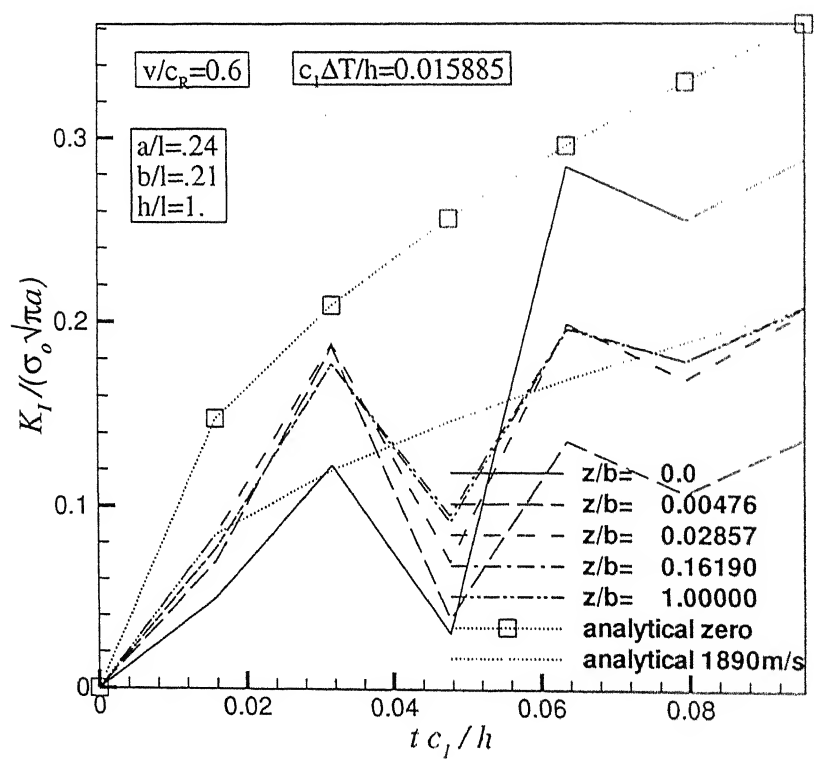


Figure 5.8: DSIF variation with time for different positions along the crack front for $v/c_R = 0.6$ (delay time $c_1 \tau / h = 0.03177$)

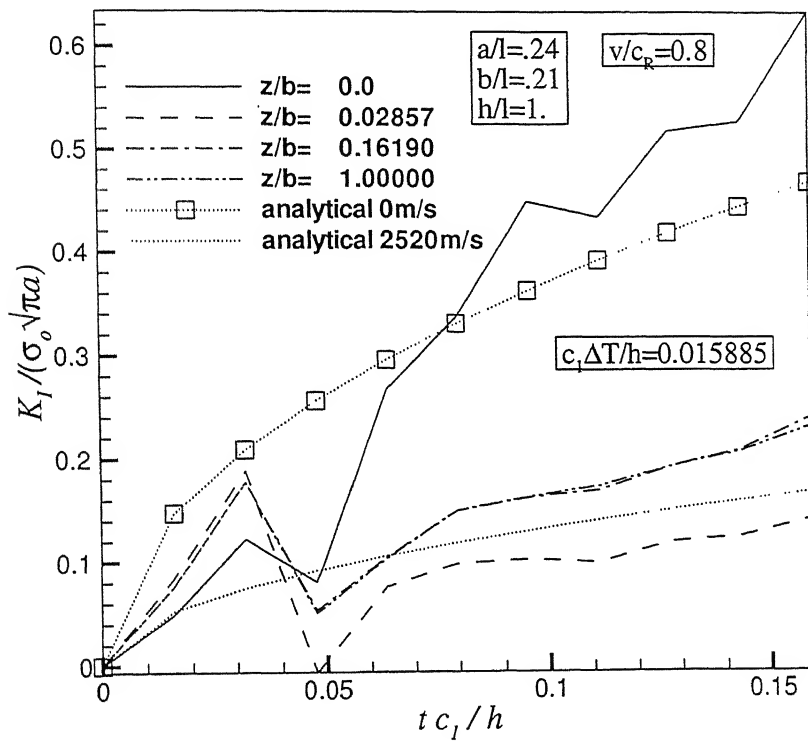


Figure 5.9: DSIF variation with time for different positions along the crack front for $v/c_R = 0.8$ (delay time $c_1 \tau / h = 0.03177$)

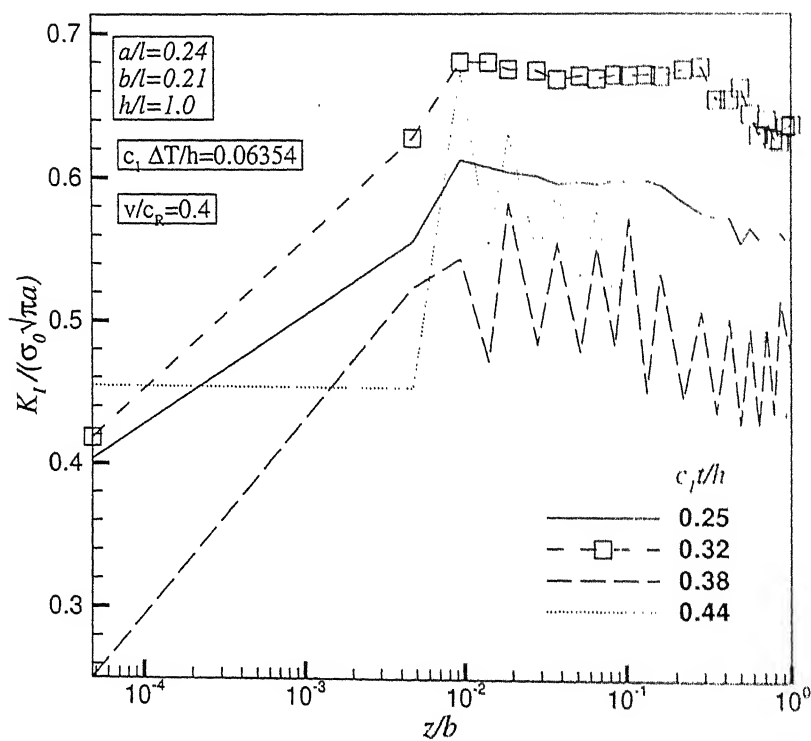


Figure 5.10: DSIF variation along the crack front for different instants of time for $v/c_R = 0.4$ (delay time $c_1 \tau/h = 0.032$)

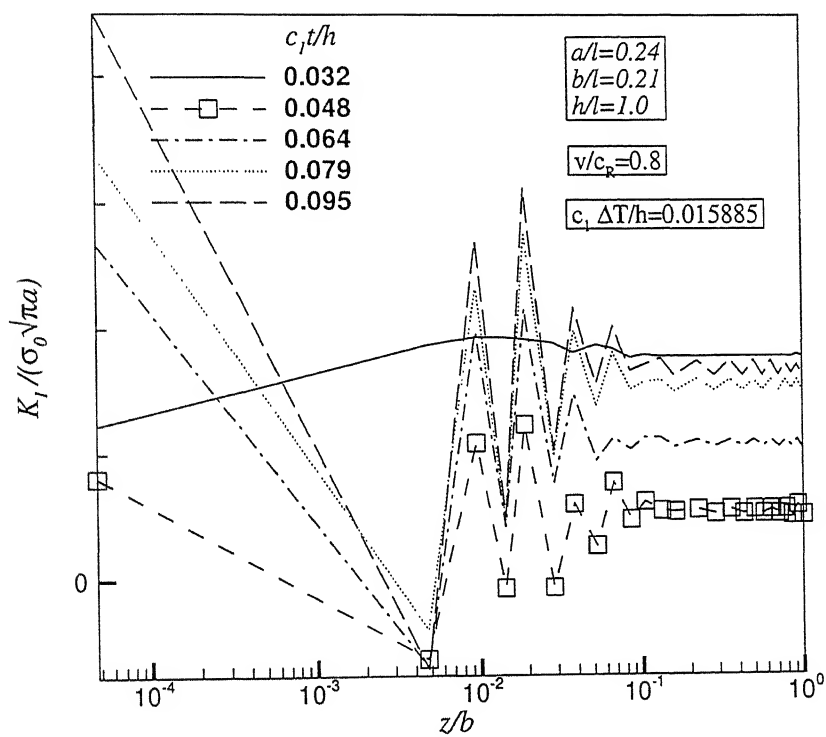


Figure 5.11: DSIF variation along the crack front for different instants of time for $v/c_R = 0.8$ (delay time $c_1 \tau/h = 0.032$)

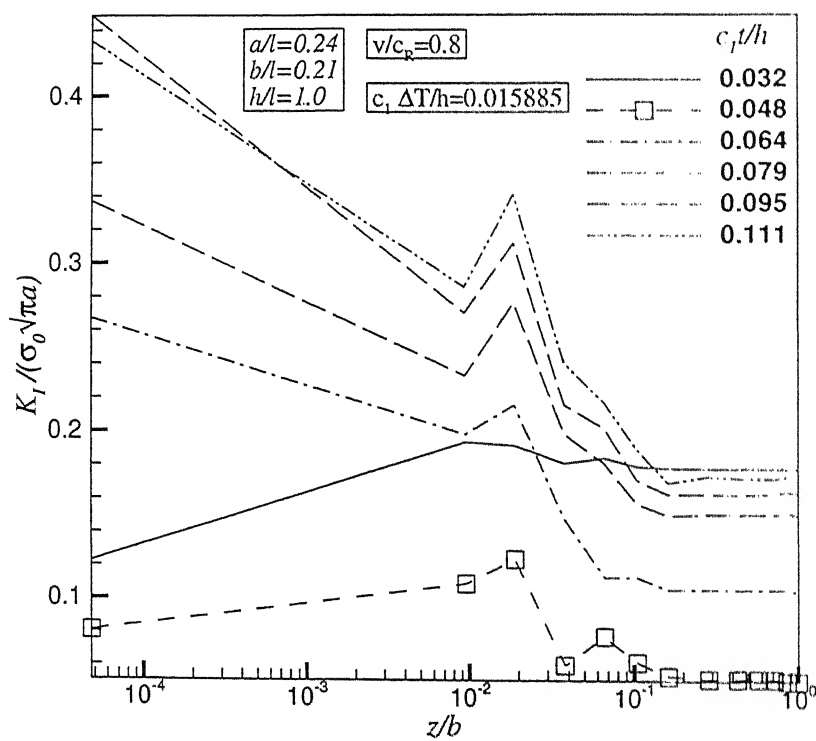


Figure 5.12: DSIF variation along the crack front for different instants of time for $v/c_R = 0.8$, using only DSIF values at corner nodes of the elements on crack front

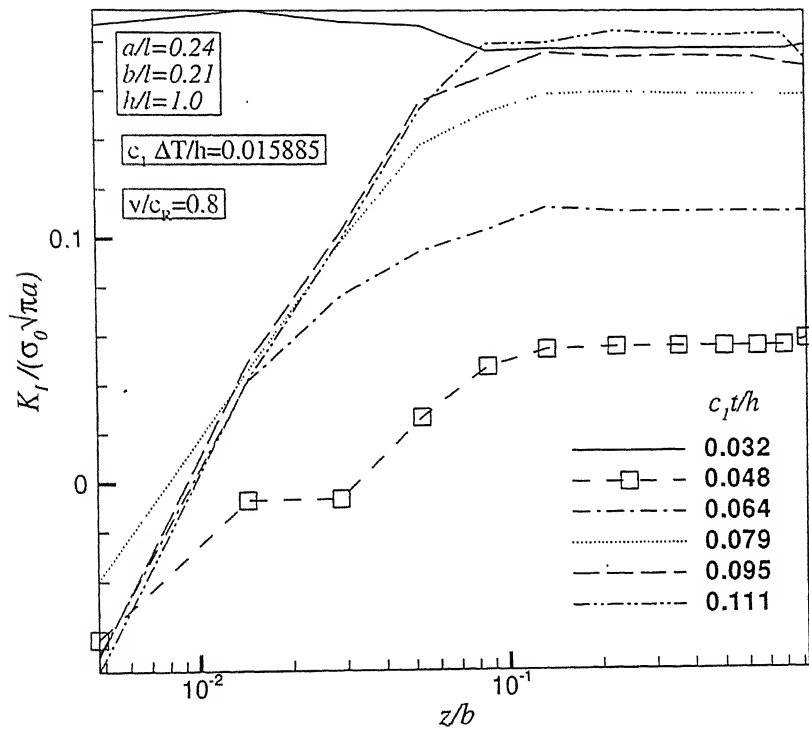


Figure 5.13: DSIF variation along the crack front for different instants of time for $v/c_R = 0.8$, using only DSIF values at mid-side nodes of the elements on crack front

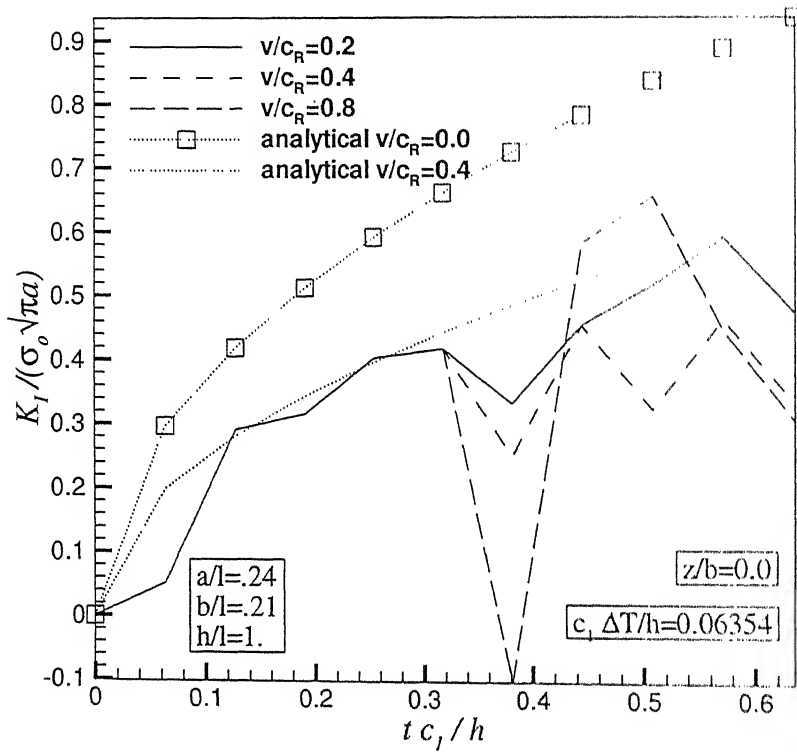


Figure 5.14: DSIF variation with time at crack vertex for different speeds of crack propagation (delay time $c_1 \tau / h = 0.3177$)

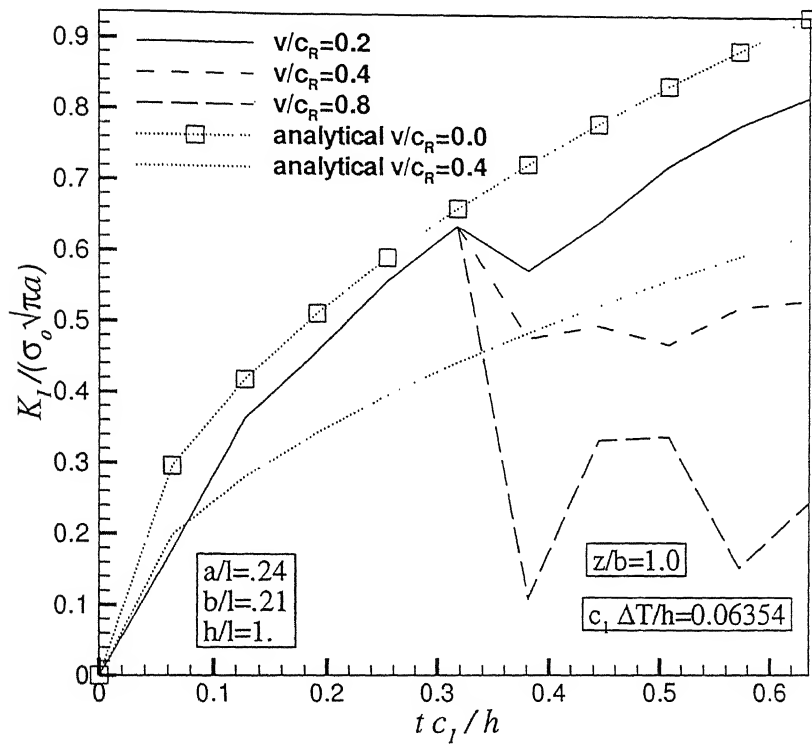


Figure 5.15: DSIF variation with time at mid-surface for different speeds of crack propagation (delay time $c_I \tau / h = 0.3177$)

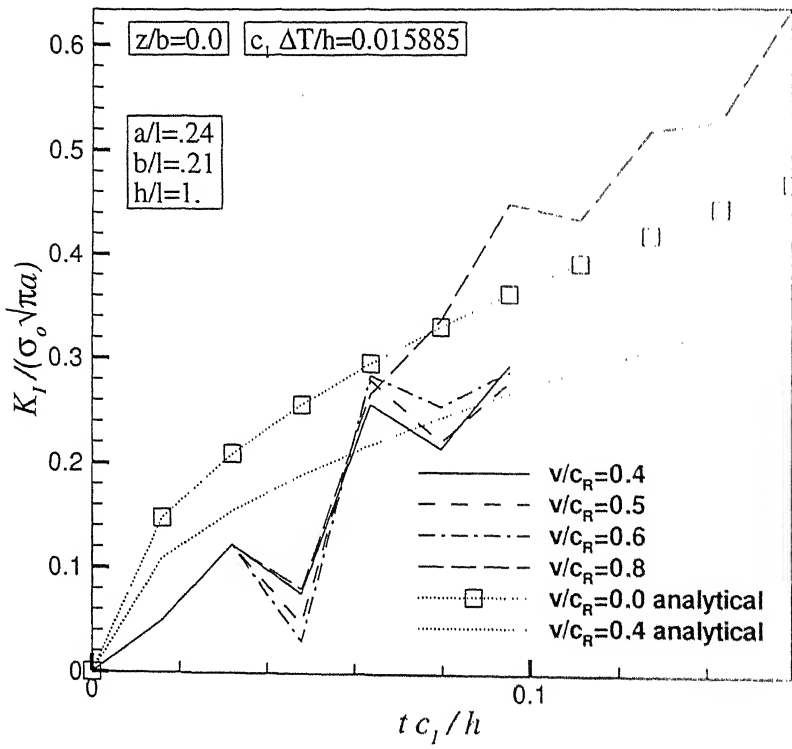


Figure 5.16: DSIF variation with time at crack vertex for different speeds of crack propagation (delay time $c_1 \tau / h = 0.03177$)

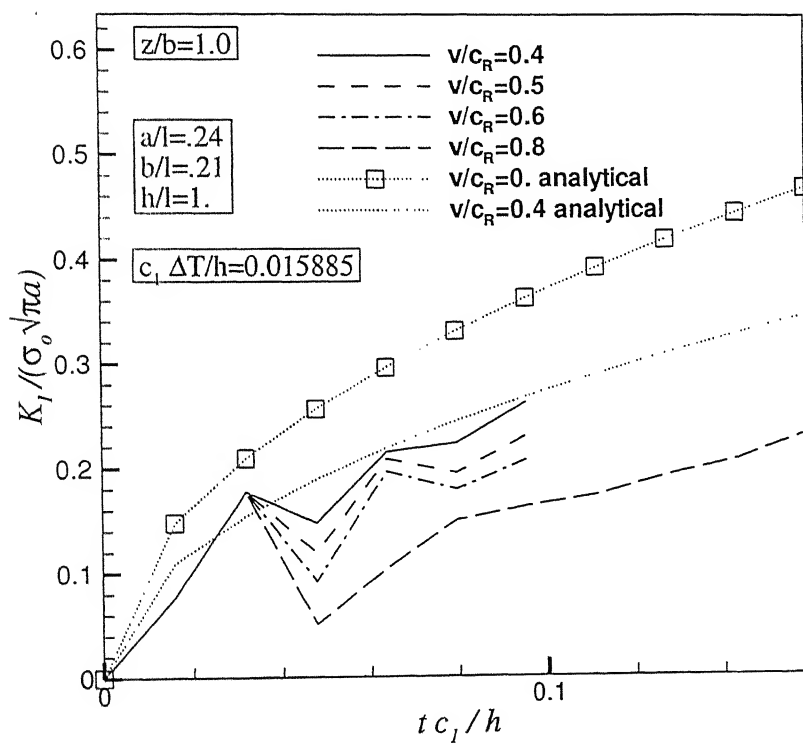


Figure 5.17: DSIF variation with time at mid-surface for different speeds of crack propagation (delay time $c_I \tau/h = 0.03177$)

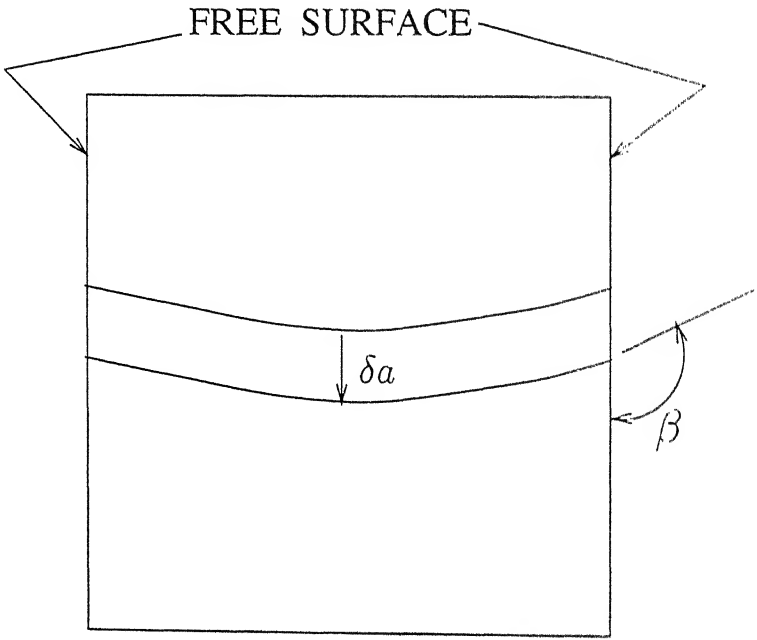


Figure 5.18: Direction of crack advance parallel to free surface to achieve self-similar profile

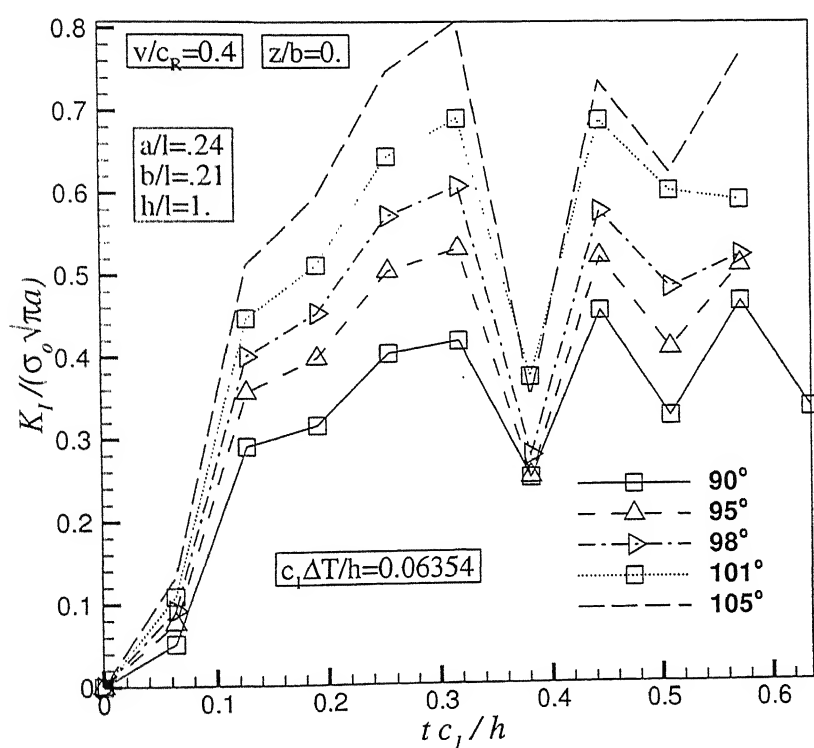


Figure 5.19: Plots of $K_I(t)$ at crack vertex for different intersection angles of crack front with free surface (delay time $c_1 \tau / h = 0.3177$)

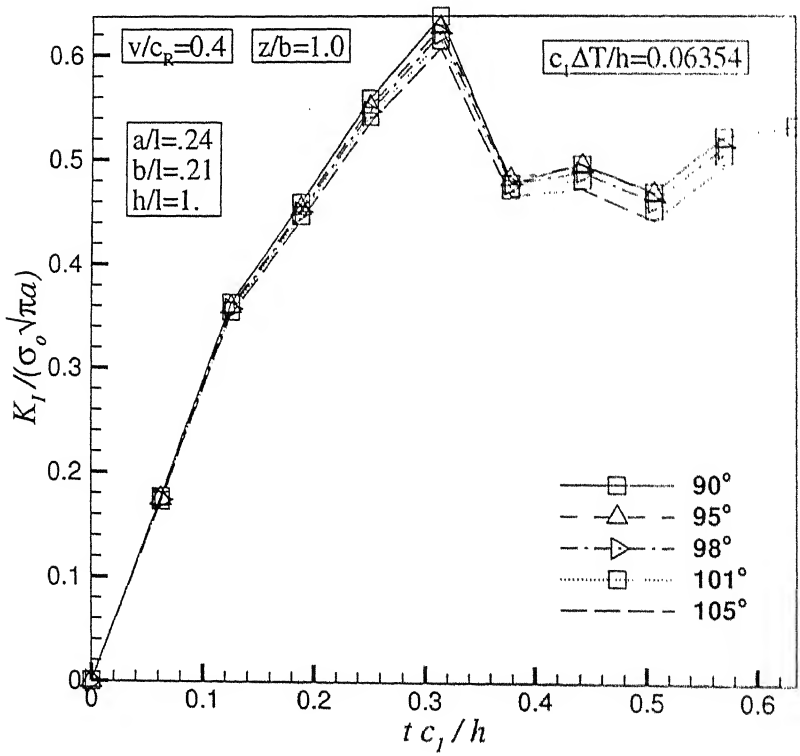


Figure 5.20: Plots of $K_I(t)$ at mid-surface position for different intersection angles of crack front with free surface (delay time $c_I \tau / h = 0.3177$)

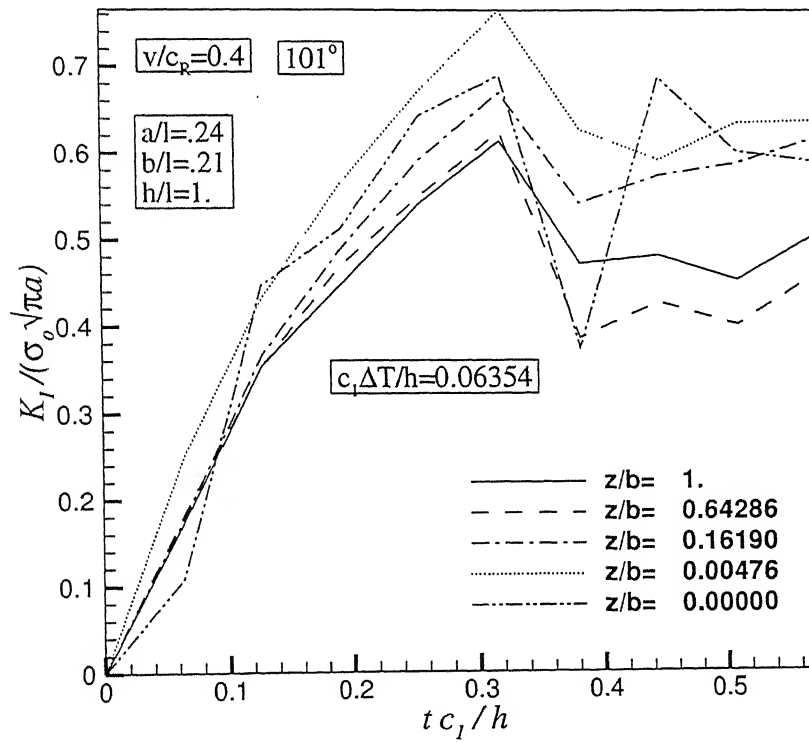


Figure 5.21: Plots of $K_I(t)$ with time for different positions along crack front for intersection angle of 101° (delay time $c_I \tau / h = 0.3177$)

Chapter 6

Conclusions and Future Directions

This chapter summarises this thesis, and will set forth goals for future work.

6.1 Conclusions

In this work, the effect of free surfaces on fracture characteristics for elastostatic and elastodynamic problems has been investigated using three-dimensional boundary element method. Free surface effect has been studied for a through center cracked finite body for three situations: quasi-static conditions, stationary crack under impact loading and running crack under impact loading.

For finite geometries, finite element analysis is not able to obtain an accurate stress state adjacent to the crack tip in the region close to the free surface. The problems of brittle fracture involving intersection of the crack fronts with the free surfaces still requires extremely careful examination. The BEM has special suitability for problems of fracture mechanics. Its capability to accurately model steep stress gradients is the main motivation for its use in this study to analyse free surface effect for through cracks.

Stress intensity factors from a boundary element analysis can be directly calculated from values of tractions at nodes on the crack front. Values of J_1^n integral calculated along the crack front correspond well with the K_I values calculated from nodal traction values in quasi-static analysis. Thus, it is possible to relate the evaluated state of stress at the crack vertex, where crack front meets the free surface, with a value of SIF. This SIF value reflects the influence of the exponent of singularity existing at the crack vertex. A lower value of SIF is computed for a weaker singularity at the vertex and a higher value of SIF is computed for a stronger singularity at the vertex. For the same level of mesh refinement, value of SIF is seen to be sensitive to change in singularity of stresses at the vertex brought

about by changes in either Poisson's ratio of the material or intersection angle of the crack front with the free surface. It becomes possible to estimate the intersection angle at which the SIF at the crack vertex is equal to or higher than mid-surface SIF value. So the intersection angle at which free surface vertex point becomes critical along with other parts of the crack front gets estimated.

Values of DSIF calculated from nodal tractions at crack front show sensitivity to loss of square-root dominance in transient fields. Lower values of DSIF are found at corner point for Mode-I loading for low speeds of crack propagation, confirming the existence of lower singularity in stresses at corner point. But at crack speeds beyond $v = 0.4c_R$, higher values of DSIF are computed compared to the rest of the crack front. The study correctly predicts that for high speeds of crack propagation, crack front maintains its straight profile.

It should become possible to capture free surface retardation of crack growth accurately in different crack propagation problems with the methodology used in this paper for both static and dynamic conditions.

6.2 Future Directions

The presented methodology may be further tested on actual crack propagation problems. In this study, only self-similar crack propagation was considered. The presented methodology may be used to resolve the question of uniqueness of relationship between K_I^d and v in high speed crack propagation experiments and simulations. For dynamic problems, dynamic J -integral may be computed and its correspondence with DSIF values computed from nodal tractions on crack front verified. The work can be easily extended to study free surface effect for interfacial cracks.

References

- [1] Benthem J.P. State of stress at the vertex of a quarter-infinite crack in a half-space. *International Journal of Solids and Structures*, 13:479–492, 1977.
- [2] Bažant Z.P., Estenssoro L.F. Surface singularity and crack propagation. *International Journal of Solids and Structures*, 15:405–426, 1979.
- [3] Gudmundson P., Östlund S. Stress singularity at the free surface of a dynamically growing crack. *ASME Journal of Applied Mechanics*, 57:112–116, 1990.
- [4] Burton W.S., Sinclair G.B., Solecki J.S., Swedlow J.L. On the implications for LEFM of the three-dimensional aspects in some crack/surface intersection problems. *International Journal of Fracture*, 25:3–32, 1984.
- [5] Rolfe S.T., Barsom J.M. *Fracture and fatigue control in structures*. Prentice Hall, Englewood Cliffs, New Jersey, 1977.
- [6] Lin X.B., Smith R.A. Finite element modelling of fatigue crack growth of surface cracked plates part I : The numerical technique. *Engineering Fracture Mechanics*, 63:503–522, 1999.
- [7] Guiggiani M., Gigante A. A general algorithm for multidimensional Cauchy principal value integrals in the boundary element method. *ASME Journal of Applied Mechanics*, 57:906–915, 1990.
- [8] Cruse T.A., Aithal R. Non-singular boundary integral equation implementation. *International Journal for Numerical Methods in Engineering*, 36:237–254, 1993.
- [9] Mi Y., Aliabadi M. H. Semi-analytical integration method for 3-D near-hypersingular integrals. In *Boundary Element Method XVI, Proc. of 16th Int. Conf. on BEM*, ed. C. A. Brebbia, Computational Mechanics Publications, Southampton, pages 423–429, 1994.
- [10] R. Gallego, J. Domínguez. Dynamic crack propagation analysis by moving singular boundary elements. *ASME Journal of Applied Mechanics*, 59:S158–S162, 1992.
- [11] Freund L. B. Crack propagation in an elastic solid subject to general loading, I, constant rate of extension, II, non-uniform rate of extension. *Journal of the Mechanics and Physics of Solids*, 20:129–140, 141–152, 1972.
- [12] Freund L. B. *Dynamic Fracture Mechanics*. Cambridge University Press, Cambridge, 1990.

- [13] Sternberg E., Sadowsky M.A. Three-dimensional solution for the stress concentration around a circular hole in a plate of arbitrary thickness. *ASME Journal of Applied Mechanics*, pages 27–38, 1949.
- [14] Hartranft R. J., Sih G. C. An approximate three-dimensional theory of plates with application to crack problems. *International Journal of Engineering Science*, 8:711–729, 1970.
- [15] Yang W., Freund L.B. Transverse shear effects for through-cracks in an elastic plate. *International Journal of Solids and Structures*, 1985.
- [16] Rosakis A. J., Ravi-Chandar K. On crack-tip stress state: An experimental evaluation of three-dimensional effects. *International Journal of Solids and Structures*, 22(2):121–134, 1986.
- [17] Nakamura T., Parks D.M. Three-dimensional stress field near the crack front of a thin elastic plate. *ASME Journal of Applied Mechanics*, 55:805–813, 1988.
- [18] Bakker A. Three-dimensional constraint effects on stress intensity distributions in plate geometries with through-thickness cracks. *Fatigue Fracture Engineering Materials and Structures*, 15(11):1051–1069, 1992.
- [19] Smith C. W. Analytical and experimental studies of the surface flaw. *Experimental mechanics*, pages 194–200, 1988.
- [20] Broek D. *Elementary Engineering Fracture Mechanics*. Martinus Nijhoff, London, 1982.
- [21] Kanninen M.F., Popelar C.H. *Advanced fracture mechanics*. Oxford university press, Oxford, 1985.
- [22] Cherepanov G.P. *Mechanics of brittle fracture*, translated by R. de Wit and W. C. Cooley. McGraw-Hill, New York, 1979.
- [23] Hellan K. *Introduction to fracture mechanics*. McGraw-Hill, New York, 1984.
- [24] P. Kumar. *Elements of fracture mechanics*. Wheeler Publishing, New Delhi, 1999.
- [25] Knott J.F. *Fundamentals of fracture mechanics*. Butterworth, London, 1979.
- [26] Lawn B.R. *Fracture of brittle solids, 2nd edition*. Cambridge University Press, Cambridge, 1993.
- [27] Barsom J. M., Rolfe S. T. *Fracture and fatigue control of structures, 2nd edition*. Prentice-Hall, Englewood Cliffs, New Jersey, 1987.
- [28] Griffith A. A. The phenomenon of rupture and flow in solids. *Phil. Trans. Roy. Soc. Lond.*, A221:163, 1920.
- [29] Irwin G. R. Fracture dynamics. In *Fracturing of metals*. ASM publ., 147–166, 1948.
- [30] Orowan E. Energy criteria of fracture. *Welding journal*, 34:157–160, 1955.
- [31] Irwin G. R. *ASME Journal of Applied Mechanics*, 24:361, 1957.

- [32] Rice J. R. Mathematical analysis in the mechanism of fracture. In *Fracture*, ed. H. Liebowitz, vol. 2, chapter 3. Academic Press, New York, 1968.
- [33] Z. Parton V., G. Boriskovsky V. *Dynamic Fracture Mechanics Volume 1: Stationary Cracks*. Hemisphere Publishing Corporation, New York, 1989.
- [34] Z. Parton V., G. Boriskovsky V. *Dynamic Fracture Mechanics Volume 2: Propagating Cracks*. Hemisphere Publishing Corporation, New York, 1990.
- [35] Broberg K. B. *Cracks and fracture*. Cambridge University Press, Cambridge, 1999.
- [36] Freund L. B. Crack propagation in an elastic solid subjected to general loading. III. stress wave loading. *Journal of the Mechanics and Physics of Solids*, 21:47–61, 1973.
- [37] Parton V. Z. *Fracture mechanics from theory to practice*. Gordon and Breach Science Publishers, Philadelphia, 1992.
- [38] Ravi-Chandar K., Knauss W. G. An experimental investigation into dynamic fracture: II. microstructural aspects. *International Journal of Fracture*, 26:65–80, 1984.
- [39] Ravi-Chandar K., Knauss W. G. An experimental investigation into the mechanics of dynamic fracture: I. crack initiation and arrest. *International Journal of Fracture*, 25:247–262, 1984.
- [40] Ma C.C, Freund L.B. The extent of the stress intensity factor field during crack growth under dynamic loading conditions. *ASME Journal of Applied Mechanics*, 53:303–310, 1986.
- [41] Freund L. B., Rosakis A. J. The structure of the near-tip field during transient elastodynamic crack growth. *Journal of the Mechanics and Physics of Solids*, 40(3):699–719, 1992.
- [42] Kobayashi J. W. Dynamic photo-elastic determination of the $\dot{a} - k$ relation for the 4340 steel. In *Crack Arrest methodology and applications*, edited by Hahn, G. T., et al. , ASTM STP 711, pp.189–210. 1980.
- [43] Rosakis A. J., Duffy J., Freund L. B. The determination of dynamic fracture toughness of AISI 4340 steel by the shadow spot method. *Journal of the Mechanics and Physics of Solids*, 32:443–460, 1984.
- [44] Zehnder A. T., Rosakis A. J. Dynamic fracture initiation and propagation in 4340 steel under impact loading. *International Journal of Fracture*, 43(4):271–285, 1990.
- [45] Kobayashi A. S., Mall S. Dynamic fracture toughness of homalite 100. *Experimental Mechanics*, 18:11–18, 1978.
- [46] Liu C., Rosakis A. J. Investigation of transient effects for dynamically initiating and growing cracks under stress wave loading conditions. In *Dynamic fracture mechanics*. Computational Mechanics Publications, Southampton U.K., 1995.
- [47] Aoki S., Kishimoto K., Kondo H., Sakata M. Elastodynamic analysis of crack by finite element method using singular elements. *International Journal of Fracture*, 14:59–68, 1978.

- [48] Atluri S.N., Nishioka T. Numerical studies in dynamic fracture mechanics. *International Journal of Fracture*, 27:245-261, 1985.
- [49] Manolis G. D., Beskos D. E. *Boundary element methods in elastodynamics*. Unwin Hyman, London, 1988.
- [50] Domínguez J. *Boundary Elements in Dynamics*. Computational Mechanics Publications and Elsevier Applied Science, Southampton Boston and London New York, 1993.
- [51] Love A.E.H. *A treatise on the mathematical theory of elasticity*, 4th edn. Dover, New York, 1944.
- [52] Graffi D. Sul teorema di reciprocità nella dinamica dei corpi elastici. *Mem. Acad. Sci. Bologna*, 4:103-111, 1946/1947.
- [53] Wheeler L.T., Sternberg E. Some theorems in classical elastodynamics. *Arch. Rational Mech. Anal.*, 31:51-90, 1968.
- [54] Kellogg O.D. *Foundations of potential theory*. Dover, New York, 1929.
- [55] Love A.E.H. The propagation of wave motion in an isotropic elastic solid medium. *Proc. London Math. Soc.*, 2nd series, 1:291-344, 1904.
- [56] Mantic V. A new formula for the C-matrix in the Somigliana identity. *Journal of Elasticity*, 33:191-201, 1993.
- [57] Cruse T.A. Numerical solutions in three dimensional elastostatics. *International Journal of Solids and Structures*, 5:1259-1274, 1969.
- [58] Ahmad S., Banerjee P. K. Time-domain transient elastodynamic analysis of 3-D solids by BEM. *International Journal for Numerical Methods in Engineering*, 26:1709-1728, 1988.
- [59] Karabalis D.L. Efficient time and space integrations of stoke's fundamental solutions-applications to a direct time domain BEM for elastodynamics. In *Boundary Element Methods in Engineering*, ed. ,B.S. Annigeri and K. Tseng ; *Proceedings of the the International Symposium on Boundary Element Methods: Advances in Solid and Fluid Mechanics, East Hartford, Connecticut, USA, Oct 2-4, 1989* , Springer-Verlag, 1990.
- [60] Domínguez J., Gallego R. Time domain boundary element method for dynamic stress intensity factor computations. *International Journal for Numerical Methods in Engineering*, 33:635-647, 1992.
- [61] Cole D.M., Kosloff D.D., Minster J.B. A numerical boundary integral equation method for elastodynamics - I. *Bull. Seismol. Soc. Am.*, 68:1331-1357, 1978.
- [62] Rego Silva J. J., Wrobel L. C., Telles J. C. A new family of continuous/discontinuous three dimensional boundary elements with application to acoustic wave propagation. *International Journal for Numerical Methods in Engineering*, 36:1661-1679, 1993.
- [63] Brebbia C.A., Telles J.C.F., Wrobel L.C. *Boundary element techniques*. Springer-Verlag, Berlin, 1984.

- [64] Gallego R., Domínguez J. Hypersingular BEM for transient elastodynamics. *International Journal for Numerical Methods in Engineering*, 39:1681–1705, 1996.
- [65] Stroud, Secrest. *Gaussian quadrature formulas*. Englewood Cliffs: Prentice-Hall, 1966.
- [66] Doblaré M., Gracia L. On non-linear transformations for the integration of weakly singular and Cauchy principal value integrals. *International Journal for Numerical Methods in Engineering*, 40:3325–3358, 1997.
- [67] Guiggiani M., Krishnasamy G., Rudolphi T.J., Rizzo F.J. A general algorithm for the numerical solution of hypersingular boundary integral equations. *ASME Journal of Applied Mechanics*, 59:604–614, 1992.
- [68] Aliabadi M.H., Hall W.S., Phemister T.G. Taylor expansions for singular kernels in the boundary element method. *International Journal for Numerical Methods in Engineering*, 21:2221–2236, 1985.
- [69] Mi Y. *Three-Dimensional Analysis of Crack Growth*. Computational Mechanics Publications, Southampton UK and Boston USA, 1996.
- [70] Hayami K., Matsumoto H. A numerical quadrature for nearly singular boundary element integrals. *Engineering Analysis with Boundary Elements*, 13:143–154, 1994.
- [71] Cruse T.A. Mathematical foundations of the boundary integral equation method in solid mechanics. Technical Report AFSOR-TR-77-1002, Pratt and Whitney Aircraft Report, 1977.
- [72] Perucchio R., Ingraffea A.R. An integrated boundary element analysis system with interactive computer graphics for three-dimensional linear-elastic fracture mechanics. *Computers and Structures*, 20(1-3):157–171, 1985.
- [73] Martínez J.Q., Domínguez J. On the use of quarter-point boundary elements for stress intensity factor computations. *International Journal for Numerical Methods in Engineering*, 20:1941–1950, 1984.
- [74] Amestoy M., Bui H.D., Labbens R. On the definition of local path independent integrals in three-dimensional crack problems. *Mechanics Research Communications*, 8(4):231–236, 1981.
- [75] Carpenter W.C., Read D.T., Dodds R.H.Jr. Comparison of several path independent integrals including plasticity effects. *International Journal of Fracture*, 31:303–323, 1986.
- [76] Dodds R.H.Jr., Carpenter W.C., Sorensen W.A. Numerical evaluation of a 3-D J-integral and comparison with experimental results for a 3-point bend specimen. *Engineering Fracture Mechanics*, 29(3):275–285, 1988.
- [77] Dodds R.H.Jr. Finite element evaluation of J parameters in 3D. *International Journal of Fracture*, 33:R7–R15, 1987.
- [78] Rigby R.H., Aliabadi M.H. Mixed-mode J-integral for analysis of 3D fracture problems using BEM. *Engineering Analysis with Boundary Elements*, 11:239–256, 1993.

- [79] Hayami K. A robust numerical integration method for three dimensional boundary element analysis. In *Boundary Elements XII, Vol 1*, ed. M. Tanaka, C.A. Brebbia and T. Honma, Computational Mechanics Publication, Southampton, Springer-Verlag, Berlin, pages 33–51, 1990.
- [80] Shih C.F., Moran B., Nakamura T. Energy release rate along a three-dimensional crack front in a thermally stressed body. *International Journal of Fracture*, 30:79–102, 1986.
- [81] Luchi M.L., Rizzuti S. Boundary elements for three-dimensional elastic crack analysis. *International Journal for Numerical Methods in Engineering*, 24:2253–2271, 1987.
- [82] Benthem J.P. The quarter-infinite crack in a half space: Alternative and additional solutions. *International Journal of Solids and Structures*, 16:119–130, 1980.
- [83] Nishimura N., Guo Q. C., Kobayashi S. Elastodynamic crack analysis by BIEM. In *Boundary Elements in Applied Mechanics*, Tanaka M. and Cruse T. A. (eds), Pergamon Press, Oxford, pages 245–254, 1988.
- [84] Zhang C., Gross D. Non-hypersingular time-domain biem for 3D transient elastodynamic crack analysis. *International Journal for Numerical Methods in Engineering*, 36:2997–3017, 1993.
- [85] Zhang Y. Y., Shi W. Transient analysis of three-dimensional crack problems by the Laplace transform boundary element method. *Engineering Fracture Mechanics*, 47:715–722, 1994.
- [86] Wen P. H., Aliabadi M. H., P. Rooke D. Fictitious stress and displacement discontinuity method for dynamic crack problems. In *Boundary Elements XVI*, Brebbia C. A. (ed), Comput Mech Publ, Southampton, pages 469–476, 1994.
- [87] Wen P. H., Aliabadi M. H., P. Rooke D. Indirect boundary element method for three-dimensional dynamic problems. *Engineering Analysis with Boundary Elements*, 16:351–362, 1995.
- [88] Chirino F., Domínguez J. Dynamic analysis of cracks using boundary element method. *Engineering Fracture Mechanics*, 34:1051–1061, 1989.
- [89] Chirino F., Gallego R., Sáez A., Domínguez J. A comparative study of three boundary element approaches to transient dynamic crack problems. *Engineering Analysis with Boundary Elements*, 13(1):11–19, 1994.
- [90] Agrawal A. K., Kishore N. N. A study of free surface effects on through cracks using BEM. *Engineering Fracture Mechanics*, 2001 (accepted).
- [91] Nishioka T. Recent developments in computational dynamic fracture mechanics. In *Dynamic fracture mechanics*. Computational Mechanics Publications, Southampton, UK and Boston, USA, 1995.
- [92] Chen Y. M. Numerical computation of dynamic stress intensity factors by a Lagrangian finite-difference method (the hemp code). *Engineering Fracture Mechanics*, 7:653–660, 1975.

- [93] Lin X., Ballman J. Re-consideration of Chen's problem by finite difference method. *Engineering Fracture Mechanics*, 44(5):735–739, 1993.
- [94] Tsai C. H., Ma C. C. Theoretical and transient analysis of the interaction between a dynamically propagating in-plane crack and traction-free boundaries. *ASME Journal of Applied Mechanics*, 64:819–827, 1997.
- [95] Goodier J. N., Bishop R. E. D. A note on critical reflections of elastic waves at free surfaces. *Journal of Applied Physics*, 23(1):124–126, 1952.
- [96] Roesler F. C. Glancing angle reflection of elastic waves from a free boundary. *Phil. Mag. Ser. 7*, 46:517–526, 1954.
- [97] Beinert J. M. Schlierenoptical stress analysis of short duration pulses in elastic plates. *ASME Journal of Applied Mechanics*, pages 5–8, 1975.
- [98] Agrawal A.K., Kishore N.N. A study of free surface effects on through cracks under impact loading. *Engineering Analysis with Boundary Elements*, 2001 (accepted).
- [99] Das S. A numerical method for determination of source time functions for general three-dimensional rupture propagation. *Geophys. J. Roy. Astr. Soc.*, 62:591–604, 1980.
- [100] Das S., Kostrov B. V. On the numerical boundary integral equation method for three-dimensional dynamic shear crack problems. *ASME Journal of Applied Mechanics*, 54:99–104, 1987.
- [101] Koller M.G., Bonnet M., Madariaga R. Modelling of dynamical crack propagation using time-domain boundary integrals. *Wave Motion*, 16:339–366, 1992.
- [102] Fedelinski P., Aliabadi M.H. The time-domain BEM for rapidly growing cracks. *International Journal for Numerical Methods in Engineering*, 40:1555–1572, 1997.
- [103] Peirce A., Siebrits E. Stability analysis and design of time-stepping schemes for general elastodynamic boundary element models. *International Journal for Numerical Methods in Engineering*, 40:319–342, 1997.
- [104] Hildenbrand J., Kuhn G. Non-linear coordinate transformation of finite part integrals in two-dimensional boundary element analysis. *International Journal for Numerical Methods in Engineering*, 36:2939–2954, 1993.